Towards reconciling geodynamic models with kinematic reconstructions of slab sinking and plate motion

Erik van der Wiel

Members of the dissertation committee:

Prof. dr. N. Coltice
Côte d'Azur University - Nice, France

Prof. dr. J. H. Davies
Cardiff University - Cardiff, United Kingdom

Prof. dr. A. F. Deuss
Utrecht University - Utrecht, The Netherlands

Prof. dr. C. Faccenna
Roma Tre University - Rome, Italy

Dr. D. G. van der Meer
Utrecht University - Utrecht, The Netherlands

Towards reconciling geodynamic models with kinematic reconstructions of slab sinking and plate motion

Een opstap naar het overeenstemmen van geodynamische modellen met kinematische reconstructies van het zinken van platen en plaatbeweging

(met een samenvatting in het Nederlands)

Proefschrift

ter verkrijging van de graad van doctor aan de Universiteit Utrecht op gezag van de rector magnificus, Prof. Dr. H.R.B.M. Kummeling, ingevolge het besluit van het college voor promoties in het openbaar te verdedigen op

woensdag 8 mei 2024 des middags te 14.15 uur

door

Erik van der Wiel

geboren op 7 januari 1993 te Dordrecht

Promotoren:
Prof. dr. D. J. J. van Hinsbergen
Prof. dr. W. Spakman

Copromotor:
Dr. C. A. P. Thieulot

Beoordelingscommissie:
Prof. dr. N. Coltice
Prof. dr. J. H. Davies
Prof. dr. A. F. Deuss
Prof. dr. C. Faccenna
Dr. D. G. van der Meer

Contents

Summary

Deformation in the Earth's crust and the occurrence of earthquakes, volcanism and georesources are caused by processes occurring in the Earth's interior. Geodynamical models are the only way to study the interplay between the Earth's (deep) interior and its surface as many of these processes occur on timescales from millions to billions of years. Moreover, direct observations can only be done on the Earth's surface, where the geological record provides the only window back in time on these timescales. Geodynamic models often use input from one field and aim to predict structure, evolution of the solid Earth and explain processes therein, which may then be tested by observations from another field. Therefore, novel geological or geophysical observations provide a constant means to improve these models and thereby our understanding of the dynamic solid Earth. This dissertation focusses on the interaction between the Earth's mantle and the tectonic plate motion on top by using novel kinematic observations obtained through plate-tectonic reconstructions based on geological data.

One of these observations is the inferred average slab sinking rates, which are obtained by the correlation of the geological record with tomographically imaged slabs in the mantle. These illustrate the deceleration of slabs from plate motion speeds in the upper mantle to an average sinking rate in the lower mantle. We explore the effect of varying slab sinking rates on the long-term average magnitude of mantle flow and the propensity of mantle mixing in whole mantle convection models. Models with slab sinking rates of 10-15 mm/a have a very limited bulk mantle motion, of only a few mm/a. In these models the preservation of large unmixed zones in the mid-mantle occurs even after 1000 Ma of simulated subduction evolution and mantle convection. Comparing such models with the Earth's mantle is difficult as observations from the mantle come from the interpretation of seismic tomography or the chemical signature of plume-related volcanics. We use configurational entropy as a means to quantify and map the mixing of different compositions in our mantle convection models. This entropy may be used to analyse, with a single global measure, the mixed state of the mantle and compare various geodynamic models with each other. Furthermore, the local entropy may be useful to validate geodynamic models against local anomalies in the mantle from seismological or geochemical observations.

The deceleration of slabs from subducting plate velocities to the lower mantle average slab sinking rates occurs in the upper mantle and mantle transition zone by thickening or buckling of the subducting plate. Recent

high-resolution kinematic reconstructions of the Indian Plate revealed rapid oscillations in plate motion of up to 50% in 2-3 Ma which must be accommodated in the upper mantle. Our regional geodynamic models show that buckling of slabs can cause such oscillations in plate motion speed before eventual transfer of slabs in the lower mantle. We show that amplitude and period of such oscillations depend on the average subducting speed as it is subject to the time in which a subducted plate transfers through the upper mantle. We discuss how episodic deformation in the overriding plate may be caused by the buckling of subducting plates and how plate-tectonic reconstructions may generally smooth out such rapid plate motion oscillations.

This shows that tectonic plates are generally driven by subduction, or a 'slab pull' force, in the top few hundred kilometres of the mantle. However, plates without an attached slab, and therefore lacking such a force, are not mantle-stationary. For continental plates this may be explained by mantle drag on their keels induced by mantle flow and plume pulses. Contrarily, the Pacific Plate is an example of an oceanic plate that moved up to 9 cm/a in the Late Cretaceous without actively subducting and being surrounded by mid-oceanic ridges and transform faults. We use 3D-geodynamic models of an oceanic plate, surrounded by mid-oceanic ridges, that is influenced by the plate motion of the plates on either side of those ridges. These models show that the centre oceanic plate slowly trails the faster moving neighbouring plate and whose plate motion is increased by viscous coupling below the mid-oceanic ridges. We discuss the kind of mechanisms that may be responsible to induce such viscous coupling below a fast-spreading oceanic-ridge and how this may play a role in the transfer of changes in plate tectonic motion, for instance during global plate reorganizations.

This dissertation shows that geodynamic models, when tuned to specific kinematic observations of plate motion, are useful to study the processes driving tectonic plates and motion in the Earth's mantle. Such models provide a powerful means to gain inside in individual processes but also the linked dynamical evolution that shaped the Earth thereby using and improving insights from the various disciplines that study the solid Earth.

Introduction

Rationale and aims

A major target of the study of mantle dynamics is to explain how seemingly unrelated observations near the Earth's surface, such as distributed crustal deformation and earthquakes, volcanism, and location of georesources, and the formation and destruction of topography, may be connected through common drivers of deformation within the Earth's mantle. In the last decades, the study of these dynamics has improved dramatically through the use of numerical thermo-mechanical models focusing on how such first-order solid Earth processes operate. These models often use observations from one field as input and aim to predict the observations for another in a series of testable hypotheses (e.g., Coltice and Shephard, 2018). These so-called geodynamic models may then ultimately be used to predict structure, evolution, and processes in the solid Earth. Conversely novel, unexplained geological or geophysical observations challenging the state-of-the-art provide a means to continuously improve our models and related dynamic understanding.

There are currently two main concepts that explain the drivers of mantle dynamics. The first concept was developed a century ago, when Holmes suggested that the heating of the Earth's deep mantle and the cooling at the top, combined with its viscous nature, should generate convection Holmes, 1928 (Holmes, 1928), and could explain, through 'lateral flowage' the then-novel theory of Continental Drift proposed by Wegener (1912). Alternative drivers for surface motion and deformation were recognized in the 1960's as the newly formulated theory of plate tectonics (Isacks *et al.*, 1968; Le Pichon, 1968; McKenzie and Parker, 1967; Morgan, 1968). Plate tectonic forces such as slab pull, driven by the negative buoyancy of aging oceanic lithosphere, and to a lesser extent ridge push, driven by the gravitational gradient from ridge to trench, were recognized by Forsyth and Uyeda (1975) and lateral density contrasts, defining lateral buoyancy gradients, within the lithosphere by Fleitout and Froidevaux (1982). Although slab pull and ridge push are now widely recognized as the most important drivers of plate tectonics, whole mantle convection causing mantle drag at the base of plates may also be at work, although assessing its importance, either as a driving or a resisting force (Coltice *et al.*, 2019; Faccenna *et al.*, 2021), is challenging. An example of plate driving basal drag has been postulated to cause short-lived pulses of changes in plate motion caused by the arrival of mantle plumes below plates, which could generate plate boundary reorganizations

(van Hinsbergen *et al.*, 2021). Longer-term whole mantle convection causing basal drag and modifying the force balance between slap pull and ridge push have been invoked to explain, for example, the ongoing underthrusting of the Indian Continent below Asia (e.g., Becker and Faccenna, 2011; Faccenna *et al.*, 2013), although predictions from this process have not been reconciled yet with kinematic observations from neighbouring plates such as the Australia Plate (Becker and Faccenna, 2011).

This thesis aims to further our understanding of the interaction between mantle dynamics and the lithosphere by attuning geodynamic models, to explain different sets of plate-kinematic reconstructed observations, i.e., sinking rates of slabs across the mantle, and so far unexplained plate motions. These kinematic data have so far not widely been used as constraint in geodynamic modelling but have the potential to challenge the state-of-the-art. First, systematic correlations between slabs, imaged by mantle tomography, and geological records of subduction have provided kinematic estimates of the average rate at which detached slabs sink through the Earth's mantle, towards the core-mantle boundary (van der Meer *et al.*, 2012; van der Meer *et al.*, 2018). These slab sinking rates are individually substantiated from a correlation of tomographically imaged slabs in the mantle with the timing of subduction initiation and cessation based on geological interpretations (van der Meer *et al.*, 2018). These sinking rates suggest that slabs strongly decelerate from upper mantle sinking rates that are equal to subduction rates, i.e., up to 20 cm/a (Zahirovic *et al.*, 2015) to deep lower mantle sinking rates that decrease to 1-1.5 cm/a. This constitutes important constraints on the dynamics of the lower mantle and were previously used to explore implications for lower mantle viscosity (Čížková *et al.*, 2012). It is worth noting that in most cases, modern mantle convection models produce much higher rates of slab sinking (e.g., Peng and Liu, 2022; Li *et al.*, 2023) than inferred (Domeier *et al.*, 2016; van der Meer *et al.*, 2018). The inferred sinking rates allow exploring the flow behaviour of the ambient lower mantle, the degree to which whole-mantle convection may cause a driving mantle drag on plates, and how much of Earth's plate motion driving force must be generated in the less viscous upper mantle. Moreover, it provides possibilities to evaluate how efficiently the mantle may mix on long geological timescales, which could provide a mantle dynamic perspective to bridge observations obtained from seismology and geochemistry.

Finally, if slab pull and ridge push are the main drivers of plate motion, non-subducting tectonic plates, i.e. surrounded by ridges and transforms but not attached to a slab, are not expected to develop a large absolute plate motion. Particularly in the presence of large continental keels, the drag of

ambient convection of the mantle may to some extent drive plates (Coltice *et al.*, 2019; van Hinsbergen *et al.*, 2021), but so far, convection-driven absolute plate motions in excess of 4 cm/a have not been recognized (Becker and Faccenna, 2011). However, kinematic reconstructions by Torsvik *et al.* (2019) placed in a mantle reference frame have revealed that plates without continents nor associated keel, solely bounded by mid-oceanic ridges and transform faults, also develop a rapid absolute plate motion. Such plates range from small, such as the Bauer, Easter, and Galapagos microplates at the East Pacific Rise, to large such as the Pacific Plate. Additionally, Pacific and global hotspot frames reveal that the Pacific Plate has always had an absolute plate motion varying between 4 and 9 cm/a, which remains unexplained, and mostly unexplored in the current geodynamic literature. In this thesis, we aim to explore in which way plate-driving forces may propagate across the mantle wedge of active mid-oceanic ridges to propel plates without an active subduction zone: is major mantle drag required, or may intraplate lithospheric stress transmitted by remote slab pull also affect plates that are separated from the subducting plate by a ridge? We will then discuss how such coupling at ridges may influence estimates of plate dynamics and provide means to accommodate global plate reorganizations.

Methods

In this thesis we use the state-of-the-art numerical codes ASPECT (Kronbichler *et al.*, 2012; Heister *et al.*, 2017) and SEPRAN (van den Berg *et al.*, 1993; van den Berg *et al.*, 2015) to model the thermodynamically coupled problems of mantle and lithosphere dynamics. Both codes rely on the finite element method to solve the conservation of mass, momentum, and energy equations and are capable to accurately model the nonlinear geodynamic processes, among which the use of a visco-plastic rheology (Glerum *et al.*, 2018). Applications of these codes are versatile including for example: plate tectonic behaviour (Glerum *et al.*, 2020), subduction related processes (Pokorný *et al.*, 2021; Behr *et al.*, 2022; Pons *et al.*, 2022) and whole mantle convection (Čížková *et al.*, 2012; van den Berg *et al.*, 2019; Saxena *et al.*, 2023). Both codes can be run in parallel, and ASPECT uses adaptive mesh refinement (Burstedde *et al.*, 2011) which enables computationally fast parametric studies of solid Earth processes. In either code the Geodynamic World Builder may be used to create initial conditions for specific set-ups in Cartesian and spherical geometries (Fraters *et al.*, 2019).

Specific python and gnuplot based post-processors were developed to analyse and visualize the outcome of the numerical models. These post-processors use the generated data from passive particles in the numerical

models (Gassmöller *et al.*, 2018) which track the (initial) position and composition through time. The postprocessors use data-analysis and statistical approaches to calculate average sinking rates, the mixing-state of the mantle and the periodicity of plate motions. The particles also provide a unique way of visualizing flow in such geodynamic models by imposing a composition- or location-based indicator.

We use both two- and three-dimensional models with problem-specific set-ups in order to simulate the processes that take place in the solid Earth. Our modelling approach for the three different sets of kinematic data is similar. First, we create a reference model tailored to the specific problems of slab sinking rates, changing plate motions or the motion of non-subducting plates. Secondly, we perform a parametric study in which we vary the visco-plastic flow law parameters to match the proposed kinematic datasets. Thirdly, we use our postprocessors to evaluate and analyse the modelling results and create compelling visualizations.

Outline of this thesis

Chapter 1: Linking rates of slab sinking to long-term lower mantle flow and mixing

Chapter 1 uses the novel inferred average slab sinking rates of 10-15 mm/a (van der Meer *et al.*, 2018) to help constrain geodynamic modelling of global mantle convection. These slab sinking rates provide a kinematic constraint that is independent of interpretation or assumption on mantle convection as they are devoid of dynamic interpretations. This chapter presents 2D whole mantle convection models developed using the geodynamics code ASPECT (Kronbichler *et al.*, 2012; Heister *et al.*, 2017), in which we tuned rheological parameters within experimentally permitted ranges to develop self-consistent plate-like behaviour (e.g., Ulvrova *et al.*, 2019) and to vary lower mantle slab sinking rates. The chapter investigates under what set of rheological conditions, lower mantle slab sinking behaviour provides a first-order match with the plate-kinematically reconstructed average sinking rates. We then illustrate the effect which tuning of mantle flow models to slab sinking rates has on the overall convective flow of the mantle as well as on the degree of convective mixing in the modelled mantle after one billion years of convection. To this end, we compare models that match kinematically reconstructed average sinking rates with those with marginally matching rates, and with those with much higher sinking rates. We explore the implications of our results for long-term lower mantle geochemical reservoir stability.

Chapter 2: Quantifying mantle mixing through configurational entropy

Chapter 2 provides a means to objectively quantify the degree of mantle mixing in geodynamic models as maps of mantle heterogeneity. The geochemistry of oceanic islands basalts reveals the presence of heterogeneity in the Earth's mantle both on small and global scale, including remains of 'primordial' mantle that is thought to have remained essentially unmixed since the first formation of the mantle (e.g., Stracke *et al.*, 2019; Jackson *et al.*, 2021). Seismological observations of that same mantle reveal regional zones of material with coherent seismic properties, which may represent geochemical reservoirs. Geodynamic models have the power to provide both geochemical composition and the distribution of anomalies, and may be used to identify their seismic properties, but this requires bridging scales and translating model results to the fields geochemistry and seismology. Chapter 2 uses the model results from Chapter 1 and quantifies mixing at different scales using configurational entropy (Shannon, 1948). To this end, the chapter tracks compositions in geodynamic models to quantify the degree of mixing on a global and a local scale. It also discusses various ways to define 'compositions', i.e. both unchanging from an initial configuration (static) and changing compositions through time (dynamic), and proposes to use this method to relate seismological, geochemical observations with a modelled mantle.

Chapter 3: Slab buckling as a driver for rapid oscillations in plate motion and subduction rate

Mantle convection, induced by buoyancy of thermal anomalies in the mantle, seems to act on long temporal and spatial scales. Then it is surprising that novel high-resolution plate tectonic reconstructions reveal fluctuations in plate motion on very short (<3 Ma) time-scales (DeMets and Merkouriev, 2021). Previous modelling results (Briaud *et al.*, 2020; Pokornỳ *et al.*, 2021; Pons *et al.*, 2022) as well as tomographic observations Wu *et al.*, 2016; Chen *et al.*, 2019) have shown that slab buckling is the typical mechanism to decelerate subducting plates to lower mantle sinking rates by an order of magnitude. Slab buckling is an oscillating process, and Chapter 3 therefore explores whether it might also explain the rapid fluctuations in plate motion observed for India during its fast motion towards Eurasia in the Paleocene. To this end, we use as a starting point the 2D numerical modelling study of (Pokornỳ *et al.*, 2021), which is developed with the SEPRAN code (van den Berg *et al.*, 1993; van den Berg *et al.*, 2015).

This chapter evaluates to what extent the amplitude and period of plate motion oscillations depend on the subduction zone evolution, governed by the oceanic plate age or the resistance on the subduction interface. The chapter then discusses how slab buckling and possible plate kinematic effects may impact the deformation and motion of an overriding plate and it discusses which tectonic settings are conducive to such rapid oscillations.

Chapter 4: Slab pull driving absolute motion of adjacent non-subducting plates through viscous coupling at mid-oceanic ridges

Finally, Chapter 4 focuses on the simple question: how can tectonic plates that are not subducting along their boundaries attain a (fast) absolute plate motion? In particular we focus on oceanic plates surrounded by only mid-oceanic ridges and transform faults. The Late Cretaceous Pacific Plate is a primary example as it has not had an active subduction zone for long periods of its existence (Torsvik *et al.*, 2019). However, plate tectonic reconstructions reveal that its absolute plate motion in these times was trailing the fastest-moving neighbouring plates, dominated by the Izanagi Plate that was subducting below eastern Eurasia. Chapter 4 performs numerical experiments using a 3D set-up of three initial plates separated by spreading ridges. We test whether viscous coupling at spreading ridges could allow for the propagation of plate driving forces and for the development of an absolute plate motion of the plate bounded solely by spreading centres. It then discusses this mechanism in the context of intraplate stress and global plate reorganizations.

1

Linking rates of slab sinking to long-term lower mantle flow and mixing

Erik van der Wiel
Douwe J.J. van Hinsbergen
Cedric Thieulot
Wim Spakman

Abstract

Numerical models of Earth's mantle dynamics that aim to comply with a variety of surface observations and/or modern mantle structure, still predict a widely varying vigour of mantle flow which governs the long-term evolution of mantle structure and mixing. A yet unexplored source of intrinsic information on mantle flow characteristics are the geologically reconstructed average slab sinking rates. Here we evaluate from numerical experiments how average slab sinking rates relate to the vigour of mantle convection and mixing. We use a simplified mantle convection model and show that long-term mantle flow velocity and mixing is strongly sensitive to slab sinking rates. Models tuned to match lower mantle average sinking rates of 10-15 mm/a, yield lower mantle convection rates of only several mm/a. Furthermore, they reveal large unmixed regions in the mid-mantle which preserve 25% of 'primordial' lower mantle material after 1000 Ma, which may explain geochemical observations from hotspot volcanoes.

1.1   Introduction

Earth's mantle is a solid-state convecting system which governs multiple dynamic processes from deep geochemical mixing to the plate tectonics and deformation of the cold boundary layer (e.g. Bercovici *et al.*, 2015). How mantle processes dynamically operate can only be assessed by numerical modelling of the chemical-physical system as observations of mantle dynamics are generally of an implicit kinematic nature. Numerical experiments can be of a generic nature, or can focus on the simulation of mantle convection models that comply with observations, e.g., reconstructed and active plate motions (Coltice *et al.*, 2013; Rolf *et al.*, 2018), geochemical composition and evolution of the Earth's interior revealed by volcanic rocks (Yan *et al.*, 2020), and/or seismological observations of modern mantle structure (Ballmer *et al.*, 2016; Ritsema and Lekić, 2020). This large variety of observational constraints has, however, not led to imposing a strong constraint on the style of mantle convection in terms of the typical flow velocity and spatial variation, or of fast/slow geochemical mixing.

An unexplored source of information on the vigour of mantle convection are the geologically reconstructed average slab sinking rates of van der Meer *et al.* (2018). These slab sinking rates were determined for the tomographically imaged tops and bottoms of slabs by dividing the imaged depth by the geological time since subduction initiation and cessation. Importantly, these rates combine geological dating of past subduction with modern man-

tle structure and are therefore independent of any dynamic interpretation or assumption of mantle composition, flow, or rheology (viscosity). The average sinking rates imply that slabs move through zones in the mantle with different convective behaviour, from an upper mantle that permits, or drives, plate velocities, to a lower mantle in which rates are up to an order of magnitude slower: $10-15$ mm/a.

In this paper, we exploit the inferred depth variation in average slab sinking rates to assess the typical magnitude of vertical and horizontal slab velocity and assess the mixing behaviour of Earth's mantle. We perform a set of numerical experiments of simplified plate tectonics in a 2D cylindrical geometry in which we vary lower mantle rheology to obtain lithosphere subduction and slab sinking with rates that vary from <10 to >50 mm/a. From these experiments we evaluate the first-order correlation between slab sinking rates and bulk mantle flow. We focus on the long-term (1000 Ma) evolution of bulk mantle flow in terms of typical mantle velocity and the degree of mantle mixing through the potential preservation of mantle heterogeneities.

1.2   Background

A key mantle property in convection models is the dynamic viscosity, which relates the mechanical stress to the solid-state mantle flow. Various types of observations have been used to obtain a depth-dependent profile of mantle viscosity (Mitrovica and Forte, 2004; Steinberger and Calderwood, 2006; Čížková *et al.*, 2012; King, 2016; Rolf *et al.*, 2018; Argus *et al.*, 2021) resulting in estimated radial viscosity profiles which can differ by more than an order of magnitude (Figure 1.1). Within the currently accepted ranges of mantle properties, numerical models predict semi-layered convection (Kellogg and Turcotte, 1990; Waszek *et al.*, 2021), whole mantle convection (Becker and Faccenna, 2011; Flament *et al.*, 2022), or a hybrid-variant with limited interaction between the upper and lower mantle (Gülcher *et al.*, 2020; Waszek *et al.*, 2021). In such models ambient mantle flow at the base of the mantle can have different magnitudes, indicated by near-stagnant (Bull *et al.*, 2010) or highly mobile (Flament *et al.*, 2022) Large Low Shear Velocity Provinces (LLSVPs). This variety in flow magnitudes allow for a well-mixed (Coltice and Schmalzl, 2006) or strongly heterogeneous mantle (Keken *et al.*, 2002; Barry *et al.*, 2017; Gülcher *et al.*, 2021). These variations in mantle convection pattern show that new constraints are desirable to further limit the range of possibilities towards developing more predictive models.

Chapter 1
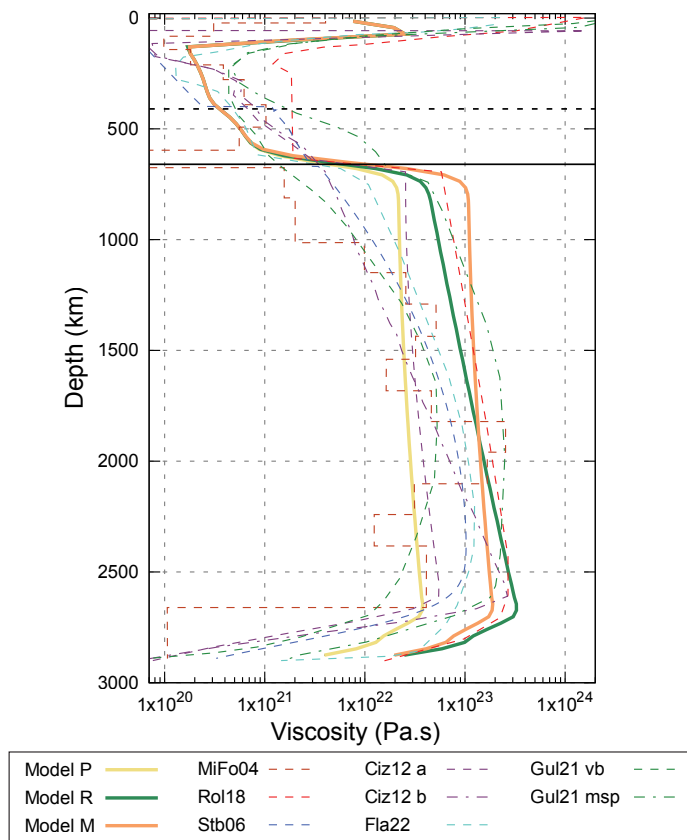
Figure 1.1 Radial viscosity profiles for the three models discussed here (solid lines: P - Poor, R - reference and M - Moderate) compared to viscosity profiles as used in other studies: MiFo04 (Mitrovica and Forte, 2004), Stb06 (Steinberger and Calderwood, 2006), Ciz12-a & -b family (Čížková *et al.*, 2012), rol18 case M8 (Rolf *et al.*, 2018), Gul21 viscous blobs (vb) & metastable piles (msp) (Gülcher *et al.*, 2021), Fla22 (Flament *et al.*, 2022).

In the last decade, average slab sinking rates have been inferred from the association of geological evidence of the timing of past subduction with large positive seismic velocity anomalies imaged in the modern mantle by seismic tomography (van der Meer *et al.*, 2010; van der Meer *et al.*, 2018). Pioneering studies showed that the geological records of subduction can be used to date the timing of subduction of imaged slab remnants (van der Voo *et al.*, 1999; Faccenna *et al.*, 2003; Replumaz *et al.*, 2004; van Hinsbergen *et al.*, 2005; Hafkenscheid *et al.*, 2006). Since then, positive seismic wave speed anomalies in tomography have been systematically interpreted and linked to detailed geological reconstructions, whereby shallower (deeper) anomalies are well explained by younger (older) subduction zones. From

Table 1.1 Global model parameters

Surface temperature	300 K
Bottom temperature	3700 K
Mantle thickness	2890 km
Thermal expansivity	3×10^{-5} K^{-1}
Thermal diffusivity	1×10^{-6} m^{2}s^{-1}
Thermal conductivity	6 Wm^{2}s^{-1}
Heat capacity	1250 Jkg^{-1}K^{-1}
Radiogenic heating rate	5.44×10^{-12} Wkg^{-1}
Reference density	3316 kgm^{-3}
Continental reference density	2916 kgm^{-3}
Minimum viscosity cut-off	1×10^{20} Pas
Maximum viscosity cut-off	6×10^{24} Pas
Compressibility	5.12×10^{-12} Pa^{-1}

these correlations, a globally consistent average slab sinking rate of $12 - 13 \pm 3$ mm/a has been calculated (Butterworth *et al.*, 2014; van der Meer *et al.*, 2010). More recently, the comprehensive, global compilation (van der Meer *et al.*, 2018) revealed how subducted lithosphere decelerates from plate motion speeds down to an average of $10 - 15$ mm/a in the lower mantle. This deceleration starts in the mantle transition zone and continues to 1000-1500 km depth and is consistent with evidence for buckling and thickening of slabs in the same interval (van Hinsbergen *et al.*, 2005; Sigloch and Mihalynuk, 2013; Fuston and Wu, 2021). These correlations suggest that after detachment slabs sink nearly vertically, which is also independently substantiated by statical analysis of positive seismic anomalies and locations of paleo-subduction (Domeier *et al.*, 2016). The inferred sinking rates are all confined to a much narrower sinking rate range than the < 10 to > 50 mm/a that we study in our experiments.

1.3   Methods

We performed numerical experiments in a 2D cylindrical geometry, simulating global mantle convection during 1000 Ma of subduction evolution. These models are used to obtain slabs varying in size and shape and track their lower mantle sinking rates to compare with the slab sinking rates from (van der Meer *et al.*, 2018). Our models are purposely simple to solely illustrate the effect of different slab sinking rates, obtained through different lower mantle viscosity profiles, on mantle convection patterns.

Table 1.2 Model parameters for viscous flow laws

Viscosity parameters (model R)	Upper mantle	Mantle transition zone	Lower mantle	Continents
Dislocation creep				
Prefactors (A) Pa^{-n}s^{-1}	6.51×10^{-16}	8.51×10^{-16}	6.51×10^{-16}	6.51×10^{-28}
Stress exponents (n)	3	3	1	1
Activation energies (E) Jmol^{-1}	500×10^3	500×10^3	530×10^3	540×10^3
Activation volumes (V) m^{3}mol^{-1}	1.3×10^{-5}	1.3×10^{-5}	1.3×10^{-5}	1.8×10^{-5}
Diffusion creep				
Prefactors (A) Pa^{-n}s^{-1}	6.00×10^{-17}	9.00×10^{-17}	1.00×10^{-18}	-
Activation energies (E) Jmol^{-1}	150×10^3	155×10^3	150×10^3	-
Activation volumes (V) m^{3}mol^{-1}	6.34×10^{-7}	14.34×10^{-7}	12.34×10^{-7}	-
Cohesions (C) MPa	4	-	-	10
Angles of internal friction (f)	1.434	-	-	30

Phase transitions	410 km	660 km
Reference temperatures K	1700	1900
Clapeyron slopes MPaK^{-1}	3	-2.5

Lower Mantle viscosity parameters for the S- and F-family models

S-family models	Pre-factor diffusion creep	Diffusion creep activation volume
F1 / S1 (Poor fit)	1.0×10^{-18}	8.34×10^{-7}
S2	6.0×10^{-19}	=
S3 (Moderate fit)	2.0×10^{-19}	=
S4	1.0×10^{-19}	=

F-family models	Pre-factor diffusion creep	Diffusion creep activation volume
F1 / S1 (Poor fit)	1.0×10^{-18}	8.34×10^{-7}
F2	=	10.34×10^{-7}
F3 (Good fit, reference)	=	12.34×10^{-7}
F4	=	14.34×10^{-7}

1.3.1 Physical model

In our experiments, we solve the compressible flow equations of mass (1.1), momentum (1.2), and energy conservation (1.3) in a 2D spherical shell. Computations were done using the finite element geodynamic code AS-PECT version 2.3.0 (Kronbichler *et al.*, 2012; Heister *et al.*, 2017; Gassmöller *et al.*, 2018; Bangerth *et al.*, 2021), in which we solve for the velocity (u), pressure (P) and temperature (T).

$$\frac{\partial \rho}{\partial t} + \nabla \cdot (\rho u) = 0 \tag{1.1}$$

$$\nabla \cdot \sigma + \rho g = 0 \tag{1.2}$$

$$\rho C_p \left(\frac{\partial T}{\partial t} + u \cdot \nabla T \right) - \nabla \cdot (k \nabla T) = \rho H + S_s + S_a + S_l \tag{1.3}$$

The second and third terms of the energy conservation equation (1.3) account for the advective and diffusive heat transport whereas the right-hand side contains additional heating processes, i.e. radioactive heat production (ρH), shear heating (S_s), adiabatic heating (S_a) and latent heating (S_l) which are coupled to strain rate, thermal expansivity and phase changes in the model, respectively (Schubert *et al.*, 2001; Zelst *et al.*, 2022).

We use the Isentropic Compression Approximation (ICA), the default approximation for compressible flow in ASPECT (Gassmöller *et al.*, 2020). The ICA neglects the time derivative of the density in the mass conservation equation but does compute a local adiabat based on temperature, pressure, and composition, which results in the alteration of the mass conservation to equation (1.4), where κ_s is the compressibility and ρ the density as function of pressure, temperature, and composition (Gassmöller *et al.*, 2020). Composition dependent material properties are advected through equation (1.5) using compositional fields (c_i).

$$\nabla \cdot u = -\kappa_s \rho g \cdot u \tag{1.4}$$

$$\frac{\partial c_i}{\partial t} + u \cdot \nabla c_i = 0 \tag{1.5}$$

1.3.2 Viscous flow formulation

Flow in our model is governed by the viscous-plastic flow equations that describe dislocation and diffusion creep and we use the Drucker-Prager yield criterion to limit viscous stresses (Glerum *et al.*, 2018). Equation (1.6) calculates the diffusion and dislocation creep viscosity which are a function

of the effective deviatoric strain rate ($\dot{\varepsilon}$), pressure (p), and temperature (T), as well as material properties defined in tables 1.1 and 1.2 (Glerum *et al.*, 2018; Karato and Wu, 1993). The grain-size in the diffusion creep is assumed constant and therefore incorporated in the pre-factor A. Diffusion creep is obtained by setting $n = 1$ in equation ($\dot{\varepsilon}$) and dislocation creep by $n = 3$. In the lower mantle flow is based on diffusion creep only.

$$\eta^{cr} = \frac{1}{2}A^{-\frac{1}{n}}\dot{\varepsilon}^{\frac{1-n}{n}}exp\left(\frac{E+pV}{nRT}\right) \qquad (1.6)$$

$$\sigma_y = C\cos\phi + P\sin\phi \qquad (1.7)$$

$$\eta^{pl} = \frac{\sigma_y}{2\dot{\varepsilon}} \qquad (1.8)$$

$$\eta^{cr}_{ave} = \left(\frac{1}{\eta_{diff}} + \frac{1}{\eta_{disl}}\right)^{-1} \qquad (1.9)$$

$$\eta^{eff} = min\left(\eta^{pl}, \eta^{cr}_{ave}\right) \qquad (1.10)$$

In 2D the Drücker-Prager yield criterion is similar to the Mohr-Coulomb criterion as shown in equation (1.7) (Glerum *et al.*, 2018). The criterion is parameterised by the cohesion C and angle of internal friction ϕ, where the latter has the same depth dependency as in Ulvrova *et al.* (2019). The effective viscosity is rescaled in equation (1.8) to ensure that local stresses cannot exceed the yield stress (Glerum *et al.*, 2018). As both the dislocation and diffusion creep could be active simultaneously, the two are harmonically averaged in equation (1.9) before the effective viscosity (η^{eff}) is calculated in equation (1.10), which is the lowest of either the plastic (η^{pl}) or averaged creep viscosity (η^{cr}_{ave}).

The flow law parameters in the upper mantle (UM) (Table 1.2) are constant in all experiments where the pressure and temperature dependence of diffusion creep is based on Ulvrova *et al.* (2019)). This enabled us to obtain self-consistent subduction evolution comprising initiation and cessation of subduction zones. However, in the mantle transition zone (MTZ) we use higher depth-dependency (activation volume) for dislocation creep. We obtain a viscosity in the UM between 10^{20} and 10^{21} Pa s (Figure 1.1). To evaluate the effect of different slab sinking rates we vary the lower mantle viscosity in two ways, creating two families of models. We either change the pre-factor (A) or the activation volume (V) in equation (1.6), respectively between $1-10 \times 10^{19}$ Pa^{-n} s^{-1} and $8.34-14.34 \times 10^{-7}$ m^3 mol^{-1} (Table 1.2). These values lead to lower mantle viscosities in our models between 2×10^{22} and 1×10^{24} Pa s (Figure 1.1; Supplementary figure 1).

1.3.3 Set-up

Both the inner and outer boundaries are free-slip boundaries, so there is no external kinematic forcing on the model. The resulting existing rotational null space is removed by imposing no-net-rotation of the mantle. The boundaries have fixed temperatures of 3700 K and 300 K. Within the domain two compositional fields are defined: mantle and continent. The mantle domain consists of three different regions separated by the two major phase changes occurring at 410- and 660-km depths. We use the geodynamic World Builder (Fraters *et al.*, 2019) to set the initial temperature and compositional field distribution. Similar to Ulvrova *et al.* (2019), we use viscous rafts as 'continents' to aid with modelling one-sided subduc-
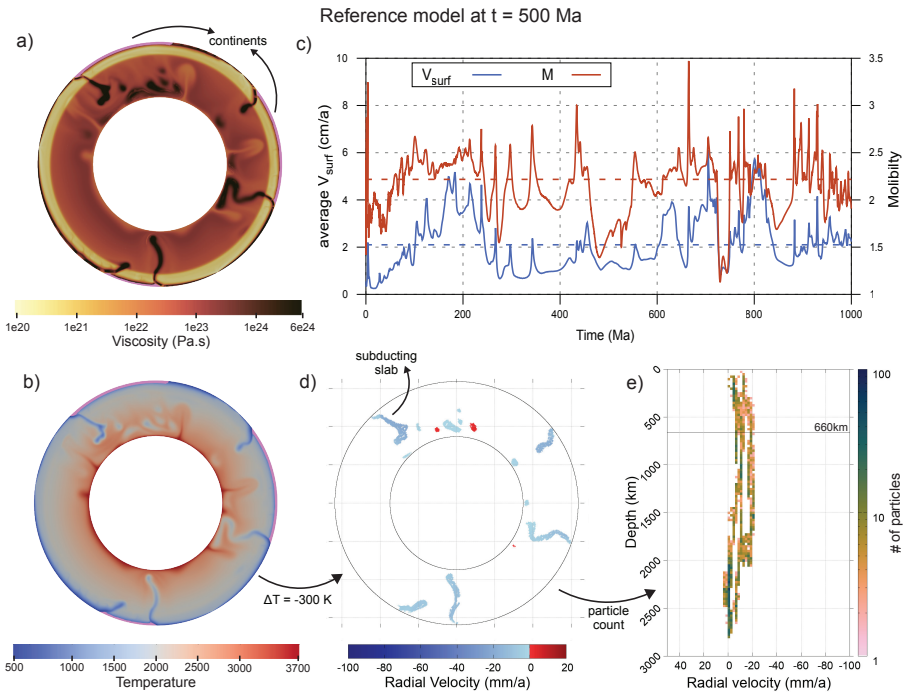

Figure 1.2 Results of the reference model (R) after 500 Ma of mantle convection simulation. Snapshots of the model at $t = 500$ Ma are shown for the viscosity (**a**) and temperature (**b**) within the modelled domain, showing five slabs actively subducting below the continents (pink). **c** Solid lines indicate average surface velocity (blue) and mobility ratio M (Tackley, 2000) (red) of model R as well as their dashed time-averages V_{surf}=2.1 cm/a and $M =$ 2.218. **d** Radial velocity of all tracers defined as slabs plotted at their position in the model where blue indicates sinking slabs and red slowly rising. Shown tracers are 300 K colder than the radial averaged temperature at similar depth and automatically obtained (see methods). **e** 2D-histogram showing the depth vs the radial velocity in 25 km by 2 mm/a bins of the tracers identified as slabs. The colour indicates the number of tracers within a certain bin.

tion systems (Ulvrova *et al.*, 2019). We use three continents of 5000, 5000 and 3000 km length, covering roughly 30% of the model surface. To avoid subduction of the continents, we assign the viscous rafts a reference density of 2916 $km\,m^{-3}$, which corresponds to a 400 $km\,m^{-3}$ density contrast with the reference mantle density (Lamb *et al.*, 2020). Furthermore, to avoid deformation of the continents, we assign them a viscosity that equals the maximum cut-off viscosity in the model, i.e. 6×10^{24} Pa s. We also configure three subduction zones and two detached slabs in the initial set-up to seed the model with initial negative buoyancy.

Material properties like thermal expansivity, thermal conductivity and compressibility are a constant (Table 1.1). We acknowledge this may not be the case for Earth, but exploring the effects of the depth, temperature and compositional dependencies of these parameters is beyond the scope of this study. Through the Rayleigh number we know that a decreasing thermal expansivity and increasing thermal conductivity with depth would lower the vigour of mantle convection, especially in the lowermost mantle (Tosi *et al.*, 2013; Guerrero *et al.*, 2023). However, this vigour should still comply with the inferred average slab sinking rates and therefore in our study this would lead to mantle viscosity profiles somewhat reduced in magnitude to establish the same goal of evaluating the accompanying convective behaviour.

The minimal resolution of the mesh in the top 370 km of the modelled domain is 26 km wide cells at the surface, while in the top 1370 km the minimal resolution is a cell width of about 40 km at 1370 km depth. Besides these criteria the mesh refinement is also adaptive, based on viscosity gradients and the velocity field, allowing for refinements up to 13 km wide at the surface. These higher resolutions in the top of the domain allow for accurate modelling of plate-like motion and the initiation of subduction.

1.3.4 Postprocessing

As we do not prescribe any kinematical boundary conditions in our experiments, we can use the surface velocity of plates to evaluate plate-like motion behaviour, assessed by computing the mobility ratio M (Figure 1.2c), which is the ratio of surface motion to motion in the entire domain (equation 1.11). When higher than 1, M is deemed indicative of plate-like behaviour (Tackley, 2000).

$$M = \frac{V_{rms,surface}}{V_{rms,domain}} \tag{1.11}$$

We change the rate of slab sinking in the lower mantle by tuning the global lower mantle viscosity (Figure 1.1) which we vary by increasing/decreasing the activation volume V, leading to a pressure dependent viscosity
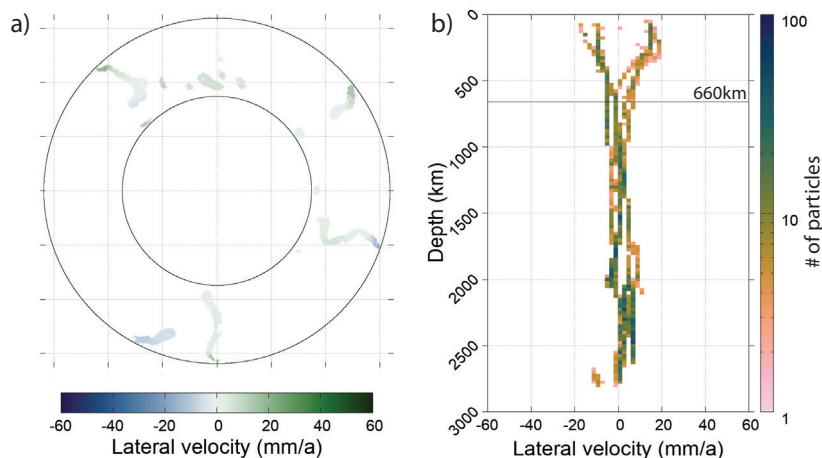
Figure 1.3 Lateral slab velocity distribution for the reference model (R) at $t = 500$ Ma. **a** Lateral velocity of all tracers defined as slabs plotted at their position in the model, where positive (green)values indicate clockwise motion, and negative (blue) values indicate anti-clockwise motion. **b** 2D-histogram showing tracer depth vs lateral slab motion in 25 km by 2 mm/a bins. Colours indicate the number of tracers within a certain bin.

increase/decrease with depth, and/or by changing the pre-factor of the diffusion creep law A, leading to an overall shift in the viscosity profiles to lower/higher values, see equation (1.6) and Table 1.2. Modelling 1000 Ma of ocean-ocean and ocean-continent convergence within the cold thermal boundary layer leads multiple subduction zones through time that result in slabs of varying size and shape sinking to the CMB in each experiment (Figure 1.2).

We track the slabs during their mantle journey with passive tracers. Slabs are automatically identified by tracers that move faster than 1 mm/a and have a local temperature that is 300 K lower than the average temperature at depth (Figures 1.2b,d and 1.3a). This temperature threshold is based on estimates of the tomographic visibility of slabs using conversions between seismic velocity anomalies and temperature (Trampert *et al.*, 2001; Goes *et al.*, 2004). 2D-histograms of slab velocity versus depth are constructed from the slab tracers in 5 Ma intervals (Supplementary Movies 1-3). This is done separately for the lateral (Figure 1.3b) and radial (Figure 1.2e) velocity components using a speed interval of 2 mm/a and a depth interval of 25 km. The resulting 200 histograms per experiment are summed to create the accumulated distribution of lateral and radial slab velocities during the 1000 Ma of simulated mantle convection (Figure 1.4). Our experiments show that these accumulated histograms gradually become time

stationary. This allows to compute the time-average of *in situ* slab sinking velocity $V(d)$ at mantle depth d from which the average slab sinking rate $V_{ave}(d)$ is obtained with equation (1.12).

$$V_{ave}(d) = \frac{1}{d} \int_0^d V(z)dz \qquad (1.12)$$

$V_{ave}(d)$ represents the model prediction of the average sinking rate for slabs between the surface and the depth d and can directly be compared to the kinematically inferred average slab sinking rates (van der Meer *et al.*, 2018).

1.4 Results

1.4.1 Natural subduction and plate-tectonic behaviour

The surface plate velocities in our experiments are self-generated and are within typical reconstructed ranges of less than 20 cm/a (Zahirovic *et al.*, 2015), and generally below the 10 cm/a. The differences in average plate motion between experiments are small and addressed in the sections below. In all our experiments we obtain lateral plate motions that lead to converging and separation of the cold thermal boundary layer, indicating subduction zones and mid-oceanic ridges. Subduction under the 'continents' is one-sided (Figures 1.2a,b) and occasionally, in regions with a thin (weak) oceanic lithosphere, intra-oceanic subduction can be two-sided. This occurs through polarity flips of the subduction interface. As our study focusses particularly on the sinking rates of slabs in the lower mantle, the occasional double-sided subduction of the cooled thermal boundary layer material is of no influence on our results. Lateral slab motions in the lower mantle are smaller than their vertical component, indicating that most slabs sink vertically after detachment.

The initially imposed continental regions (Figures 1.2a,b) can move away and towards each other, driven by active downwelling of cold material at subduction zones and accommodated by the formation of oceanic ridges. Occasionally this leads to continental collision and break-up of previously collided continents.

Our experiments show the straightforward trend that with increasing lower mantle viscosity the average slab sinking rates $V_{ave(d)}$ decrease. Therefore, we can limit the result description to three models obtained in distinct experiments. First, the reference model R ($A_{df} = 1 \times 10^{-18}$ Pa^{-1}s^{-1}, $V_{df} = 12.34 \times 10^{-7}$ m^3 mol^{-1}) in which the predicted average slab sinking rates compare well with those kinematically reconstructed (van der Meer

et al., 2018). Second, model M ($A_{df} = 2 \times 10^{-19}$ Pa^{-1}s^{-1},$V_{df} = 8.34 \times 10^{-7}$ m^3 mol^{-1}) that provides a marginal sinking rate fit and third, model P ($A_{df} = 1 \times 10^{-18}$ Pa^{-1}s^{-1},$V_{df} = 8.34 \times 10^{-7}$ m^3 mol^{-1}) that exemplifies models yielding a poor match to the sinking rate constraints, with much higher sinking rates than permitted by the data. We will use these three experiments to evaluate the effects of tuning mantle convection models to slab sinking kinematics.

1.4.2 Reference model R

The average plate velocity along the surface of the reference model R is between 1 and 6 cm/a with a time-averaged mobility ratio Mr of 2.218 (Figure 1.2c), which is in the realm of plate-like behaviour (Tackley, 2000). The averaged surface velocity is within the typical plate motion ranges reconstructed for the last 200 Ma (van der Meer *et al.*, 2014; Zahirovic *et al.*, 2015). The three continents that are initialised in the set-up resist subduction and move around laterally along the surface while colliding, diverging, and shielding parts of the subcontinental mantle from active subduction (Supplementary Movie 4).

Slab sinking rates in the uppermost mantle are similar to subducting plate motions, generally below 10 cm/a but occasionally reaching 20 cm/a, again similar to typically reconstructed values (van der Meer *et al.*, 2014; Zahirovic *et al.*, 2015). Deceleration of the model slabs starts in the mantle transition zone (MTZ) and continues throughout the lower mantle (Figure 1.4a). The averaged *in situ* sinking velocities $V(d)$ has a clear maximum in the upper mantle on top of the MTZ. The first part of the lower mantle shows *in situ* sinking velocities around 15 mm/a up to 1000 km depth before gradually slowing down to 0 mm/a at the CMB (Figures 1.4a, 1.5a). The slab sinking rate $V_{ave}(d)$ decreases from 15 mm/a at the top of the lower mantle to 10 mm/a at the CMB which fits the kinematically reconstructed average sinking rates of 10-15 mm/a (van der Meer *et al.*, 2018).

Lateral motion of slabs in the upper mantle is mostly restricted between -20 and 20 mm/a (negative (positive) numbers indicate clockwise (anticlockwise) motion in the model) clearly decreasing from the surface to the 660-discontinuity (Figure 1.4b). The average lateral velocity in the lower mantle is -2 mm/a with a standard deviation of 5-8 mm/a, dependent on depth, which comprises most (85%) of the slab-defining tracers (Figure 1.4b). This shows that most slabs sink nearly vertically in the reference model.
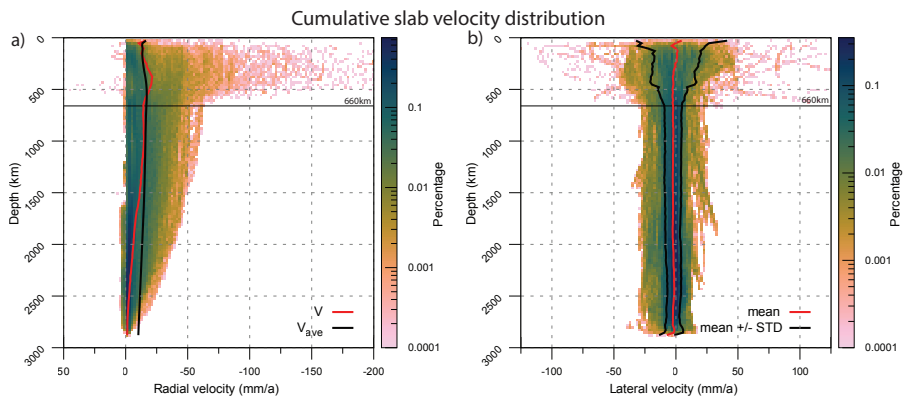
Chapter 1

Figure 1.4 Slab sinking rate distribution. Summation of all slab velocity distributions from the reference model (R) taken every 5 Ma (see figures 1.1e, 1.2b; supplementary movie 1). The colour scale represents the percentage of all slabs (tracers) that sunk in 1000 Ma of mantle evolution. Tracers defined as slabs can be counted in multiple time intervals. **a** Radial slab velocity distribution with averaged in situ radial slab velocities at each depth (red) and integrated slab sinking rate through equation 1.12 (black). **b** Lateral slab velocity distribution in which positive (negative) values indicate (anti-)clockwise motion, mean lateral slab velocity at each depth (red) and mean plus/minus a standard deviation (black).

1.4.3 Tuning slab sinking rates

Our experiments show that lower mantle viscosity has a small influence on surface plate motions but a first-order impact on slab sinking rates, as exemplified by the models with a poor (P) and moderate (M) fit to the slab sinking rates. Model P is based on a viscosity profile that is generally of smaller amplitude in the lower mantle than the profile of model R (Figure 1.1), while the profile of model M has higher viscosities in the top part of the lower mantle and lower values in the bottom part (Figure 1.1). Models P and M have similar averaged mobility factors ($M_p = 2.215$, $M_m = 2.332$, resp.) as model R ($M_r = 2.218$). The spherically averaged surface velocities in model P and M are larger than in model R, generally between 1 and 10 cm/a. A contrast between the model predictions occurs mainly in the attained slab sinking rates. Model P results in a poor match to the inferred slab sinking rates exemplified by the four times larger maximum *in situ* sinking velocity (Figure 1.6), because of the lower lower mantle viscosity in model P (Figure 1.1). Excess peak-velocities in model P occur in the upper mantle and around 1000 km depth, where *in situ* sinking velocities reach highest values up to 60 mm/a (Figure 1.5a; Supplementary Figure 2). The large difference in *in situ* velocities between models P and R translates into a large difference in average sinking rates. Model P has average sinking

rates between 40 and 60 mm/a (Figure 1.5b; Supplementary Figure 3), about four times higher than in model R.

Subduction in model M leads to average sinking rates in the lower mantle that are comparable to the faster side of inferred sinking rate values (Figure 1.5b). Model M has an average lower mantle viscosity that is only slightly increasing with depth, from 10^{23} Pa s in the top of the lower mantle to 2×10^{23} Pa s in the deep lower mantle (Supplementary Figure 1). The maximum *in situ* sinking velocity in model M is twice as large as in the reference model R, up to 35 mm/a in the upper mantle (Figure 1.5a; Supplementary Figure 2). The sinking velocities in the lower mantle are, again, highest around 1000 km depth where slabs in model M sink with a depth-averaged *in situ* velocity of 18 mm/a. The average slab sinking rates of model M are above 20 mm/a in the upper part of the lower mantle while decreasing to 14 mm/a near the CMB (Figure 1.5b).

The lateral motion of slabs in the lower mantle is directly correlated to the sinking rates, models with slabs that sink fastest also show a greater variability in lateral motion across the mantle. Broadly distributed lateral velocities over 100 mm/a occur in the entire lower mantle of model P (Supplementary Figure 2) and although the lateral average remains close to the centre at $2 - 3$ mm/a, the standard deviation is with $18 - 22$ mm/a, varying with depth, in the lower mantle three times larger than in the reference model R. Model M occasionally has lateral slab velocities over 20 mm/a in the lower mantle, however, the histograms shows a narrow distribution with standard deviations of maximum 10 mm/a (Supplementary Figure 2).

1.4.4   Mantle flow and mixing

In our models, cold slabs are the main drivers of mantle flow, and their sinking triggers hot upwellings from the lower thermal boundary layer. Over geological time this leads to mantle mixing, the efficiency of which depends on the vigour of mantle convection. We analyse the overall evolution of mantle motion, as well as mixing, by tracking predefined tracer clouds over time in three different ways. First, we track how 4 circular tracer clouds at 0 Ma are dispersed through time in steps of 250 Ma (Figures 1.6a,b). Second, we investigate the positions at 0 Ma, and at every 250 Ma, of tracers that aggregate in the same 4 circular regions after 1000 Ma of model evolution (Figures 1.6c,d). Third, to visualize mixing in the entire mantle, we track all initial 100.000 tracers, colour coded as function of their radius at 0 Ma. Figures 1.7a-d show all tracers at 500 Ma and 1000 Ma and Supplementary Movies 4-6 show the mantle flow and mixing through time in steps of 5 Ma. Furthermore, we track the number of tracers that have been entrained in
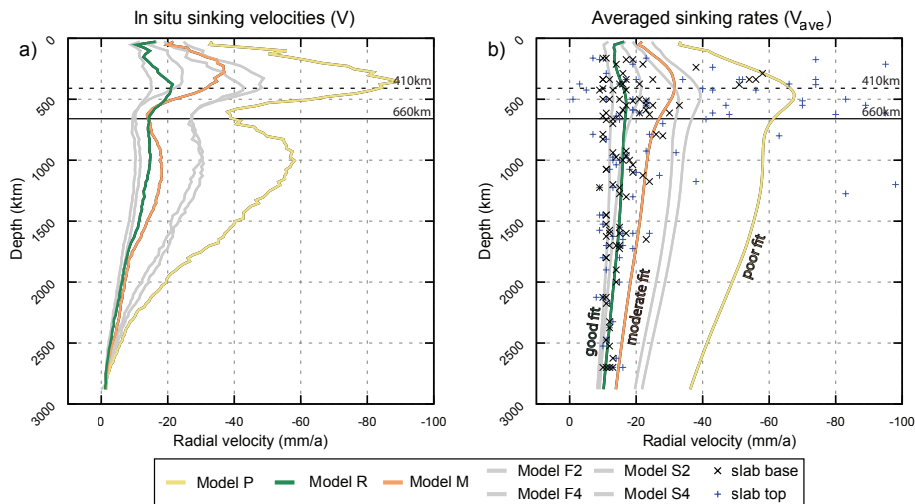
Figure 1.5 Profiles of in situ sinking velocities and averaged sinking rates from equation 1.12 matched with the data from (van der Meer *et al.*, 2018). **a** In situ sinking velocities calculated as depth average from the cumulative radial slab velocities (Figure 1.4a – red line). **b** Averaged slab sinking rates (Figure 1.4a – black line) integrated through equation 1.12 (methods) compared to the slab data (van der Meer *et al.*, 2018) base (plus) and slab top (cross) data. The models with a good fit (model R – green), moderate fit (model M – orange) and poor fit (model P – yellow) are shown in colour together with all other S and F models in grey. The cumulative slab velocity distributions for all models are shown in supplementary figures 2,3.

the upper mantle or in the lithosphere (configured as the top 100 km of the modelling domain) or stayed in the lower mantle in 1000 Ma of model evolution (Figure 1.8).

The dispersion of tracers in models R and M is similar: both models have large provinces of tracers that move in unison for the first 500 Ma of convection. These coherently moving mantle volumes deform while moving slowly through the lower mantle but can be dispersed and stretched when a slab sinks through (Figures 1.6a,b). Most lateral motion and dispersion of these tracers occurs after their entrainment in the upper mantle or lithosphere (Figure 1.6b). Accordingly, tracers that never enter the upper mantle undergo little dispersion in the mantle. In model R, some tracers only moved by 2000 km in 1000 Ma of convection (Figure 1.6a), which gives an average non-slab mantle velocity of 2 mm/a. Both model R and M have mantle provinces that remain in the mid-mantle and that show no or little mixing throughout the modelled 1000 Ma time period. An increased tracer cloud stretching and dispersing is observed in Model P, signalling stronger

Tracer dispersion

Tracer aggregation
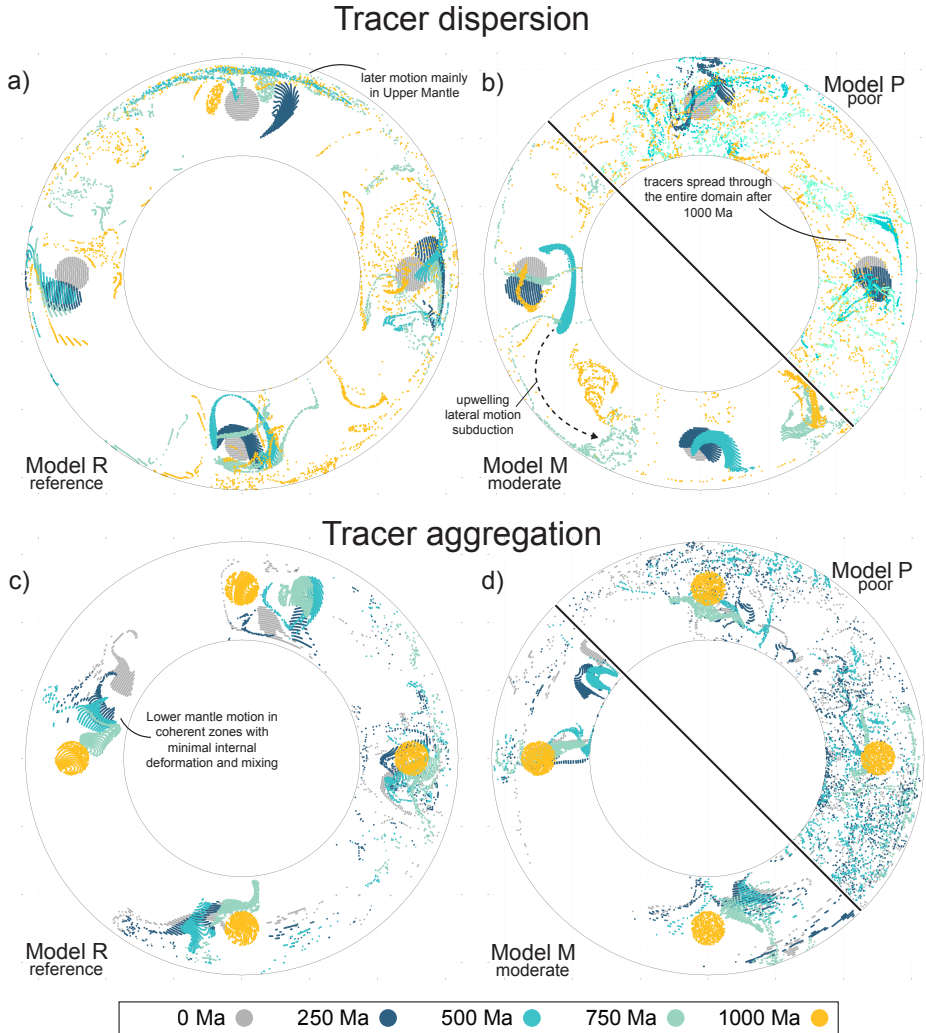
Figure 1.6 Motion of the mantle shown through individual tracers in 250 Ma steps. Tracers that move from (disperse) or move to (aggregate) four pre-defined circles. **a-b** Tracer dispersion and **c-d** aggregation for the Reference model (model R) with good fit to the data and models M and P with a Moderate and Poor fit.

mixing. After 1000 Ma, tracers are mixed throughout the mantle and are more randomly distributed over the entire mantle domain as compared to models R and M (Figures 1.6a,b).

The same holds for the aggregating tracers of model P. At 0 Ma the tracers that will end up in the four yellow circular regions after 1000 Ma of mantle evolution are distributed throughout the entire mantle. After 750

Ma of convection only part of those tracers have aggregated into irregular shaped zones (Figure 1.6d). This means that in the last 250 Ma significant mantle motion must still occur to form final tracer configuration of yellow circular regions.

This is entirely different in the more viscous model M, which shows a convective vigour where many tracers at 0 Ma already form irregular shaped closely packed clouds of tracers. Over time those tracer clouds will further deform into their final circular shape at 1000 Ma. This shows that their original mantle composition is being preserved (Figure 1.6d), i.e., with limited or no mixing. In the last 500 Ma of convection in model M, most tracers reside in the lower mantle and are within 3000 km of their final destination, giving a maximum non-slab lower mantle flow rate of 6 mm/a. Model R's convective pattern is even slower, most of the aggregating tracers have moved coherently since 0 Ma and seem to never enter the upper mantle and their average distance travelled is lower than 4000 km in 1000 Ma of convection giving an averaged flow speed of less than 4 mm/a (Figure 1.6c).

After 500 Ma, model R has large accumulations of subducted initial lithosphere near the CMB while the removed lithosphere at the surface has been formed out of material that mostly originated from the initial upper mantle (Figure 1.7a). Adjacent to the piles of subducted initial lithosphere at the CMB, lower mantle material has started upwelling, but most parts of the lower mantle still have retained their initial internal structure. Model M shows similar features of lower mantle evolution, although the upper mantle is more mixed, especially below the collided continental keels (Figure 1.7b). In contrast, after 500 Ma in Model P, the subducted lithosphere material is much less accumulated near the CMB and has been mixed upward by return flows leading to preservation in slivers throughout the lower mantle, albeit near their subduction location. And although the lower mantle is not well-mixed after 500 Ma, it does not show the propensity of preserving large coherent areas of 'primordial' mantle structure as seen in the other two models. The lower mantle experiences more deformation and more zones of upwelling bring material from the lowermost mantle to the surface (Figures 1.7b, 1.8a). 18% of all tracers have been entrained in the lithosphere at least once and 40% of the lower mantle material has remained there after 500 Ma (Figures 1.8a,b). In models M and R, these ratios are equal with 13% of tracers that have been part of the lithosphere while more than 45% of tracers remained in the lower mantle (Figures 1.8c-f).

After 1000 Ma of subduction and convection the differences between model P, and the models R and M have increased. Model P shows no tendency for preservation of large regions of primordial mantle (less than 10%;
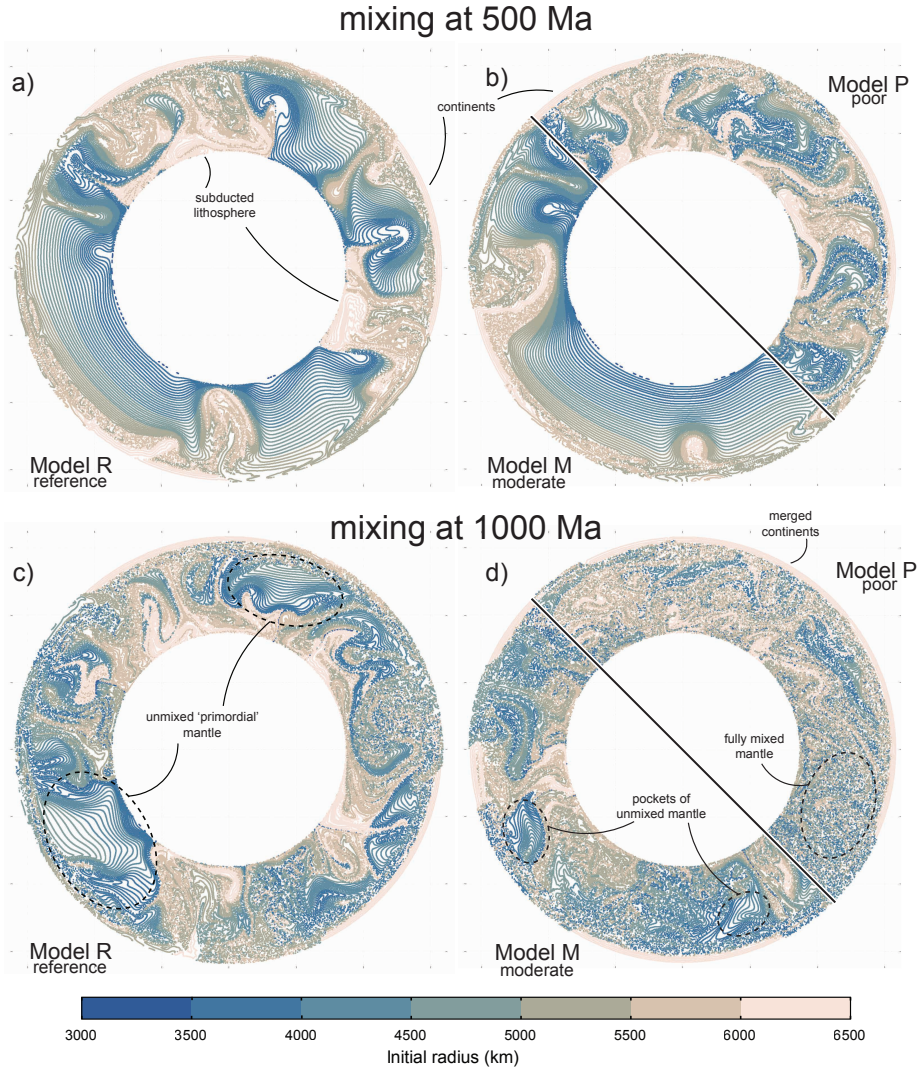
Figure 1.7 Mixing of the mantle for the three models at 500 and 1000 Ma of simulated convection. Shown are all tracers within each model coloured by their radius at $t = 0$ Ma.

Figure 1.8b) as the mantle is largely mixed and initial lithosphere material has been stirred through the entire mantle with only a few stretched slivers remaining (Figures 1.7d, 1.8a and Supplementary Movie 6). For model P, more than 40% of tracers have been part of the lithosphere during the model evolution, indicating a high degree of mixing (Figure 1.7, 1.8b). Model R contains preserved zones of mixed mantle as well as zones of unmixed, 'primordial' mantle. The initially subducted lithosphere has been

pushed around near the CMB and in the lower mantle while occasionally also brought back to the surface through plume-like upwellings (Supplementary Movie 4). The unmixed zones preserve their original internal structure, have varying sizes and occur at all depth in the lower mantle (Figures 1.7c, 1.8e). Here, about 25% of the tracers have been preserved in the lower mantle while only 20% has been entrained in the lithosphere (Figure 1.8f). Finally, model M has a similar preservation as model R although the preserved unmixed mantle is less abundant (only 13%; Figure 1.8d), and the zones are smaller (Figures 1.7d, 1.8c). Pockets of unmixed mantle can enter the upper mantle but are then fast entrained in lateral 'surface' flow, like plate motions, before being mixed back into the mantle during subduction (Supplementary Movie 5).

1.5 Discussion

Our experiments illustrate that average slab sinking rates are strongly linked to the long-term vigour of mantle convection. Models with lower slab sinking rates showcase a low propensity for mixing by mantle flow such that large and slowly deforming regions in the mantle remain unmixed after 1000 Ma of mantle evolution (Figures 1.7c, 1.8e). Using average slab sinking rates as an additional constraint that needs to be matched by geodynamic models provides a promising opportunity to advance to more 'Earth-like' mantle models with better determined mantle viscosity, and mantle flow and mixing properties.

We deliberately use simplified models and parameters because we primarily aim to demonstrate the benefit of using the inferred average slab sinking velocity for narrowing the range in the vigour of mantle convection. The lower mantle viscosity of our preferred model (model R) is on the high-end of the estimated ranges (Mitrovica and Forte, 2004; Steinberger and Calderwood, 2006; King, 2016) but similar to other recent geodynamic studies (Figure 1.1) (Čížková *et al.*, 2012; Rolf *et al.*, 2018; Gülcher *et al.*, 2021; Flament *et al.*, 2022). However, most of these studies use a decreasing thermal expansivity and increasing thermal conductivity with depth, which both lead to a smaller density contrast between slab and mantle and thus a gradual reduction of slab buoyancy with depth (Tosi *et al.*, 2013). Qualitatively, to match the inferred sinking rates, a gradual reduction in slab buoyancy would generally imply a gradual depth-dependent reduction of the mantle viscosities. This may explain our higher lower mantle viscosity, roughly by a factor 2, than the first study matching slab sinking rates (Čížková *et al.*, 2012), although we also assess a broader spatial and temporal spectrum of subducted slabs than a single slab system as in (Čížková
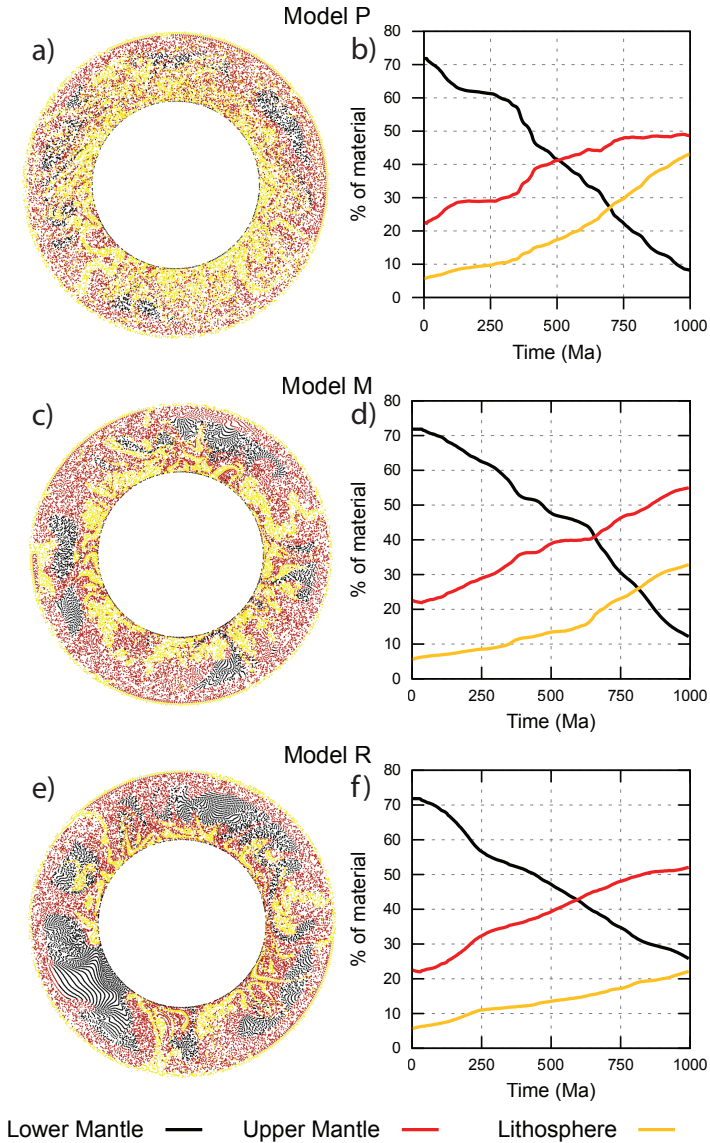
Figure 1.8 Mixing of the mantle of the three models at 1000 Ma (**a,c,e**) and the relative abundance of three compositions (**b,d,f**). The compositional distribution is based on radius of the tracers, with the Lower Mantle (black) below 660 km, Upper Mantle (red) below 100 km and lithosphere (yellow) in the top 100 km. Lower mantle tracers can get entrained in the upper mantle and subsequently in the lithosphere but not visa-verse. Therefore, the percentage of lower mantle material can only decrease and the percentage of lithosphere material can only increase.

et al., 2012). We do not expect that when the slab buoyancy is reduced, due to the decreasing thermal expansivity and increasing thermal conductivity, the convective vigour of our models will change, as we would tune our preferred viscosity profile to comply to the same average sinking rates.

Other rheological simplifications in our models are that chemical or compositional heterogeneities that are present in the Earth's mantle are not represented in our experiments. Our slabs have the same rheological properties as the bulk mantle, and once the negative buoyancy that makes our slabs sink disappears by thermal conduction, they assimilate to the warm mantle and do not inherit any density or chemical signal as recycled oceanic crust in the model. In reality, also thermally assimilated slabs are likely still compositionally distinct from the bulk mantle (Lambart *et al.*, 2019; Jones *et al.*, 2021). The same holds true for primordial mantle material, which is compositionally distinct from bulk mantle (Jackson *et al.*, 2021). This may be one of the reasons why thermochemical structures, such as LLSVPs or ULVZs that are probably not purely thermal features (Garnero *et al.*, 2016; Koelemeijer *et al.*, 2017; McNamara, 2019), do not develop in our models. Nonetheless, it is interesting to evaluate how mixing and motion behaviour in our reference model R, that is successfully tuned to slab sinking kinematics, compares with models that address current debates on Earth's interior dynamics, like LLSVP stability, mantle heterogeneity, or plume dynamics (Mulyukova *et al.*, 2015; Arnould *et al.*, 2020; Cao *et al.*, 2021; Gülcher *et al.*, 2021; Jones *et al.*, 2021; Flament *et al.*, 2022).

The fate of subducted oceanic lithosphere might be strongly connected to structures in the lower mantle, as they may form thermochemical piles on the CMB (Jones *et al.*, 2021) that may overlap with or correspond to LLSVPs or ULVZs (Dobson and Brodholt, 2005; Ballmer *et al.*, 2016). Our models R and M seem to preserve former slabs in thick piles on the CMB (Figures 1.7a,b). These modelled piles are strongly tied to the convective vigour of the mantle rather than being a characteristic feature of our slabs. For instance, in model P, with high sinking rates of 40-60 mm/a, such piles do not form (Figure 1.7b). We observe that in parts of the model without actively sinking slabs, mantle flow is minimal, allowing preservation of more or less stagnant piles of subducted lithosphere, even though in our models subducted material is not compositionally distinct. We foresee that adding compositional heterogeneity to our models may further enhance this behaviour.

Because of the, purely thermal, density differences in slabs, the piles on the CMB do move and get entrained in mantle flow, whereby mantle flow is controlled by slab sinking and close to the CMB by horizontal slab

motion (Figures 1.7c,d). In models R and M, horizontal slab motion in the lower mantle is limited and slabs sink nearly vertically (Figure 1.4b; Supplementary Figures 2-3), and thus only interact with the ambient mantle in their direct surroundings. The average velocity of the lowermost mantle (bulk mantle and slabs) in model R is lower than 4 mm/a, well below the sinking rate of slabs. The slowly convecting mantle in our models provides a straightforward explanation for the stability of lowermost mantle structures including the LLSVPs (Burke and Torsvik, 2004; Torsvik *et al.*, 2010; Torsvik *et al.*, 2014) and slab graveyard compositions (Jackson and Macdonald, 2022) that follow from kinematic correlations.

Conversely, our model P, with higher sinking rates, also has faster horizontal slab motions, with standard deviations around 20 mm/a, three times higher than in model R. In that respect, the rates of sinking and mantle flow in model P resemble those in model experiments that were used to argue for strong horizontal motions of slabs in the mantle, which in turn would be able to shovel lower mantle structures such as LLSVPs along the CMB (Cao *et al.*, 2021; Flament *et al.*, 2022; Lin *et al.*, 2022; Peng and Liu, 2022). The comparison between our models P and R suggests that tuning models to reconstructed slab sinking behaviour may strongly influence the conclusions on lower mantle mobility and horizontal slab motion during sinking.

Finally, it is interesting to note that even after a billion years of subduction and convection the mantle in our experiments tuned to slab sinking rates preserve large blobs of unmixed, 'primordial' mantle. These are in the heart of major, slow, mantle convective systems in the lower to mid-mantle (Figure 1.7c). These primordial provinces in our experiments resemble structures that were proposed before as compositionally distinct zones that could be more rigid (Ballmer *et al.*, 2017; Gülcher *et al.*, 2020). In our experiments, provinces of subducted lithosphere forming piles and primordial provinces forming mid-mantle blobs simply result from the slow bulk mantle convection rate that results from tuning the model against slab sinking. This illustrates that much lower mantle convection rates than typically generated in numerical models may explain many of the outstanding puzzles on long-lived structural and compositional heterogeneity. Adding further complexity to mantle convection models, such as compositional, thermal and depth variations of thermal conductivity and expansivity (Tosi *et al.*, 2013; Guerrero *et al.*, 2023) and compositionally dependent viscosity in the lower mantle (Yamazaki and Karato, 2001; Ballmer *et al.*, 2017; Gülcher *et al.*, 2021) may further enhance the patterns we observe in our experiments, as the rheological contrast between different compositions may influence the mixing behaviour (Manga, 1996). Our models are based on

the commonly used linear diffusion rheology of the lower mantle. This does not include shear localization as a local agent for mantle mixing. Propositions for nonlinear lower mantle rheologies are few (e.g., Girard *et al.*, 2016; Cordier *et al.*, 2023) and how these would impact mantle flow and mantle mixing is yet to be established. Arguably, if shear localization would occur around sinking slabs ten this would decouple slab sinking from the ambient mantle to a higher degree than in our models with linear rheology and thus could lead to a lower mixing of the ambient mantle than modelled here.

Nonetheless, our results, with a compositionally homogeneous mantle, show that tuning geodynamic models to match the average slab sinking rates for the last 250 Ma provides a novel avenue towards explaining the survival of large, primordial mantle reservoirs. Furthermore, models with too high slab sinking rates might systematically overestimate bulk mantle flow and the vigour of convection. This suggests that adding new kinematic correlations between geochemistry, seismology, and geology as constraint on mantle convection models is an important step in improving our dynamic models and their predictive value.

1.6 Conclusions

In this study, using 2D cylindrical mantle modelling, we have explored how the recent inferred average slab sinking rates can help narrow determining the long-term average magnitude of mantle flow velocity and the propensity for mantle mixing. Models with low mantle slab sinking rates of $10 - 15$ mm/a have very limited bulk mantle motion, of only a few mm/a, and after 1000 Ma of subduction evolution and mantle convection these models preserve large zones of unmixed regions in the mid-mantle. Therefore, the addition of new inferred kinematic observations or constraints to mantle convection models can provide avenues to explain the magnitude and pattern of mantle convection and the large-scale preservation of geochemical mantle reservoirs.

2

Quantifying mantle mixing through configurational Entropy

Erik van der Wiel
Cedric Thieulot
Douwe J.J. van Hinsbergen

Abstract

Geodynamic models of mantle convection provide a powerful tool to obtain insights into the structure and composition of the Earth's mantle that resulted from a long history of differentiating and mixing. Comparing such models with geophysical and geochemical observations is challenging as these datasets often sample entirely different temporal and spatial scales. Here, we explore the use of configurational entropy, based on tracer and compositional distribution on a global and local scale. We show means to calculate configurational entropy in a 2D annulus and find that these calculations may be used to quantitatively compare long-term geodynamic models with each other. The entropy may be used to analyze, with a single measure, the mixed state of the mantle as a whole and may also be useful to validate numerical models against local anomalies in the mantle that may be inferred from seismological or geochemical observations.

2.1   Introduction

Mantle convection models that are used to simulate the evolution and dynamics of the solid Earth are built on different sets of observations each providing their own constraints to validate the state of the mantle through time (e.g., Gerya, 2014; Dannberg and Gassmöller, 2018). For instance, with the advent of full-plate kinematic reconstructions of the past 100s Ma (e.g., Domeier and Torsvik, 2014; Merdith *et al.*, 2021), mantle models can now be driven by plate motions through geological time (e.g., Heister *et al.*, 2017; Coltice and Shephard, 2018; Flament *et al.*, 2022). Such experiments then lead to a prediction of the structure and composition of the mantle that may be compared to geological, geochemical, or seismological observations from the modern Earth (e.g. Bower *et al.*, 2015; Yan *et al.*, 2020; Flament *et al.*, 2022; Lin *et al.*, 2022; Li *et al.*, 2023).

Key observables of the modern Earth that may be predicted by models are anomalies in mantle structure or composition that result from mantle mixing, or absence thereof. For instance, seismic tomography provides images of the present-day mantle as relative slow and fast regions in terms of seismic wave propagation, which can relate to variations in temperature and/or composition such as slabs or mantle plumes (Koelemeijer *et al.*, 2017; Ritsema and Lekić, 2020). The heterogeneity of the Earth's mantle is also reflected in geochemical observations of magmatic rocks, oceanic island basalts (OIB) and mid-oceanic ridge basalt (MORB), which suggest the existence of depleted, enriched, and even primordial mantle reservoirs, i.e. un-

mixed regions that maintain a geochemically distinct composition (Jackson *et al.*, 2018; McNamara, 2019; Stracke *et al.*, 2019; Jackson and Macdonald, 2022). Notably, seismological and geochemical heterogeneities may entirely, partly, or hardly overlap, and observations may relate to entirely spatial and temporal scales. Seismology reveals seismic velocity anomalies in the mantle on scales of 100s to 1000s of km, varying from slabs to LLSVPs (e.g., Ritsema *et al.*, 2011; Garnero *et al.*, 2016; van der Meer *et al.*, 2018). Geochemical differences between MORBs from the Atlantic, Pacific and Indian Ocean indicate compositional heterogeneity on a hemispheric scale (Dupré and Allègre, 1983; Hart, 1984; Doucet *et al.*, 2020; Jackson and Macdonald, 2022), geochemical zonation within a single plume system is evidence for heterogeneities on a 100 km scale (Hoernle *et al.*, 2000; Weis *et al.*, 2011; Gazel *et al.*, 2018; Homrighausen *et al.*, 2023), whereas micro-scale analysis reveals even major variations between samples (Stracke *et al.*, 2019). All such variations may result from a cycle of geochemical differentiation and renewed mixing that is associated with mantle convection and that eventually may be predicted by mantle convection models. To this end it is important to also be able to define or quantify the mixed state of the modern mantle from a suitable numerical mantle convection model over the relevant range of spatial scales.

Here, we investigate the merits of configurational (or 'Shannon') entropy for quantifying compositional mixing of particles through flow on a global or local scale (Shannon, 1948; Camesasca *et al.*, 2006; Naliboff and Kellogg, 2007). We develop the application of configurational entropy to the 2D cylindrical mantle convection models which we recently developed (Chapter 1), implementing measures for local and global entropy of mixing that incorporates information on composition. We aim to use configurational entropy to quantify the degree of mixing on different scales for different hypothetical initial compositional configurations of the mantle and evolution thereof over time. Subsequently, we discuss how configurational entropy may be used as a bridge for quantitative comparison between mantle convection models and geological, seismological, or geochemical observations.

2.2   Methods

2.2.1   Mixing Entropy

Configurational Entropy (Shannon, 1948) describes how fast information on compositional particle distribution is lost through flow. It is widely used and has a large variety of applications, including fluid or magma mixing (Camesasca *et al.*, 2006; Naliboff and Kellogg, 2007; Perugini *et al.*, 2015),
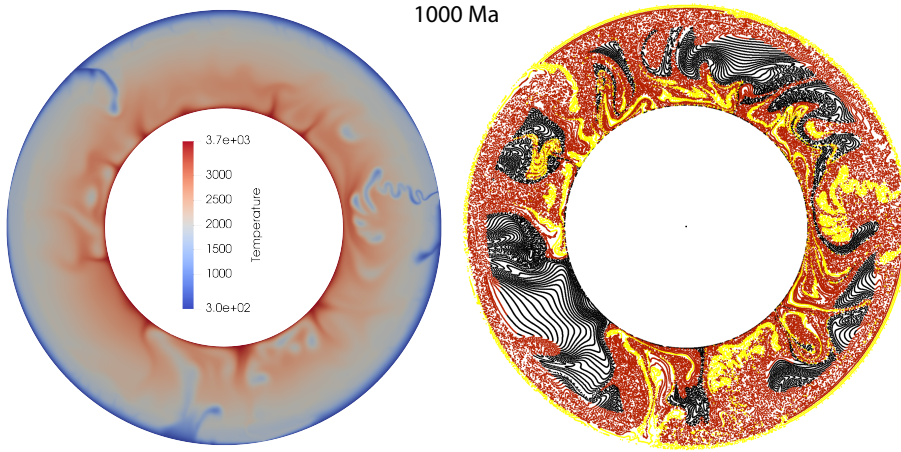
Figure 2.1 Snapshot from model R at $t = 1000$ Ma showing the temperature field in Kelvin (left) and passive particles colored by composition (lithosphere: yellow, upper mantle: red, lower mantle: black).

transport of plastic in oceans (Wichmann *et al.*, 2019), distribution of seismicity in earthquake populations (Goltz and Böse, 2002), or the quantification of uncertainty in geological models (Wellmann and Regenauer-Lieb, 2012).

The definition of the entropy S is based on the probability of a particle distribution in a domain tessellated by non-overlapping cells. For this we use passive particles, or tracers, that are advected in a flow model leading to particle trajectories. The entropy depends on the distribution of particles, the number of cells and the initial compositional distribution (see section 2.2.3). Let C be the number of compositions and M the number of cells in the domain. The entropy is calculated based on the discretized particle density $\rho_{c,j}$ (Equation 2.1), i.e., the amount of particles of composition c in cell j,

$$\rho_{c,j} = \frac{n_{c,j}}{N_c} \tag{2.1}$$

where N_c is the total number of c-particles divided by the number of cells M. This assumes that cells are of equal area, which will be used here in our 2D application. Hence, N_c is the same for all cells. From the compositional density $\rho_{c,j}$ we calculate the conditional probability $P_{j,c}$ for finding a group of particles of composition c in cell j through equation (2.2)

$$P_{j,c} = \frac{\rho_{c,j}}{\sum\limits_{c=1}^{C} \rho_{c,j}} \tag{2.2}$$

and as well the probability for the cell-sum of compositional densities P_j by equation (2.3),

$$P_j = \frac{\sum\limits_{c=1}^{C} \rho_{c,j}}{\sum\limits_{j=1}^{M} \sum\limits_{c=1}^{C} \rho_{c,j}} \tag{2.3}$$

Next, equation 2.4 defines the global entropy S_{pd} of the particle distribution.

$$S_{pd} = -\sum_{j=1}^{M} P_j \ln P_j \tag{2.4}$$

which quantifies the global spatial heterogeneity of the particle distribution independent of composition (Naliboff and Kellogg, 2007). At the cell level, the local entropy S_j for cell j can be defined for the mixture of particles with different compositions:

$$S_j = -\sum_{c=1}^{C} P_{j,c} \ln P_{j,c} \tag{2.5}$$

Finally, the global entropy S of the particle distribution, accounting for composition, is the weighted average of P_j (equation 2.3) and the local entropy S_j (equation 2.5) through Equation (2.6) (Camesasca *et al.*, 2006).

$$S = \sum_{j=1}^{M} P_j S_j \tag{2.6}$$

Maximum entropy is achieved when all particle densities $\rho_{c,j}$ are equal, i.e., the distribution of composition and number of particles are the same in each cell. Each entropy above has a different maximum which depends on either the number of cells for (S_{pd}) or the number of compositions used (for S and S_j). To compare entropies between mixing models with different initial conditions, we normalize the entropies by dividing each by its maximum. The maximum for S_{pd} is equal to $\ln M$, while for S_j and S the maximum is $\ln C$ (Camesasca *et al.*, 2006). This provides values for all entropies between the endmembers 0 (entirely segregated composition)

Chapter 2

and 1 (uniformly mixed). The maximum value for S_{pd} can only be reached when all compositions are present in equal ratios. Entropy calculations of four simple educational examples are shown and explained in appendix A to help the reader appraise these quantities.

2.2.2 Mantle convection model

We apply the configurational entropy to the quantification of mixing in a recently developed 2D numerical mantle model in a 2D cylindrical geometry that simulates 1000 Ma of ongoing mantle convection and subduction (Chapter 1). The convection model was designed to evaluate the sensitivity of inferred lower mantle slab sinking rates (van der Meer *et al.*, 2018) to the vigor of mantle convection. The simulations comprised dynamically
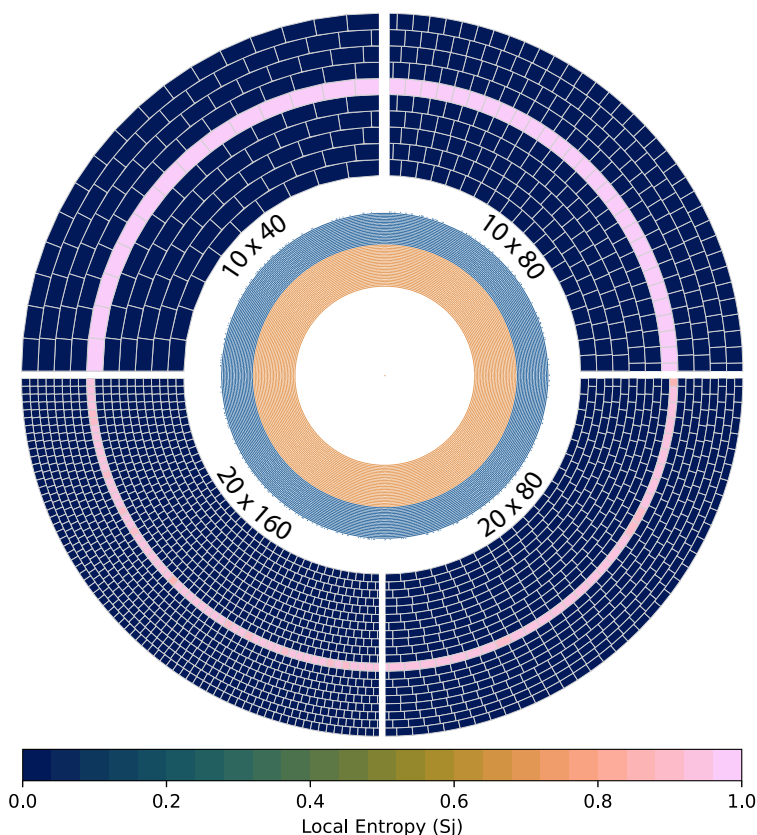

Figure 2.2 Representation of the various tested resolutions. Shown is the initial ($t = 0$ Ma) particle distribution (inner annulus) and local entropy S_j (outer annulus) for the static 50/50 composition distribution (case A). The cells with a high S_j (pink) indicate that both compositions are present, the unmixed cells (blue) contain only one composition.

self-consistent one-sided subduction below freely moving, initially imposed, continents at the surface, culminating in slab detachment followed by sinking of slab remnants across the lower mantle (Figure 2.1). Model plate motions were in the range of reconstructed values (Zahirovic *et al.*, 2015) and average slab sinking rates could be obtained in the range of those that were inferred from correlations between the location of imaged lower mantle slabs and their geological age (van der Meer *et al.*, 2018). This modelling qualitatively illustrated the degree of mixing in a modelled mantle and the potential preservation of an unmixed primordial, unmixed advected (e.g., subducted), or (partly) homogenized, mixed mantle shown by the distribution of particles.

We quantify the degree of mantle mixing in the model by investigating the local and global mixing entropies (Section 2.2.1) for model R of chapter 1 at different resolutions. We also illustrate how mixing entropy quantifies the mixing of a different model (model P) that showed significantly higher slab sinking rates than inferred for the lower mantle and that displayed a higher degree of mantle mixing (Chapter 1). For this purpose, we only used the passive particle distribution available from the models in chapter 1. The cells used to calculate the configurational entropy (see section 2.2.4) are independently substantiated and therefore not the same as used in the numerical model, for any additional information of these models we refer the reader to chapter 1.

2.2.3 Initial composition

To illustrate how we track compositional evolution with configurational entropy, we assign a compositional distribution to our example models with two different approaches. In case A, we assign a compositional distribution in the initial model, and each tracer will keep its initial composition through time. We divide the annulus in two concentric parts at a radius of 5100 km and assign the inner and outer part a different composition (simply put: a different color). This creates a 50-50 ratio between the number of particles of each composition. Case B uses dynamic compositions, i.e., the composition of a particle may change over time. We use three compositions whose relative ratios are allowed to change over time depending on the particle's depth in the model. Initially, we define particles as lower mantle when they start below 660 km depth in the model, upper mantle if they start between 100 and 660 km, and lithosphere if between 0 and 100 km depth. Particles keep their 'lower mantle' composition as long as they do not ascend above the 660 km during model evolution. Any particle that moves from a deeper reservoir into a shallower one will see its composition changed to the

shallower reservoir and will maintain this composition for the remainder of model time. This approach is an example that may be used in a study to characterize the secular geochemical differentiation of the solid Earth.

2.2.4   Cell distribution

Entropy as calculated in this study also depends on the number and distribution of cells, which is independent of the mesh used in the numerical model itself. To ensure an approximately equal cell-area throughout our domain, we vary the number of cells per radial layer. The cell-area is determined by the product of the radial extent δr and lateral extent $\delta\theta$ that follows from the number of radial layers and the number of cells along the core-mantle-boundary (CMB) circumference. Varying cell-area may be important to compare the outcome of a numerical model with datasets that have very different resolutions (e.g., seismology versus geochemistry). We illustrate different cell resolutions with our 2D example model, but a similar approach may be used for a 3D model albeit with a different tessellation (Thieulot, 2018). The lowest resolution (10x40) contains 40 cells along the CMB, increasing across the 10 layers to 68 cells along the surface, for a
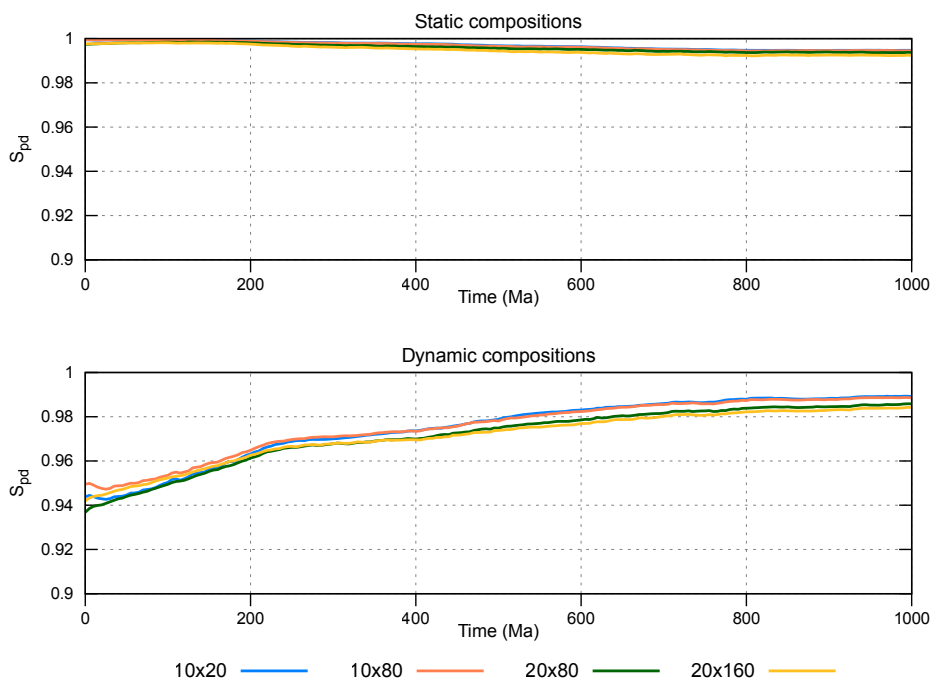

Figure 2.3 Time evolution of S_{pd} for the static (case A) and dynamic (case B) composition distributions of the four used resolutions.

global total of 539 cells (Figure 1.2). The highest resolution that we illustrate (20x160) then gives a global total of 4430 cells (Figure 2.2). The numerator $\rho_{c,j}$ for the probability calculations (equations 2.2 & 2.3) for cells that do not contain a particle ($\sum_{c=1}^{C} \rho_{c,j} = 0$) would cause a problem in its contribution to the entropy. Note that $\lim_{x \to 0}(x \ln x) = 0$, therefore cells without a particle do not add to any of the entropies, these cells are skipped in practice in the summation of equations (2.4-2.6).

2.3 Results

In this section, we describe the various obtained entropies. Starting with the particle distribution S_{pd}. Next, we underline the importance of resolution for the local entropy S_j in our example model at different resolutions for the static composition distribution (case A) and show how the local entropy evolves over time. Finally, we show the temporal evolution of the global entropy S for this model, which is also influenced by resolution and compositional choices before we elaborate on the use of dynamic compositions (case B, section 2.3.4).

2.3.1 Global particle distribution (S_{pd})

A total of 96,000 of particles are initially distributed in a regular pattern (Figure 2.2), equally spaced throughout the annulus. Over time, these particles are passively advected and their spatial distribution thus changes. The large number of particles in the initial distribution provides a good coverage in all cells as quantified by the normalized global entropy of particle distribution S_{pd} which is at the modelling start close to 1 for both cases A & B at the start (Figure 2.3). As the initial composition ratios of case B are not equal (about 72% lower mantle, 25% upper mantle, and 3% lithosphere) S_{pd} is not 1 as for case A, but 0.95, still indicating that particles are distributed equally.

Over time, as particles are advected, the S_{pd} does not change significantly for case A in which particles cannot change composition, but it does change for case B (Figure 2.3). This is caused by the secular change in composition ratios in case B (See figure 1.8). S_{pd} increases due to the increased percentage of lithosphere and upper mantle particles in the domain. We tested the effect of cell resolution on S_{pd} for both cases, which does not show significant differences (Figure 2.3). This indicates that the number of particles used in our calculations is sufficient, also for our highest resolution (20x160).
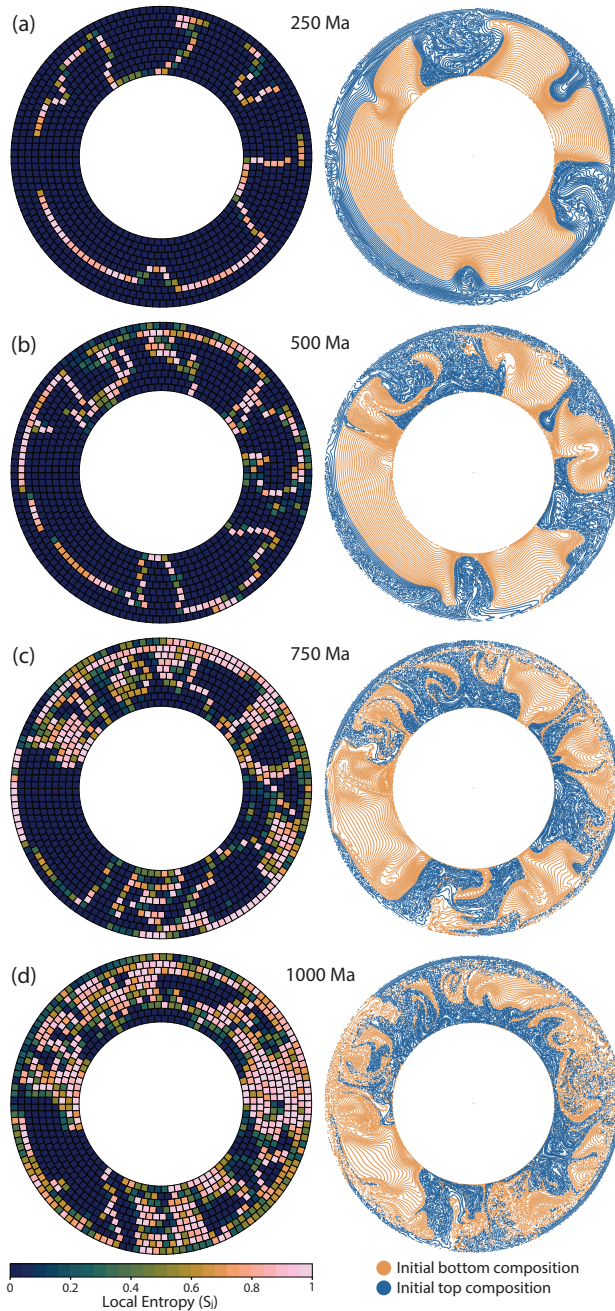
Chapter 2

Figure 2.4 Local Entropy S_j (**left**) and particle distribution (**right**) at 250 Ma intervals of the model (model R of Chapter 1) with a static 50/50 ratio particle composition (case A) at a resolution of 10×80 cells.

2.3.2 Local entropy (S_j)

A local entropy of 1 means that the ratio of particle compositions within a cell is equal to the global composition ratio, e.g. in the initial distribution for case A (Figure 2.2). $S_j = 0$ indicates that all particles in a cell have the same composition, although it does not indicate which composition. We illustrate the temporal evolution of particle distribution in 250 Ma steps (Figure 2.4) for which we use the static particle composition ratio of case A and a cell resolution of 10x80 at the CMB (Figure 2.3). After 250 Ma of convection evolution the initial distribution is undisturbed in most parts of the domain. The two compositions are only displaced since the onset of convection, but barely mixed. Mixing is concentrated around two major zones of downwelling where a narrow zone of single cells shows a local entropy S_j that is non-zero (Figure 2.4a).

At 500 Ma, some of the sharp boundaries between the two compositions have moved and a mixed boundary zone formed locally, reflected by the broader zone of non-zero local entropy (Figure 2.4b). After 750 Ma, most of the upper mantle (top three cells) has $S_j > 0$ and zones in the lower mantle are mixed as well (Figure 2.4c): the two starting compositions have been displaced and mixed through the mantle. At the end of the model, at 1000 Ma, the number of cells with non-zero S_j in the upper mantle has decreased further, the zones of fully ($S_j \approx 1$) mixed lower mantle have increased in area. However, there are still zones of unmixed ($S_j = 0$) composition present. Unmixed initial 'lower' composition is preserved mainly in the mid-mantle while unmixed initial 'upper' composition is preserved near the CMB, i.e., this material sunk and was displaced, but did not mix (Figure 2.4d).

Even though cell resolution does not significantly impact S_{pd} it does affect the local entropy S_j (and thus also the global entropy, see section 2.3.3). A smaller-sized cell mesh will have fewer particles per cell, which increases the likelihood of sampling particles of only one composition in zones with limited mixing, leading to zero local entropy. Doubling the angular resolution from 10x40 to 10x80 shows on a global scale a similar trend after 1000 Ma of convection: three zones of unmixed (low S_j) mantle separated by three zones of mixed mantle (high S_j) (Figure 2.5). However, it does show some increased detail in local entropy, mainly in the 'mixed' zones of the model (Figure 2.5). The large unmixed zones are of similar size for these two resolutions, although the ratio of cells with a low S_j compared to high S_j changed. The larger unmixed zones are composed of initial 'lower' composition (Figure 2.4d).
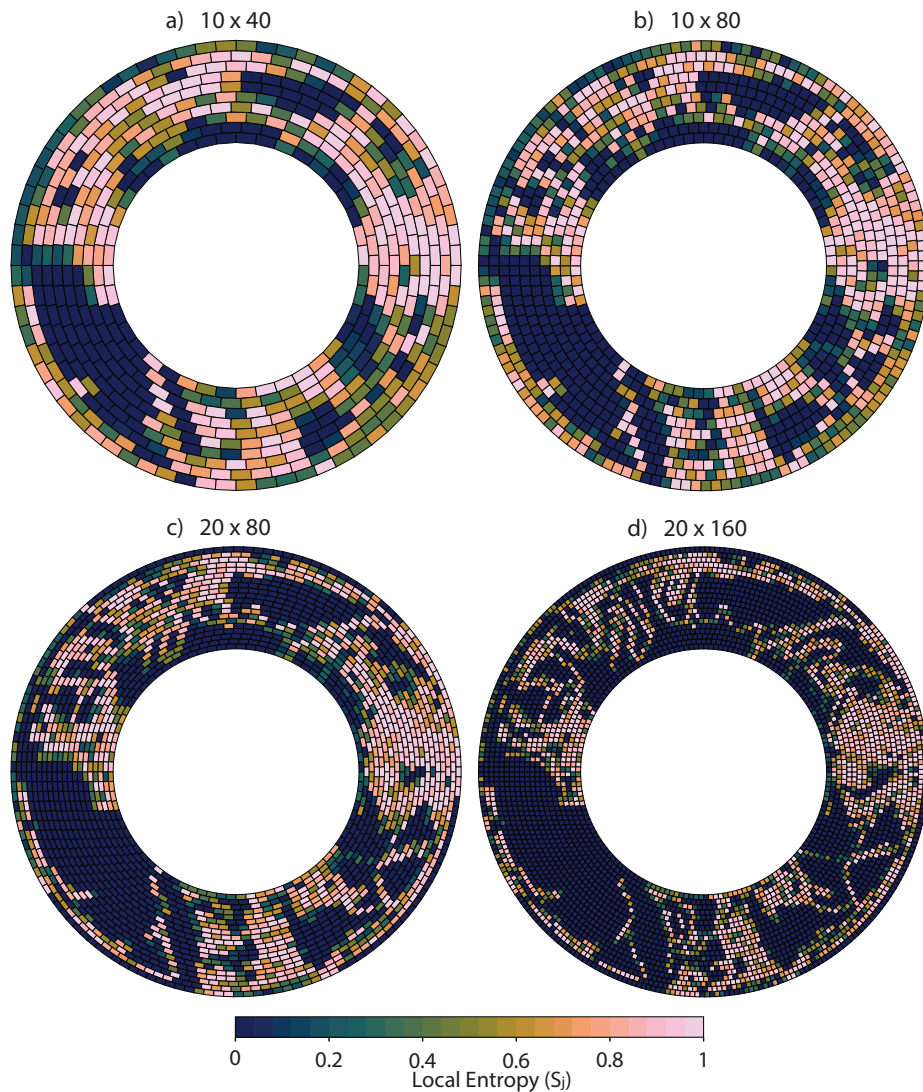
Chapter 2

Figure 2.5 Local Entropy S_j after 1000 Ma of mantle convection for the Reference model (Chapter 1) at four different resolutions of cells used to calculate the local entropy where **b** is identical as figure 2.4d.

A radial increase in resolution, from 10 to 20 cells across the domain, refines the calculation of local entropy. The number of cells with $S_j = 0$ becomes larger and increases the size of the three main unmixed zones. At this resolution, S_j resolves the 'continents': thicker portions of lithosphere that were initially placed in the model (See figure 1.2). The 20x80 resolution

has unmixed cells in regions that had high S_j at lower resolutions (Figure 2.5). Finally, with the 20x160 mesh resolution, zones of initial upper and lower composition (Figure 2.4d) show up as low S_j bounded by a single line of cells with high S_j (Figure 2.5). At this resolution the local entropy calculation resolves mantle structures such as the boundaries between slabs and ambient mantle, showing mantle structure mapped into the local entropy of mixing.

2.3.3 Global entropy (S)

The global entropy is a weighted average of the particle distribution probability P_j over cells and the compositional distribution within the cells S_j (Equation 2.6). Because the particle distribution irrespective of composition is almost equal to 1 in all tests (Figure 2.2, section 2.3.1), we may consider the entropy S as proxy for global compositional mixing. For the initial distribution of composition based on depth, almost all cells have a local entropy $S_j = 0$, apart from the cells that straddle the compositional boundary (Figure 2.2). This distribution is an unmixed state of the mantle and has a low global entropy, $S = 0.1$ for the resolutions with 10 radial levels and $S = 0.06$ for those with 20 radial levels (Figure 2.6). The lateral resolution does not matter for the initial distribution as the ratio of non-zero to zero S_j cells is the same.

While the mantle flow model evolves, compositions become more mixed and the global entropy increases depending on mesh resolution, whereby smaller cells have a higher probability to sample only one composition. Therefore, a higher resolution (smaller cells) yields a lower global entropy after 1000 Ma of mantle convection: the 20x160 resolution yields $S = 0.32$ while the 10x40 resolution yields $S = 0.51$ (Figure 2.6).

2.3.4 Case study: entropy with dynamic compositions

Case B, which has dynamic compositions that depend on compositional evolution in the model, presents a practical application of the configurational Entropy. We track the entropy as the compositional ratios evolve and mix over time. The total number of particles that have been part of the lithosphere and subducted increases over time as new lithosphere and slab is being created while the volume of material that stays in the lower mantle decreases. In our example model, after 1000 Ma, the initial volumes of 3% lithosphere, 25% upper mantle, and 72% lower mantle have changed to 25% with lithosphere 'composition', 50% upper mantle and 25% lower mantle. In this example, the dynamic composition implies that no lower mantle composition exists above the 660 km-discontinuity and the upper mantle cannot
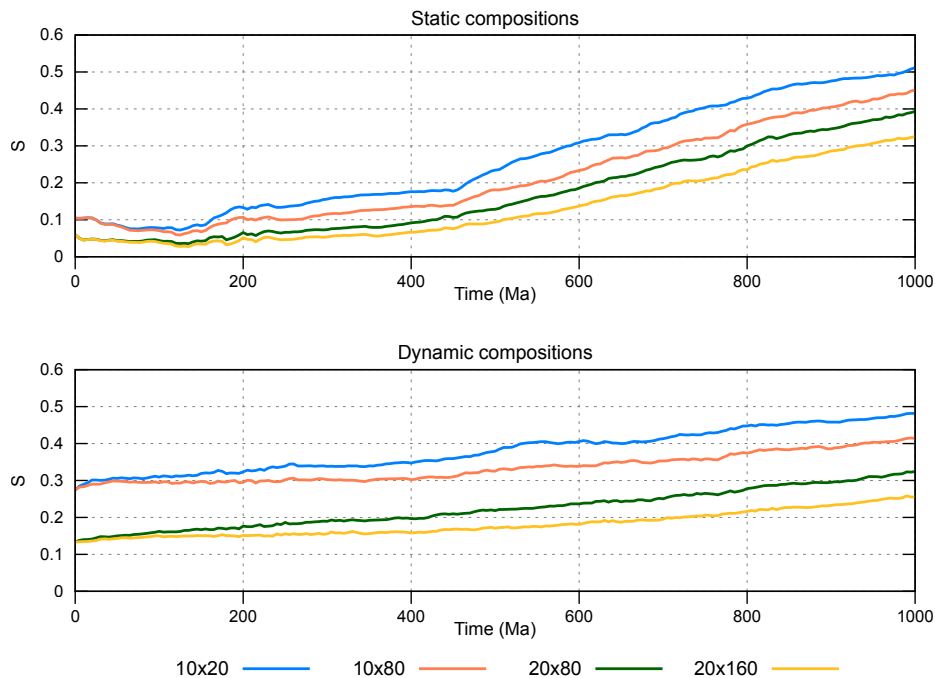
Figure 2.6 Global Entropy S of the model through time for different cell resolutions. **Top**: Case A (static compositions, **bottom**: case B (dynamic compositions).

have a local entropy of 1. However, in parts of the lower mantle the three compositions are mixed where high local entropy is present. The parts of the domain containing subducted lithosphere are better mixed, indicative of the convective mixing behavior of our model. With the highest mesh resolution we can resolve the upper- to lower-mantle boundary in the local entropy as well as active and past locations of subduction (Figure 2.7a).

The unmixed zones are of particular interest since they may provide direct information about compositions after 1000 Ma of convection. For all compositions there are cells with an unmixed signal, revealing the state of preservation of these compositions over time and over the whole domain. The entropy figures illustrate for instance the survival of unmixed original lower mantle material in the model, the fate of subducted lithosphere, and how upper mantle material is entrained downward during subduction (Figure 2.7a).

This case has an entirely different local entropy than the static composition distribution of case A (Figure 2.5). The dynamic case mainly focusses on the fate of subducted lithosphere rather than global mixing of the upper and lower part of the domain. As in the example with a static composition

(case A), the global entropy S for dynamic compositions is also cell-size-dependent. The initial global entropy is higher than for static compositions as there are now two compositional boundaries and over time the entropy only increases up to $S = 0.25$ for the 20x160 resolution. For the 10x40 resolution, $S = 0.48$ after 1000 Ma which is in the same range as the static two-composition example (Figure 2.6).

Finally, we use the dynamic composition to illustrate how changing the vigor of mantle convection changes the entropy. To this end, we compute the entropy after 1000 Ma using a model in which much higher sinking rates of subducted slabs occurred than inferred (model P - chapter 1) and that consequently has faster mantle flow. Figure 2.7b illustrates that this model is much more mixed after 1000 Ma of convection than in model R (Figure 2.7a). It has cells with a local entropy close to 1 throughout much of the domain, unmixed zones are smaller and located only in the top of lower mantle. Most of the local entropies are in the mid-mixed range. This is because only 10% of the original 'lower mantle' composition remains. Global entropy S equals 0.42 for this model at the 20x160 resolution, and even 0.60 for the 10x40 resolution, significantly higher than the reference model with dynamic composition (Figure 2.6). This example illustrates that the configurational entropy successfully quantifies mixing states in these models and is sensitive to overall changes in model behavior.

2.4   Outlook and conclusion

In this paper, we explore how configurational entropy may be applied to mantle convection models to quantify the degree of mechanical mixing, both on a local and global scale. Our results illustrate that entropy provides a way to track or map compositional heterogeneity over time using tracers or particles, which are commonly available in geodynamical models. Depending on the complexity of numerical models, any information that is stored on these tracers can be used to differentiate between 'compositions' used in the entropy calculations. The mantle convection models that we used to illustrate the use of configurational entropy were designed as numerical experiments to evaluate whether slab sinking rates scale with the vigor of mantle convection and mixing and did not aim to make a direct comparison between model and the real Earth. However, for models that do, i.e. kinematically constrained by reconstructed plate motions and aiming to resemble Earth-like features (e.g., Faccenna *et al.*, 2013; Bull *et al.*, 2014; Coltice and Shephard, 2018; Flament *et al.*, 2022; Lin *et al.*, 2022; Li *et al.*, 2023) configurational entropy may serve as a means to quantify and map the degree of mixing, and hence to determine average cell composition, on
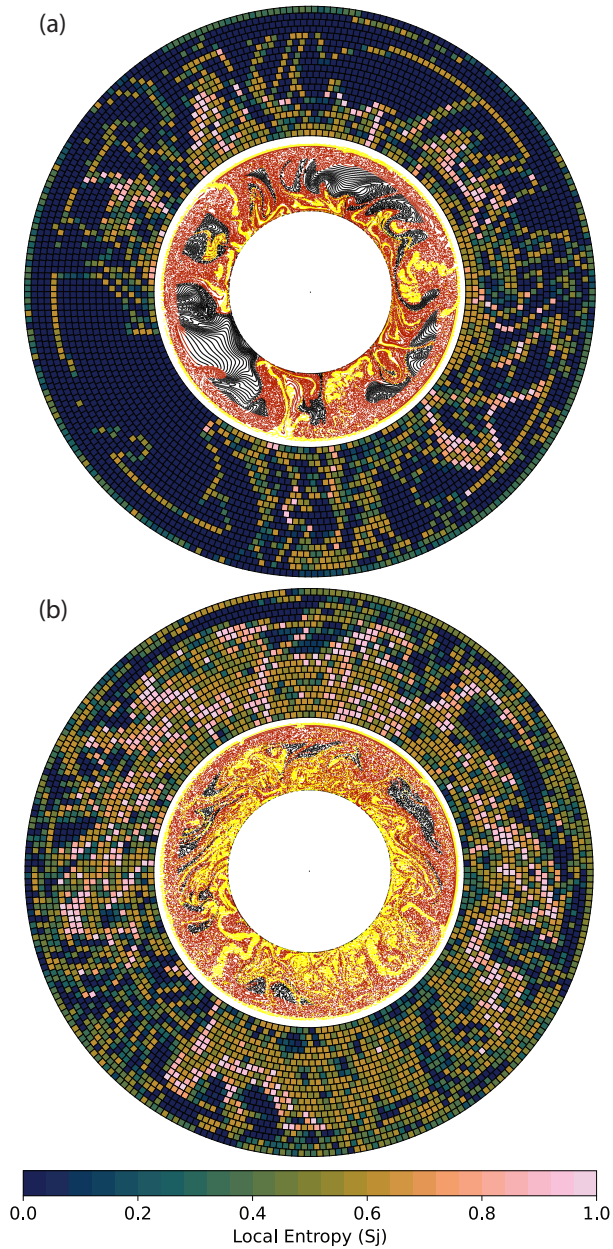
Chapter 2

Figure 2.7 Local Entropy S_j with a 20×160 resolution (outer annulus) and particle distribution (inner annulus) for dynamic compositions. Lower mantle (black), upper mantle (red) and lithosphere (yellow) compositions can change over time as function of depth. **a)** model R and **b)** model P with more vigorous convection of chapter 1 as described in section 2.3.4.

a local, regional or a global scale.

On a global scale, such models would for instance be able to track volumes of material that have remained in the lower mantle during the evolution of Earth (Figure 2.7). These volumes are of interest, because they could explain the geochemical detection of enigmatic primordial mantle, and feature in numerical models as the proposed bridgmanite-enriched ancient mantle structures (BEAMS) of (Ballmer *et al.*, 2017), or surviving in the slab graveyard (Jones *et al.*, 2021), or perhaps in LLSVPs or ULVZs (Deschamps *et al.*, 2012; McNamara, 2019; Vilella *et al.*, 2021; Flament *et al.*, 2022). In addition, the use of entropy calculations may show how subducted lithosphere may become stored in the mantle and to what degree original depleted and enriched crust, and slab material mix with upper and lower mantle rock. Particularly, dynamically changing compositions would benefit such studies, and in more sophisticated models that include geochemical evolution (e.g., (Dannberg and Gassmöller, 2018; Gülcher *et al.*, 2021), geochemical reservoirs can be quantified with configurational entropy.

At smaller scales, entropy in mantle modeling is useful to track mixing at the scale of a single subducting plate interacting with a mantle wedge, or a plume rising from the CMB. This may be done based on location solely (S_{pd}), to track the dispersal of an initial cloud of tracers in a slab or at the base of a plume (Naliboff and Kellogg, 2007), but also with the use of composition through S_j and S. For instance, it may quantify how different compositions of material from the lowermost mantle are entrained by a plume and how material entrained by that plume is mixed during its upward motion (e.g., Dannberg and Gassmöller, 2018). For instance, how material is mixed in the partially melting plume head, or in the partially melting upper mantle below a ridge, mixing on the scale of a magma chamber may also be mapped using configurational entropy, see Perugini *et al.*, 2015.

However, it may not yet be possible to numerically represent 3D mixing and motion processes on all the scales illustrated above. In the end, the dynamics driving mantle convection may force slow consumption and mixing away of primordial mantle by producing lithosphere and plumes and mixing the geochemically segregated remains of these back into the mantle. These processes lie at the basis for the widely recognized but still enigmatic geochemical reservoirs that are thought to reside in the lower mantle such as those of recycled continental crust (EM1, EM2), recycled oceanic crust (HIMU) (Yan *et al.*, 2020), recycled depleted lithospheric mantle (Stracke *et al.*, 2019), and remaining primordial mantle (Ballmer *et al.*, 2017; Jackson *et al.*, 2017; Gülcher *et al.*, 2020). These processes also culminate in the seismologically imaged mantle volumes of higher and lower seismic velocity,

or seismic attenuation, but the widely different scales at which geochemical and seismological observations are made poses a problem to link such observations. Numerical models may bridge these scales and eventually use our planets plate tectonic evolution to predict the geochemical reservoirs as tapped by volcanoes, and mantle structure as imaged by seismology. The configurational entropy in this paper may be helpful to quantitatively determine where numerical models may successfully predict these seismological and geochemical features.

3

Slab buckling as a driver for rapid oscillations in plate motion and subduction rate

Erik van der Wiel
Jakub Pokorný
Hana Čížková
Wim Spakman
Arie P. van den Berg
Douwe J.J. van Hinsbergen

Abstract

Plate tectonics is primarily driven by the constant gravitational pull of slabs where dense oceanic lithosphere sinks into the mantle at subduction zones. Under stable plate boundary configurations, changes in plate motion are then thought to occur gradually. Surprisingly, recent high-resolution Indian plate reconstructions revealed rapid (2 - 3 Ma) plate velocity oscillations of $\pm 50\%$. Here we show, through numerical experiments, that the buckling of slabs in the mantle transition zone causes such oscillations. This buckling results from the deceleration of slabs as they sink into the lower mantle. The amplitude and period of buckling-associated oscillations depend on average subduction velocity and transition zone accommodation space. The oscillations also affect the upper plate which may explain enigmatic observations of episodic deformation and fluid flow in subduction-related orogens. We infer that the slab pull that drives plate tectonics is generated in just the top few hundred kilometers of the mantle.

3.1 Introduction

Plate kinematic reconstructions provide the quantitative constraints that underpin our understanding of the driving and resisting forces of plate tectonics: primarily slab pull and to a lesser extent ridge push as driving forces (Forsyth and Uyeda, 1975; Lithgow-Bertelloni and Richards, 1998), and mantle drag as either driving or resisting plate motion (particularly by continental keels or slabs), and the resistance on subduction interfaces, as main additional forces (Behr and Becker, 2018; Spakman *et al.*, 2018; Coltice *et al.*, 2019). An important constraint on plate reconstruction and relative plate motions since the Mesozoic is provided by marine magnetic anomalies that reveal plate motion change on various temporal scales. Reconstructions of major ocean basins usually provide one average Euler pole (plate motion data point) for stages of 3 - 10 Ma (e.g. Müller *et al.*, 2019), even though often more magnetic anomalies can be present in such stages. Such reconstructions reveal gradually changing plate motions on tens of millions of year time scales with occasional sudden cusps in plate motion between stages (Torsvik *et al.*, 2008; Doubrovine *et al.*, 2012; Müller *et al.*, 2022). Gradual plate motion changes can be explained by changes in slab pull for example due to slow age variation of subducting lithosphere (Sdrolias and Müller, 2006; Goes *et al.*, 2011), or in the lubrication of plate contacts (Behr and Becker, 2018). Cusps may correspond to changes in contributing forces through e.g., changes in slab pull due to subduction initiation or

arrest (Gürer *et al.*, 2022; Hu *et al.*, 2022), by slab detachment (Bercovici *et al.*, 2015) or resistance to subduction of large oceanic plateaus (Knesel *et al.*, 2008), the arrival of a mantle plume-head that may lubricate or push plates (van Hinsbergen *et al.*, 2011; van Hinsbergen *et al.*, 2021), or to the decrease of a plate area through breakup (e.g., Wortel and Cloetingh, 1981). Only recently, high-resolution (0.5-1 Ma) plate kinematic reconstructions of India-Africa spreading during the Eocene revealed surprisingly variable ocean spreading kinematics (DeMets and Merkouriev, 2021).

It has long been known that the spreading rate between India and Africa, and the convergence rate between India and Asia, between ~ 65 and ~ 50 Ma, was very high, close to 20 cm/a (Patriat and Achache, 1984; van Hinsbergen *et al.*, 2011). Those estimates were based on about one Euler pole every 5 Ma. White and Lister (2012) suspected that shorter-wavelength plate velocity oscillations may have occurred although being smoothed out in existing global plate tectonic reconstructions. Their suspicion was recently corroborated by the high-resolution magnetic anomaly study of (DeMets and Merkouriev, 2021), which revealed that the period of high India-Asia convergence rate contained rapid oscillations with an amplitude 10 cm/a or more at a period of 6-8 Ma (Figure 3.1). Such plate motion variations suggest that a hitherto unrecognized process plays a role that causes oscillating changes in either slab pull, or friction, or both that perhaps becomes more pronounced with higher rates of subducting plate motion.

Subducting plate motions and changes therein must be accommodated in the underlying mantle. Correlations between imaged mantle structure and the global geological record of subduction show that the remnants of detached slabs in the lower mantle sink with rates of $\sim 1 - 1.5$ cm/a, almost regardless of the rate at which they subducted at a trench (van der Meer *et al.*, 2010; Butterworth *et al.*, 2014; van der Meer *et al.*, 2018). Therefore, subducting slabs eventually decelerate from plate tectonic rates (up to 20-25 cm/a (Zahirovic *et al.*, 2015; Hu *et al.*, 2022) to average lower mantle sinking rates of <1.5 cm/a. To accommodate this requires some form of slab shortening or thickening. Subduction modelling revealed that this deceleration naturally leads to slab thickening, which could occur in the mantle transition zone through slab buckling (Ribe *et al.*, 2007; Sigloch and Mihalynuk, 2013; Goes *et al.*, 2017). Later, detailed tomographic analyses of slabs in the mantle transition zone and in the top of the lower mantle confirmed that they are systematically buckled (Wu *et al.*, 2016; Chen *et al.*, 2019). Tomography of the lower mantle below India has revealed a major slab that is widely interpreted to represent the subducted Neotethys ocean, and that also contains the lithosphere that subducted between 65
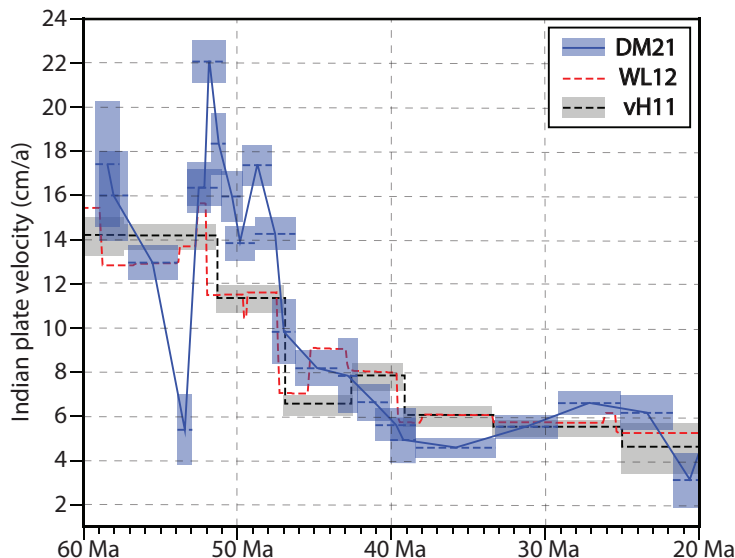
Chapter 3

Figure 3.1 Indian plate velocity relative to Eurasia from 60 Ma ago to 20 Ma ago. Shown are the reconstructed velocities of the Indian plate from DM21 (DeMets and Merkouriev, 2021), WL12 (White and Lister, 2012) and vH11 (van Hinsbergen *et al.*, 2011). Blue and grey rectangles indicate error margins in reconstructions and time interval spanned by each stage velocity.

and 50 Ma (van der Voo *et al.*, 1999; Replumaz *et al.*, 2004; Parsons *et al.*, 2021; Qayyum *et al.*, 2022). The enormous volume of this slab requires that it was drastically thickened, and while tomographic detail so far has not been able to resolve internal structure, the documentation that slabs buckle during thickening elsewhere (Wu *et al.*, 2016; Chen *et al.*, 2019) makes it feasible that this process also played a role here. Such buckling, which potentially may become more pronounced with faster subduction, makes slabs fold backward and forward, creating an oscillating slab dip and slab motion (Schellart, 2005; Lee and King, 2011; Čížková and Bina, 2013; Garel *et al.*, 2014; Holt *et al.*, 2015; Billen and Arredondo, 2018; Xue *et al.*, 2022). Here, we hypothesize that pronounced slab buckling causes the rapid, large-amplitude Eocene plate motion fluctuations of India.

To test this hypothesis, we conduct numerical experiments with decoupled, freely subducting plates that buckle in the mantle transition zone, creating periodically changing plate motions (Pokorný *et al.*, 2021). We evaluate under which conditions fluctuations such as those reported for the India plate may occur. We will discuss our results in terms of the implications for our understanding of the driving forces of plate tectonics, and how

obtaining detailed marine magnetic anomaly records may aid improving the predictive power of plate tectonic reconstructions for applications to plate boundary deformation and magmatic or mineralization processes.

3.2   Methods

3.2.1   Model set up

A set of partial differential equations in an extended Boussinesq approximation (Ita and King, 1994) (EBA) is used to describe our numerical model of subduction. These equations are solved by a finite element method implemented in the SEPRAN package (Segal and Praagman, 2005; van den Berg *et al.*, 2015). Our model domain is represented by a 2D box 10 000 km wide and 2 000 km deep (Figure 3.2). The subducting plate stretches from the ridge in the upper left corner to the trench in the middle of the upper surface. The initial temperature distribution in the subducting plate follows a half-space model followed by an adiabatic profile with a potential temperature of 1573 K beneath it.

We carried out two sets of simulations with similar matching parameters. The first set with an overriding plate that is allowed to move freely (subduction with possible rollback), while the second set features a fixed overriding plate (stationary trench – restricted rollback). Figure 3.3 illustrates time evolution of a reference model for both sets of simulations. In these reference models we assume a subducting and overriding plate age of 100 Ma at the trench and the viscosity of the crustal decoupling layer of 10^{20} Pa s.

Models of the first set have a mobile overriding plate with a ridge in the upper right corner. The rollback of trench induces the motion of the entire overriding plate towards the left, which is facilitated by the presence of a hot and low-viscosity mid-ocean ridge. The second set of models has a stagnant overriding plate with an age increasing from approximately $\sim$ 17 Ma at the right-hand side to 100 Ma (i.e., for the reference model) at the trench. Cold and thus strong overriding plates cannot move to the left because of the impermeable free slip condition on the right vertical boundary. Therefore, rollback is prohibited and the trench remains stagnant during the model run. We evaluated the effects of the age of the subducting and overriding plates (Capitanio *et al.*, 2010; Garel *et al.*, 2014) – we tested ages at the trench ranging from 50 Ma to 200 Ma.

To obtain an initial slab with sufficient negative buoyancy that would facilitate subduction, we first execute a short kinematic run to develop the slab tip to a depth of approximately 200 km. Within this kinematic prerun

a constant convergence velocity of 2.5 cm/a is prescribed on the top of the subducting plate. After 6 Ma the kinematic boundary condition is turned off and an impermeable free slip is prescribed on all boundaries.

Top and bottom model boundaries are considered isothermal with respective temperatures of 273 K and 2132 K while the vertical boundaries have zero heat flux. Thermal diffusivity is constant 10^{-6} m^{2}s^{-1} while thermal expansivity is depth dependent (Katsura *et al.*, 2009) and decreases from 3×10^{-5} K^{-1} at the surface to 1.2×10^{-5} K^{-1} at the bottom of the model domain (Hansen *et al.*, 1993).

We consider the major mantle phase transitions: the polymorphous exothermic transition of forsterite to wadsleyite at 410 km depth and the endothermic transition of ringwoodite to bridgmanite and periclase at a depth of 660 km with their associated petrological density contrasts (Table 3.1). These are incorporated through the harmonic parameterization (Čížková *et al.*, 2007) of a phase function (Christensen and Yuen, 1985). We performed a parametric study where we varied the values of Clapeyron slopes in a usually accepted range ($\gamma_{410} = 1 - 3$ MPa K^{-1}, $\gamma_{660} = -2.5 - (-1.5)$ MPa K^{-1}). All these models result in quasiperiodic buckling of the slab. The strengths of the phase transitions control slab dip angle and related rollback velocity, the ability to penetrate the lower mantle as well as slab viscosity in the transition zone. These factors than affect observed periods of the oscillations that vary between $\sim 10 - 20$ Ma. Based on this parametric study we chose the values of Clapeyron slopes of 3 MPa K^{-1} and -1.5 MPa K^{-1} for the 410 km and 660 km phase transitions. These values were chosen to

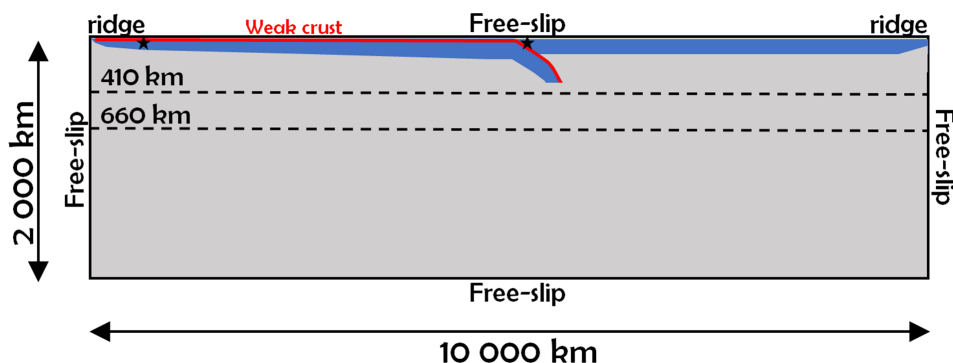**Figure 3.2** Model domain is 10 000 km wide and 2 000 km deep. Dashed lines indicate major phase transitions at 410 and 660 km depth. Red line positioned at the top of the subducting slab indicates a 10 km thick weak crustal layer, effectively separating the plates. Two black asterisks represent tracers used to track the velocity of the subducting plate and overriding plate. Free slip boundary condition is prescribed on all boundaries.

accommodate realistic average subduction velocities (Zahirovic *et al.*, 2015) with fast plate velocity oscillations (DeMets and Merkouriev, 2021) while still agreeing with in-situ X-ray diffraction experiments and thermodynamic estimates (Bina and Helffrich, 1994; Morishima *et al.*, 1994; Katsura *et al.*, 2004; Su *et al.*, 2022).

To evaluate the subducting plate velocity and trench retreat velocity in our models we use two passive particles, one initially positioned in the subcrustal lithosphere of the subducting plate (4600 km left of the trench) and the other one in the overriding plate close to the trench (Figure 3.2).

3.2.2   Rheological description

Our subduction model incorporates crustal and mantle material. A low-viscosity crustal layer facilitating mechanical decoupling of the subducting and overriding plate is initially positioned along the top of the subducting plate and within the subduction channel (Figure 3.2). Crustal material is tracked using 2 million tracers prescribed in the crust and its closest vicinity. The initial thickness of the crustal layer is 10 km.

Upper mantle material is described by a composite rheology model (van den Berg *et al.*, 1993; Ciskova *et al.*, 2002) combining dislocation creep, diffusion creep and a power-law stress limiter which effectively approximates the Peierls creep (Androvicova *et al.*, 2013). In the diffusion and dislocation creep equations (equations 3.1 and 3.2), the pressure and temperature dependence of viscosity follows Arrhenius law:

$$\eta_{diff} = A_{diff}^{-1} \exp \left(\frac{E_{diff} + pV_{diff}}{RT} \right) \tag{3.1}$$

$$\eta_{disl} = A_{disl}^{-1/n} \dot{\varepsilon}_{||}^{(1-n)/n} \exp \left(\frac{E_{disl} + pV_{disl}}{nRT} \right) \tag{3.2}$$

$$\eta_y = \sigma_y \dot{\varepsilon}_y^{-(1/\eta_y)} \dot{\varepsilon}_{||}^{(1/\eta_y)-1} \tag{3.3}$$

$$\frac{1}{\eta_{eff}} = \frac{1}{\eta_{diff}} + \frac{1}{\eta_{disl}} + \frac{1}{\eta_y} \tag{3.4}$$

Here $A_{diff/disl}$, $E_{diff/disl}$, $V_{diff/disl}$ are pre-exponential parameter, activation energy, activation volume for diffusion and dislocation creep, $\dot{\varepsilon}_{||}$ is the second invariant of the strain rate tensor and n is the power-law exponent of the dislocation creep. A power law stress limiter viscosity is parametrized through the yield stress σ_y, reference strain rate $\dot{\varepsilon}_y$ and a power-law exponent η_y, which is set to 10 in our models (equation 3.3). Assuming unique stress, individual creep mechanism viscosities are combined into the effective viscosity through equation 3.4.

Table 3.1 Model parameters. (*a*) Hirth and Kohlstedt, 2003, (*b*) Čížková *et al.*, 2012, (*c*) Bina and Helffrich, 1994 and (*d*) Steinbach and Yuen, 1995.

Parameter	Value	Units
Global model parameters		
Reference strain rate ($\dot{\epsilon}_y$)	1×10^{-15}	s^{-1}
Stress limit (σ_y)	2×10^8	Pa
Hydrostatic pressure (p)	—	Pa
Stress limit exponent (n_y)	10	—
Gas constant (R)	8.314	$JK^{-1}\ mol^{-1}$
Temperature (T)	—	K
Second invariant of strainrate ($\dot{\varepsilon}_\parallel$)	—	s^{-1}
Range of constant crustal viscosity (η_c)	$5 \times 10^{19} - 5 \times 10^{20}$	Pa s
Thermal diffusivity (κ)	10^{-6}	$m^2\ s^{-1}$
Gravitational acceleration (g)	9.8	$m^2\ s^{-2}$
Reference density (ρ_0)	3416	$kg\ m^{-3}$
Specific heat (C_p)	1250	$J\ kg^{-1}\ K^{-1}$
Surface thermal expansivity (α_0)	3×10^{-5}	K^{-1}
Upper mantle and oceanic lithosphere rheology		
Prefactor of diffusion creep[a] (A_{diff})	1×10^{-9}	$Pa^{-1}\ s^{-1}$
Prefactor of dislocation creep[a] (A_{disl})	31.5×10^{-18}	$Pa^{-n}\ s^{-1}$
Act. energy of diffusion creep[a] (E_{diff})	3.35×10^5	$J\ mol^{-1}$
Act. energy of dislocation creep[a] (E_{disl})	4.8×10^5	$J\ mol^{-1}$
Act. volume of diffusion creep[a] (V_{diff})	4.0×10^{-6}	$m^3\ mol^{-1}$
Act. volume of dislocation creep[a] (V_{disl})	11×10^{-6}	$m^3\ mol^{-1}$
Viscosity of diffusion creep (η_{diff})	—	Pa s
Viscosity of dislocation creep (η_{disl})	—	Pa s
Power-law stress limitor viscosity (η_y)	—	Pa s
Dislocation creep exponent (n)	3.5	—
Lower mantle rheology		
Prefactor of diffusion creep (A_{diff})	1.3×10^{-16}	$Pa^{-1}\ s^{-1}$
Act. energy of diffusion creep[b] (E_{diff})	2×10^5	$J\ mol^{-1}$
Act. volume of diffusion creep[b] (V_{diff})	1.1×10^{-6}	$m^3\ mol^{-1}$
Phase transition		
Clapeyron slope of 410 km [c] (γ_{410})	3×10^6	$Pa\ K^{-1}$
Clapeyron slope of 660 km [c] (γ_{660})	-1.5×10^6	$Pa\ K^{-1}$
Density contrast of 410 km [d] ($\delta_{\rho410}$)	273	$kg\ m^{-3}$
Density contrast of 660 km [d] ($\delta_{\rho660}$)	341	$kg\ m^{-3}$
Nonlinear crustal rheology		
Prefactor of dislocation creep (A_c)	2.5×10^{-17}	$Pa^{-1}\ s^{-1}$
Act. energy of dislocation creep (E_c)	1.54×10^5	$J\ mol^{-1}$
Act. volume of dislocation creep (V_c)	0	$m^3\ mol^{-1}$
dislocation creep exponent (n_c)	2.3	—
Cohesion (τ_c)	$0.25 - 1 \times 10^7$	Pa
Friction coefficient (μ_c)	$0.025 - 0.1$	—
Stress limit in the crust (σ_y^c)	—	Pa

The lower mantle deformation is assumed to be mainly through diffusion creep (Karato *et al.*, 1995), therefore we take $\eta_{eff} = \eta_{diff}$ in the lower mantle. Prefactor A_{diff} and activation parameters of lower mantle diffusion creep are based on slab sinking speed analysis (Čížková *et al.*, 2012).

The crust in our models is mostly assumed to have constant viscosity in a range of $\eta_c = 5 \times 10^{19} - 5 \times 10^{20}$ Pa s. We have also conducted several tests with the composite nonlinear rheology of the crust (Pokorný *et al.*, 2021) combining dislocation creep (Ranalli, 1995) and a Byerlee type deformation (Karato, 2008) as an approximation of the brittle failure (pseudoplastic deformation). In these models, dislocation creep viscosity follows equation 3.5 (similar to equation 3.2), but the parameters A_c, E_c, V_c and n_c differ from mantle parameters of equation 3.2 – see table 3.1.

$$\eta_{disl}^c = A_c^{-1/n_c} \dot{\varepsilon}_{\|}^{(1-n_c)/n_c} \exp\left(\frac{E_c + pV_c}{n_c RT}\right) \tag{3.5}$$

Pseudoplastic deformation limits the maximum stress in the crust to σ_y^c, where this stress limit increases with lithostatic pressure p through equation 3.6, here τ_c is the cohesion and μ is the friction coefficient. The pseudoplastic viscosity η_{pl} is then defined by equation 3.7 and the effective crustal viscosity is given by equation 3.8.

$$\sigma_y^c = \tau_c + \mu p \tag{3.6}$$

$$\eta_{pl} = \frac{\sigma_y^c}{2\dot{\varepsilon}_{\|}} \tag{3.7}$$

$$\frac{1}{\eta_{eff}^c} = \frac{1}{\eta_{disl}^c} + \frac{1}{\eta_{pl}^c} \tag{3.8}$$

3.3   Results

We conducted experiments in a 2D numerical model of subduction (Figure 3.2). The rheology of the upper and lower mantle (Čížková *et al.*, 2012; Čížková and Bina, 2013; Čížková and Bina, 2019) was chosen to accommodate typical subduction velocities (Zahirovic *et al.*, 2015) that in the upper mantle exceed the inferred lower mantle average slab sinking rates (van der Meer *et al.*, 2018). This mantle rheology leads to slab shortening and buckling in the upper-to-lower mantle transition zone (MTZ). We experimented with varying lithospheric ages to assess the effect of varying oceanic lithosphere thickness, and with varying crustal viscosities to assess the effect of average plate motion on the amplitude and period of the plate motion. We conducted one group of experiments, with a free overriding
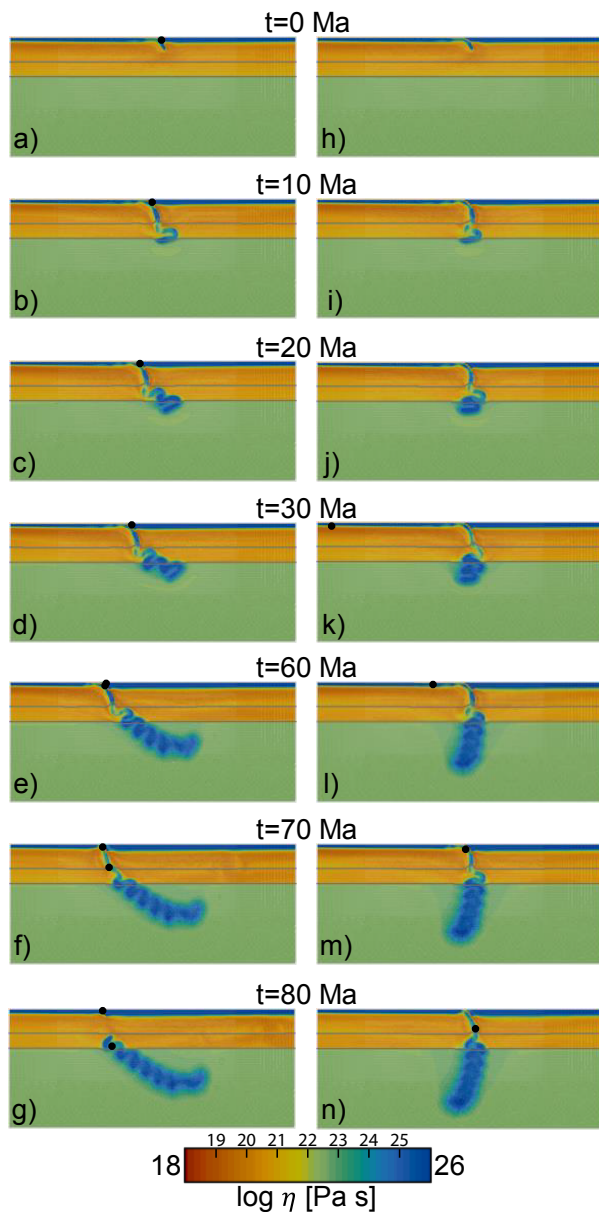
Figure 3.3 Zoomed-in viscosity snapshots (4800x2000 km) of the model for 80 Ma of model time. Grey lines indicate position of the major phase transition at 410 and 660 km depth with the values of Clapeyron slopes of 3 and -1.5 $\mathrm{MPa\,K^{-1}}$, respectively. Black dots are reference points used to calculate plate velocities. **a-g)** Reference model with free moving overriding plate resulting in trench retreat and an inclined slab in the lower mantle. **h-n)** Reference model with a stationary trench creating a vertical lower mantle slab.

plate which leads to slab rollback and results in low angle buckling with multiple buckles (partly) present in above the 660 km discontinuity, and lower net lower mantle slab sinking rates (Figure 3.3a-g). Another group of experiments implements a fixed overriding plate that suppresses the development of rollback, such that subduction occurs at a mantle-stationary trench (Figure 3.3h-n). This generates buckling into a near-vertical slab-pile (Běhounková and Čížková, 2008) that slowly sinks into the lower mantle leaving at any time only one buckle present above the 660 km discontinuity.

Slab shortening occurs through the combined resistance of the more viscous lower mantle and the endothermic phase change at the 660 km boundary, while the shallower part of the slab is continuously pulled by the exothermic phase change at 410 km (see methods). Buckling of the shortening slab is influenced by the non-linear rheology of the slab that results from the presence of a crust and lithospheric mantle layer (Pokorný et al., 2021). We assess the horizontal velocity of the subducting plate V_{SP} and upper plate V_{UP} as an effect of lithospheric thickness (corresponding to the age of lithosphere at the trench) or through weakening subduction interfaces (crustal viscosity) to evaluate causal relationships between subduction dynamics and oscillating plate motions.

3.3.1 Slab buckling in the reference models

Figure 3.3 shows two reference experiments for the model setups with and without roll-back. These have a crustal viscosity of 10^{20} Pa s and overriding and subducting plate ages at the trench of 100 Ma. In the model with a mobile overriding plate (Figure 3.3a-g), the slab undergoes a rapid, vertical descent through the upper mantle and the tip reaches the 660 km discontinuity after approximately 5 Ma model time (Supplementary Movie – panel A). The slab in the transition zone experiences down-dip compression which leads to (nonlinear) rheological weakening, causing the slab to buckle forwards (Figure 3.4a) (i.e., towards the overriding plate) over the trapped tip that started to penetrate the 660 km discontinuity. Next, the slab buckles backward (i.e. towards the downgoing plate). This leads to an episode of roll-back and short-lived V_{SP} increase until the slab is almost vertically orientated at $t = 11$ Ma (Figure 3.4b). This is followed by the initiation of a second forward buckle, folding the slab over its deeper part in the MTZ, between $t = 11$ Ma and 18 Ma (Supplementary movie – panel A), associated with rollback and a decrease of V_{SP} and increase of V_{UP} (Figures 3.4b and 3.5a). This forward buckle starts tightening at $t = 18$ Ma, inducing the next backward buckle which is followed by a rapid increase of V_{SP} up to 12 cm/a, accompanied by a decrease of V_{UP} to almost 0 cm/a
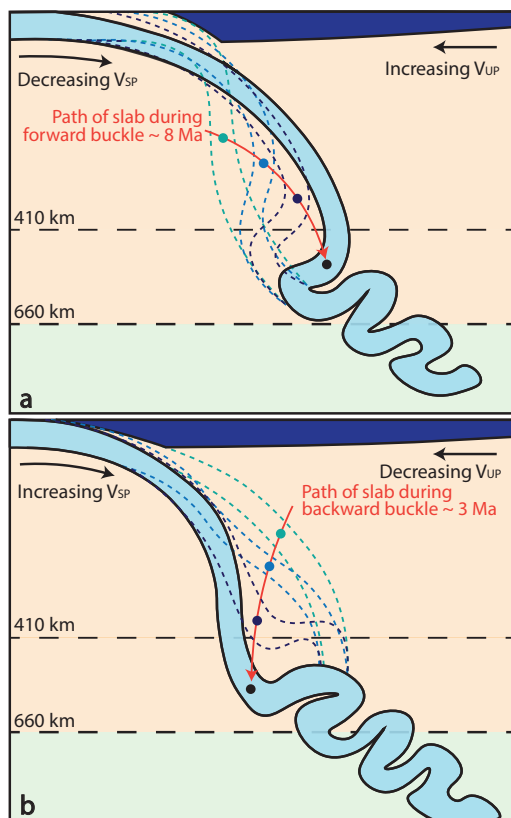
Figure 3.4 A cartoon illustrating forward (**a**) and backward (**b**) slab buckling as result of the interplay of the slab with the phase transitions and the lower mantle. During forward buckling the slab in the MTZ advances while the trench retreats, accompanied by a decreasing V_{SP} and increasing V_{UP}. The backward buckle allows the slab to sink fast in the MTZ with a rapid increase of V_{SP}, while the trench stays mantle stationary. The backward buckles form faster than forward buckles, in about 3 versus 8 Ma for our reference model.

(Figure 3.5a). At $t = 20$ Ma the next forward buckle initiated (Figure 3.3c), resulting again in an episode of rollback with decreasing V_{SP} and increasing V_{UP} (Figures 3.4a and 3.5a).

From here on, this process repeats itself quasi-periodically with new buckles forming approximately every 10 Ma (Figure 3.3c-f). This continuous subduction and rollback creates a buckled and thickened slab which slowly enters the lower mantle at an overall low-angle orientation (Figure 3.3d-g). After 70 Ma and 5000 km of subduction, the weak crust that facilitates the modelled subduction (see methods) is entirely consumed, the subducting plate is locked to the overriding plate and subduction stops. The modelled slab detaches and sinks into the lower mantle at a rate of ~ 1 cm/a, on par

with inferred and modelled lower mantle slab sinking rates (Čížková *et al.*, 2012; van der Meer *et al.*, 2018). Throughout the experiment, and after 70 Ma of modelled convergence, the overriding plate and trench moved ~ 1000 km in absolute motion, i.e., relative to the mantle, towards the subducting plate.

The model with a fixed overriding plate, which suppresses rollback (Figure 3.3h-n), shows similar characteristics. The slab is compressed down-dip and rheologically weakened in the transition zone, also resulting in the formation of a second buckle at around $t = 10$ Ma (Figure 3.3i and Supplementary Movie – Panel B). The tightening of the buckle at the base of the upper mantle coincides with an increase in plate velocity around $t = 15$ Ma (Figure 3.5b). Due to the absence of rollback, the buckled slab is oriented vertically, like previously conceptualised 'slab walls' (Sigloch and Mihalynuk, 2013). The oscillations in V_{SP} are of lower amplitude, on the order of 2 cm/a, recurring in a ~ 12 Ma period (Figure 3.5b). Absolute motion rates and oscillations therein of the subducting plate are similar to the scenario with roll-back but because the upper plate is fixed and roll-back does not add to the net convergence rate, subduction continued for ~ 90 Ma in model time, after which, the modelled slab detached and descended through the lower mantle with similar rate as in the reference model with rollback.
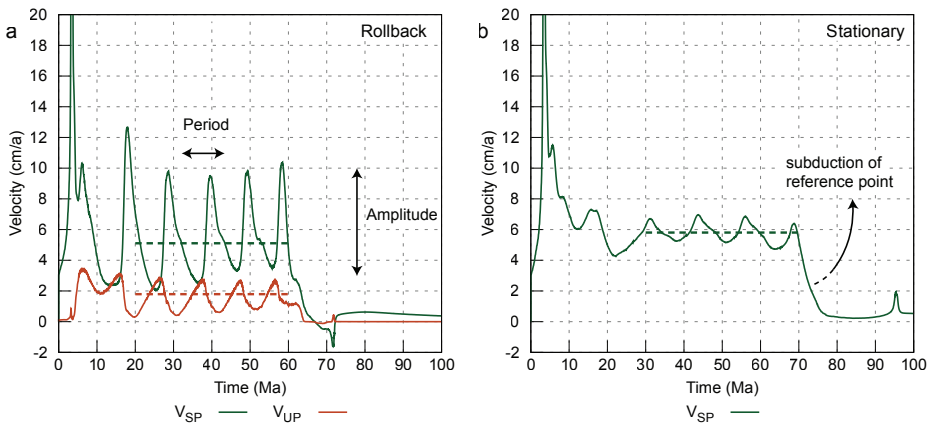
Figure 3.5 Temporal evolution of the plate motions in both reference models. **a)** Subduction velocity and overriding plate motion of the reference model with rollback, VSP oscillates between 2 and 10 cm/a and V_{UP} between 0 and 3 cm/a. The reference point subducts at t = 60 Ma and slab detachment occurs around $t = 70$ Ma. **b)** Similar as in a but for the reference model with a stationary trench, subduction of the reference point occurs at $t = 70$ Ma and slab detachment at $t = 90$ Ma. The dashed lines indicate the average velocity, which is calculated over the shown 40 Ma time-interval.

Chapter 3

75

Figure 3.6 a) Total convergence rate ($V_C = V_{SP} + V_{UP}$) of the reference model with rollback showing smaller amplitudes in the oscillations, red and green lines are the same as in Figure 3.5. **b**) Relative percentages of the total convergence rate for both the subducting plate (green; 100-50%) and overriding plate (orange; 50-0%). Grey line is the same as in **a**, and uses the y-axis of **a**.

3.3.2 Plate motion oscillations caused by buckling

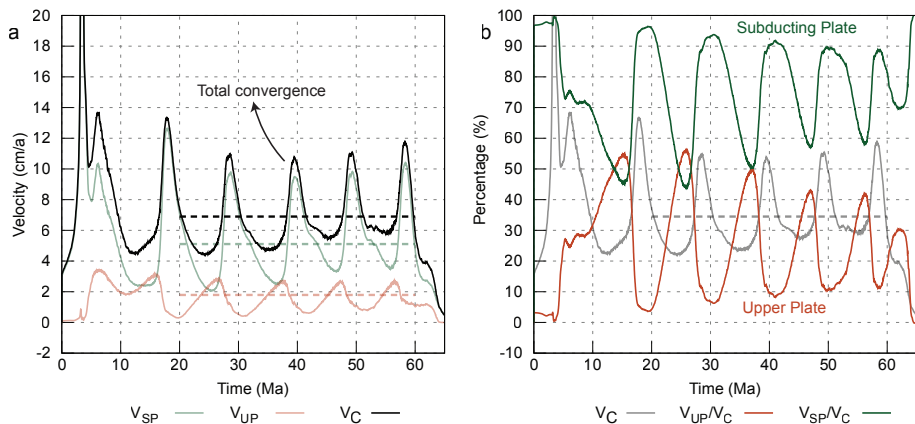The quasiperiodic buckling of the subducting plate in the MTZ causes oscillations in the subduction velocity for both types of models (Figure 3.5) and in the motion of the overriding plate in the models that allow for rollback (Figure 3.5a). Periods of fast V_{SP} coincide with tightening of a buckle and steepening of the slab and correspond with minima in the V_{UP} (Figure 3.5). We represent the periodicity of these plate motions with an amplitude and period, which we calculate in a 40 Ma time-interval of steady-state oscillations after subduction initiation and initial descend of the slab to the mantle transition zone, and before the end of the experiment (Figure 3.5). In the reference model with rollback, the subducting plate moved between 20 and 60 Ma with an average V_{SP} of 5.1 cm/a while oscillating between ~ 2 and 10 cm/a (Figure 3.5a). The average amplitude and period of the V_{SP} oscillations are 6.8 cm/a and 9.8 Ma (Figure 3.5a). Motion of the rigid, undeformable overriding plate, follows the oscillatory motion of the retreating trench. In the 20-60 Ma interval the overriding plate has an average V_{UP} of 1.8 cm/a towards the subducting plate, with oscillations between ~ 0 and 3 cm/a (Figure 3.5a). Maxima in trench motion and V_{UP} coincide with minima in V_{SP}, both occurring during formation of a new forward buckle and the associated shallowing of slab dip. During tightening of the buckle, the slab rolls back from inclined to vertical, associated with a sharp rise in V_{SP}, this change in angle is associated with a temporally near-stationary trench,

and a resulting decrease in V_{UP} towards 0. The total convergence rate (V_C) then also oscillates (Figure 3.6a), with an amplitude of 6 cm/a, about 1 cm/a smaller than the amplitude of V_{SP}. The motion of the subducting plate accounts for 50-100% of the total convergence, while the overriding plate is only responsible for 50-0% (Figure 3.6b). The highest contribution of trench motion to the convergence occurs during periods of minimal V_{SP}.

The reference model with a fixed overriding plate (Figure 3.3h-n), so with a mantle-stationary trench, also shows oscillations in V_{SP} (Figure 3.5b) caused by the buckling of the overall vertical slab in the MTZ. In the 40 Ma long time-interval (here, between 30-70 Ma) quasiperiodic buckling occurs with an average V_{SP} of 5.7 cm/a (Figure 3.5b), faster than the model with rollback. The oscillations in V_{SP} occur with a period of 12.7 Ma and an amplitude of 1.6 cm/a. This amplitude is more than 4 times lower than the amplitude of oscillations in the model with rollback. The freedom to roll back allows for much larger variation in slab dips, and results in higher amplitudes of plate motion oscillations, as well as a higher net convergence rate.

3.3.3 How subduction velocity controls plate motion oscillations

When lithosphere subducts at a rate of 5-6 cm/a as in our reference models, it can reach the 660-discontinuity 13-11 Ma after passing the trench. Higher subduction rates decrease that time interval and increase the amount of subducted slab in the MTZ, creating an accommodation space problem. We performed numerical experiments to evaluate the effect of subduction speed on the formation of buckles and on oscillations in V_{SP}. We modified the subduction rate in our experiments in two ways. On the one hand, we performed experiments with constant crustal viscosity while varying the age of the overriding and subducting plates. Overriding plate age determines the length of the subduction interface, with larger interfaces giving more resistance against subduction, decreasing subduction velocity. Subducting plate age determines the negative buoyancy, with higher subduction velocities for older plates (Capitanio *et al.*, 2011). On the other hand, we performed experiments with constant lithosphere ages (100 Ma) while adopting a constant or a power-law crustal viscosity, with lower viscosity yielding higher VSP (e.g., Behr *et al.*, 2022; see methods).

In our numerical experiments with varying plate age, the amplitude and period of the oscillations in plate velocity depend on the average subduction velocity (Figures 3.7, 3.8a-f). Models with a younger overriding plate and therefore a shorter subduction interface, have higher average subduction ve-
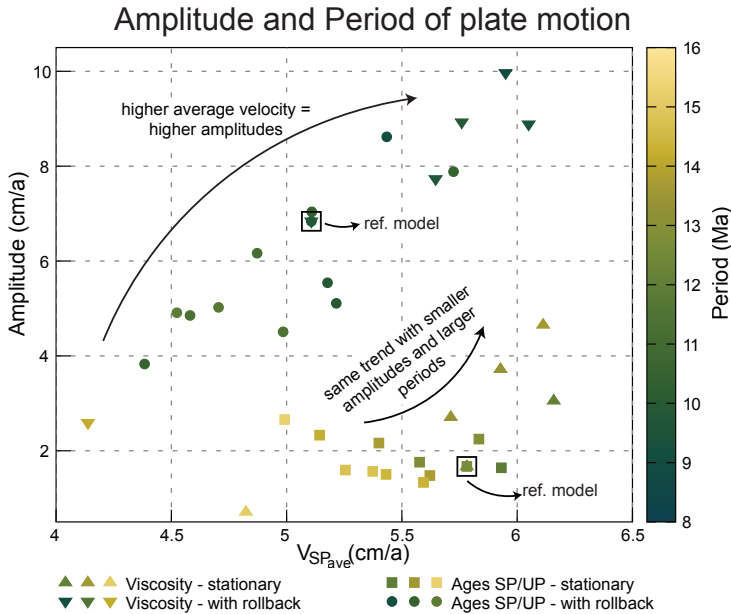
Figure 3.7 Overview of all models showing the relation the amplitude and period (colour) of VSP oscillations have with the average V_{SP}. The four types of models shown are with a varying crustal viscosity and rollback (triangles) or a stationary trench (upside-down triangles), and models with changing SP and UP ages with rollback (circles) or a stationary trench (squares). For values of the crustal viscosity and ages of plates see figure 3.8.

locities within the 40 Ma long time-period with steady-state, quasi-periodic buckling (Figures 3.8a,b). These velocities correlate directly to larger amplitudes (2-9 cm/a) in oscillations in the cases with rollback (Figure 3.8e). The cases with a stationary trench show that the amplitude of V_{SP} oscillations is predominantly determined by subducting plate age while the effect of the overriding plate age is limited. V_{SP} amplitudes vary between 1-3 cm/a (Figure 3.8f). Hence, faster-subducting plates have higher velocity amplitudes and lower periods of oscillation, and analogous to our reference models, this trend is most profound in models that allow rollback, in which the amplitudes are 2-3 times larger than in models with a mantle-stationary trench (Figure 3.7).

The models with a varying constant crustal viscosity show the same trend: higher average V_{SP}'s leads to larger velocity oscillation amplitudes (Figures 3.8c,d) and smaller periods (Figures 8 g,h). Models with a power law crustal viscosity have smaller variations in average V_{SP} between them than those with a constant viscosity and consequently also smaller variations

in oscillation amplitudes, albeit with higher absolute amplitudes (Figures 3.8c,d). This is the result of feedback mechanisms between subducting plate velocity and the power law crustal viscosity (Pokorný *et al.*, 2021), which also keeps the period of V_{SP} oscillations constant (Figures 3.8g,h).

3.4   Discussion

Slabs that subduct with plate motions exceeding the average lower mantle sinking rate of $1 - 1.5$ cm/a (van der Meer *et al.*, 2018) inevitably require that slabs shorten and thicken. Interpretations of geophysical observations and subduction models (cited above), including our own, show that this occurs through buckling of the slab in the MTZ (Figure 3.3). During slab buckling, the slab dip in the top ~ 300 km alternates between steep (vertical or overturned) and inclined, and our results illustrate that this induces alternating phases of slab rollback and stagnation (or advance), as well as motion of the trench and upper plate (Figure 3.5a). Our results reveal that these alternating phases of forward and backward buckling induce variations in subduction rate and subducting plate motion.

High subduction rates occur in our experiments when the slab buckles backward, towards the downgoing plate and adjacent to a previous slab fold. For backward buckling, the accommodation space in the MTZ in which the buckling slab can sink is available as opposed to forward buckling, in which case the lower part of the MTZ is still occupied by previously buckled slab (Figure 3.4a). As the 410 km phase transition enhances the negative buoyancy of slabs and thus enhances slab pull (Čížková and Bina, 2013) the accommodation in the MTZ for backward buckling allows the slab to force a short (in our reference model < 3 Ma) pulse of high V_{SP}, and roll-back. During roll-back, the slab steepens to a vertical orientation accompanied by limited motion of the trench (Figure 3.4b), or even trench advance if the upper plate rheology would allow it. Once the slab overturns the next forward buckle initiates, during which time MTZ accommodation space decreases. A forward buckle is associated with trench retreat and slab advance in the MTZ, seemingly rotating over a pivot point in the upper mantle (Figure 3.4a). As a result, V_{SP} decreases during a forward buckling slab while V_{UP} increases. As the slab flattens during this forward buckle it creates accommodation space for the next backward buckle and associated acceleration (Figure 3.4b).

V_{SP} variations in models with a forced stationary trench are smaller because the slab has less variation in the amount of accommodation space in the MTZ. Trench-stationary subduction causes the slab buckling in a vertical column (Figures 3.3i-n). Basically, the rate and amplitude of plate
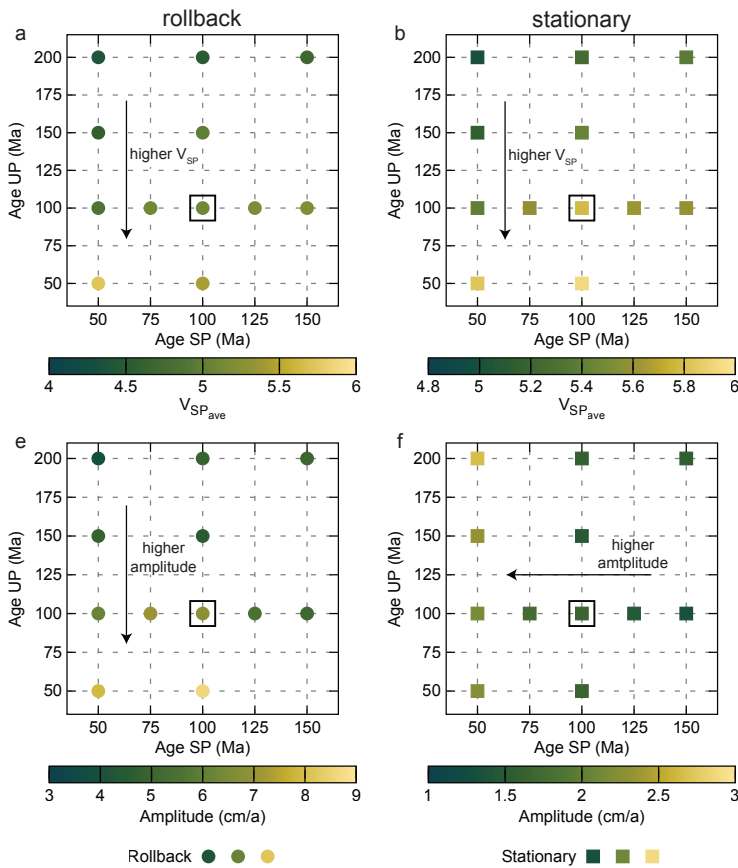
Figure 3.8 V_{SP} as function of SP and OP ages for models with a moving trench (**a**) and a stationary trench (**b**). Amplitude of the oscillating V_{SP} as function of the average V_{SP} for crustal viscosities: $5e19$, $1e20$, $5e20$ (closed triangles) and three power law crustal viscosities (open triangles) in models with a moving trench (**c**) and a stationary trench (**d**). Amplitude of the oscillating V_{SP} as function of SP and OP plate ages for models with a moving trench (**e**) and a stationary trench (**f**). Period of the oscillating V_{SP} as function of the average V_{SP} for a varying crustal viscosity in models with a moving trench (**g**) and a stationary trench (**h**). The figure is continued on the next page.

motion oscillation primarily depends on the average V_{SP}: the higher, the bigger the space accommodation problem for slab folds in the MTZ. Our experiments with a moving trench and an average V_{SP} of 6 cm/a, i.e., the global average plate velocity (van der Meer *et al.*, 2014), reveal rapid oscillations (< 10 Ma periods) with large V_{SP} fluctuations (3 to 13 cm/a) (Figure 3.6).
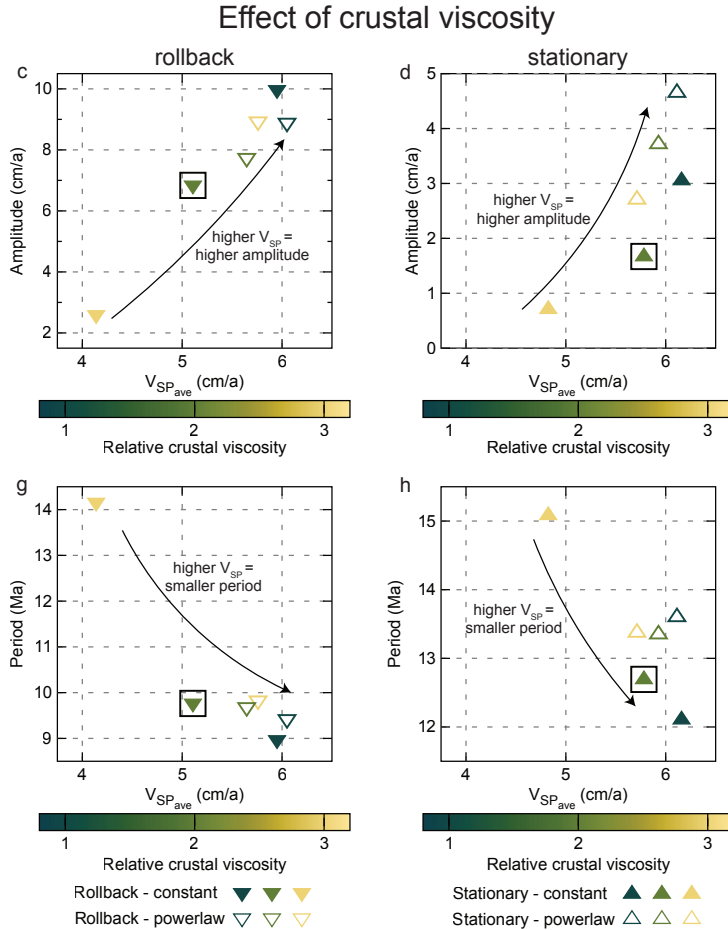
Figure 3.8 continued

The rapid subducting plate motion oscillations that we find in our experiments have similar periods to those recently observed in the high-resolution (0.5-1 Ma) reconstruction of marine magnetic anomalies of the Indian Ocean (DeMets and Merkouriev, 2021). Previous plate reconstructions using stage rotations based on larger stage intervals of 5-10 Ma (Figure 3.2) (van Hinsbergen *et al.*, 2011; Müller *et al.*, 2019) smoothed out such rapid plate motion changes (White and Lister, 2012; Espinoza and Iaffaldano, 2023). We illustrate this by sampling V_{SP} in our reference experiment with a mobile upper plate: when we sample on a 1-2 Ma resolution, similar to (DeMets and Merkouriev, 2021) we resolve rapid (< 5 Ma) oscillations in plate motion caused by slab buckling (Figure 3.9a). However, sampling our V_{SP} curves

Chapter 3

at larger, typically used intervals of 5 or 10 Ma generates the smooth plate motion history that is widely inferred from plate reconstructions (Figures 3.9b,c).

The average V_{SP} as well as the amplitudes of the plate motion oscillations for the case of India are higher than in our experiments. These differences are likely at least in part explained by the simplicity of our model: the absolute plate motion rate of India may have been much higher than we obtained in our experiments because the Indian plate may have been lubricated at the base by a mantle plume (Kumar *et al.*, 2007; van Hinsbergen *et al.*, 2011), or the subduction interface may have been heavily lubricated by sediments (Behr and Becker, 2018). The buckling behaviour may have differed because Indian subduction rates were not uniform along-strike, but increased eastward (van Hinsbergen *et al.*, 2011) and the lithosphere in the MTZ during the 55-50 Ma ago interval during which the oscillations were reconstructed may have been of continental origin (van Hinsbergen *et al.*, 2019). This could have influenced the effects of the MTZ on slab pull, the rate of slab transfer into the lower mantle, and the amount of accommodation space in the MTZ, which would all influence the oscillation V_{SP} amplitude and period in our experiments.

An additional difference with our simple experiments is that subduction of the Indian plate occurred at a trench that was not retreating, as in our experiments, but instead slowly moving northwards, i.e. advancing (van Hinsbergen *et al.*, 2019). In our experiments, subduction at a mantle-stationary trench occurs with lower amplitude oscillations than those reconstructed by (DeMets and Merkouriev, 2021). However, the Indian slab may have advanced below the upper plate and retreated without significantly affecting trench motion as in our experiments. Slab buckling combined with trench advance could create an opposite regime as in our experiments, with acceleration during forward buckles and vice versa. Trench motion can even alternate between retreat and advance (Stegman *et al.*, 2010). This could explain the ~ 1000 km wide north to south tomographic anomaly widely interpreted as the Indian slab (Qayyum *et al.*, 2022). We foresee that these processes may produce variations in MTZ accommodation space even when the trench is nearly stationary. Modelling such additional complexities is beyond the scope of our investigation: with the even higher subduction rates for India than we reproduced in our experiments, the space problem in the MTZ must have been even larger than in our experiments, and we therefore consider buckling a plausible candidate to explain the reconstructed oscillations.
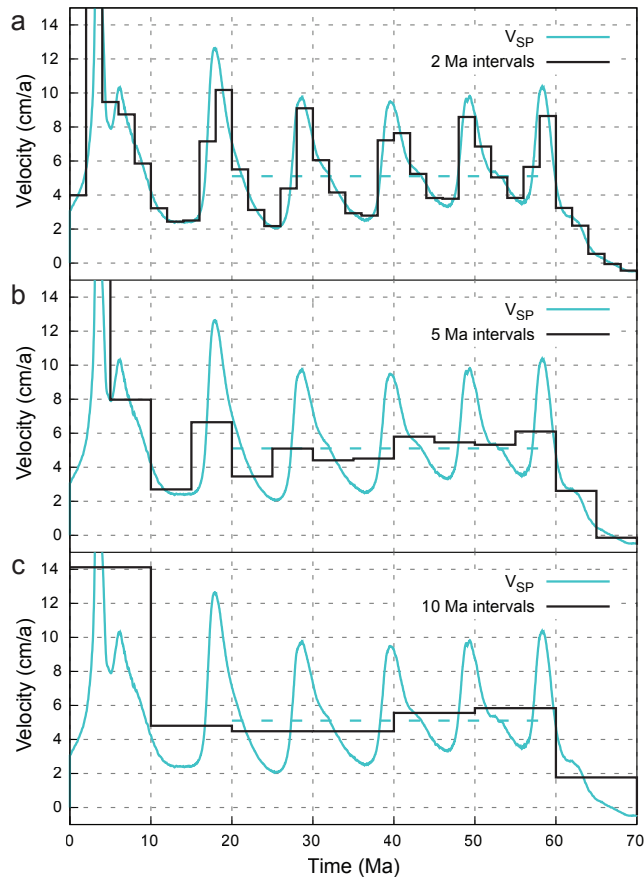
Figure 3.9 Horizontal subducting plate motion for the reference model with rollback and stage velocities if sampled at 2, 5 or 10 Ma intervals.

In our slab-pull-driven subduction models with a freely moving upper plate we also observe oscillating motion of the trench and upper plate (Royden and Husson, 2006). In our simple experiments, the rigid upper plate is not able to deform, and it thus moves along with the trench where naturally this would lead to changes in stress state, reflected by episodic back-arc spreading (Ishii and Wallis, 2022), extensional or contractional upper plate deformation (Capitanio *et al.*, 2010; Lee and King, 2011; Billen and Arredondo, 2018; Cerpa *et al.*, 2018; Boutoux *et al.*, 2021; Dasgupta *et al.*, 2021; van Hinsbergen and Schouten, 2021; Pons *et al.*, 2022) and even changes in topography (Briaud *et al.*, 2020). Such variations may be of interest to the understanding of fluid and magmatic processes affecting the upper plate. For instance, episodic magmatic ponding alternating with mi-

Chapter 3

83

gration and flare ups (Chapman *et al.*, 2021), and episodic mineralization (Chelle-Michou *et al.*, 2015) and associated pulses in the formation of ore deposits (Wilson *et al.*, 2020) may be the result of such stress state oscillations. Therefore, for subduction zones where slab buckling leads to oscillating trench motion and upper plate deformation, enhanced resolution in marine magnetic anomalies and accompanying reconstructions could lead to a better predictive power in the timing of these magmatic and ore-genesis related upper plate processes. In the Andes, alternations on a timescale of 10 Ma between shortening and trench retreat were recently postulated to result from slab buckling (Pons *et al.*, 2022). For Tibet, the only high-resolution deformation records in the relevant time interval of 60-50 Ma are from the Qiangtang terrane of northern Tibet, far from the trench (Li *et al.*, 2020a; Li *et al.*, 2020b), which on a first order appear to record shortening pulses that coincide with the oscillations (DeMets and Merkouriev, 2021). More high-resolution work, for instance in the Xigaze forearc basin, could reveal whether the upper plate may also have recorded short periods of extension.

Would all subducting plates then show these oscillating plate motions? Higher-resolution tectonic reconstructions could provide the answer, but we see several reasons why not all ridges that border subducting plates may record such oscillations similarly. The process of buckling at long subduction zones might not occur synchronously along the entire trench. Such a process may explain the oscillating azimuth of India-Asia convergence during the oscillations documented (DeMets and Merkouriev, 2021). In addition, subduction rate may vary gradually along-strike of a trench (e.g., the west Pacific subduction zones from New Zealand to Kamchatka), and rapidly across triple junctions (e.g., van de Lagemaat *et al.*, 2018; Vaes *et al.*, 2019). Plates like the modern Pacific plate would be less susceptible to the effect of slab buckling in the MTZ, even if the oscillations in a 2D system likely occur. We foresee that oscillations in plate motion are best visible for plates where subduction zones are oriented sub-parallel to spreading ridges and sub-perpendicular to the plate motion direction. Possible candidates for the Cenozoic besides the Indian plate are the Nazca plate (Pons *et al.*, 2022), the Juan de Fuca plate, the Cocos plate, or the Aluk plate (van de Lagemaat *et al.*, 2023) and for earlier times perhaps the Farallon or Kula plates. We consider these targets for high-resolution magnetic anomaly reconstruction to further test the possibilities of slab buckling and the opportunities it may apply to understand mantle and lithosphere dynamics and magmatic and economic geology.

Finally, our models show that the rapid oscillations shown by (DeMets and Merkouriev (2021)) may well be explained by buckling of the subducting slab that results from the accommodation space problem caused by the much lower sinking rates of slabs in the lower mantle. This implies that plate motions that exceed lower mantle slab sinking rates, so larger than 1-1.5 cm/a (van der Meer *et al.*, 2010; Butterworth *et al.*, 2014; van der Meer *et al.*, 2018), are resisted from the transition zone downwards. In other words, typical plate motions must be primarily driven in the top few hundred kilometers of the mantle. The 410 km phase transition still enhances slab pull, but at the 660 discontinuity the slab encounters resistance and thickens. In addition, the top 100 km of the Earth also resists plate motion due to friction on the subduction interface or drag resistance from the underlying mantle, therefore plate tectonics must primarily be driven between depths of $\sim$ 100 and 500 km, or only 6-7% of the Earths radius. This is a remarkably small niche that on Earth apparently has the right conditions for plate tectonics. We foresee that understanding the dynamics of this narrow zone throughout Earth's history holds the key to understand the uniqueness of our planet to start and sustain plate tectonics.

Chapter 3

4

Slab pull driving absolute motion of adjacent non-subducting plates through viscous coupling at mid-oceanic ridges

Erik van der Wiel
Cedric Thieulot
Alissa J. Kotowski
Wim Spakman
Douwe J.J. van Hinsbergen

Abstract

The motion of tectonic plates is dominantly driven by slab pull, yet plates without slabs attached are not mantle stationary and exhibit absolute plate motion. Typically, for continental plates with keels this may be explained by mantle drag induced by mantle flow or pushing plume pulses. However, oceanic plates do not have keels and those without slabs attached are surrounded by mid-oceanic ridges and transform faults, while continuously growing and moving. The Pacific Plate is a key example highlighting the conundrum since it moved with absolute plate motions of up to 9 cm/a in the Late Cretaceous, without actively subducting. We propose that the viscous coupling of oceanic plates at and below mid-oceanic ridges may transfer slab pull from neighboring plates over spreading ridges, thereby pulling along the conjugate plate. The Pacific Plate motion may then be caused by the fast-moving, subducting Izanagi Plate, which bounded the Pacific Plate in the north and subducted northeastwards underneath Eurasia. Furthermore, changes in slab pull from, e.g., cessation of subduction, may then efficiently propagate to neighboring plates through viscous coupling across spreading centers. Such across-ridge plate coupling may offer a mechanism to rapidly propagate changes in plate motion in global plate reorganizations.

4.1 Introduction

The motions of subducting tectonic plates is the result of two, possibly three driving forces: slab pull, ridge push, and mantle drag (Forsyth and Uyeda, 1975). Slab pull is caused by the negative buoyancy of aging oceanic lithosphere that consequently sinks into the mantle at subduction zones and pulls subducting plates towards trenches. Ridge push is caused by the gravitational gradient from high ridges to deep trenches but constitutes only a minor force. Decades of modelling has shown that slab pull is the prime driving force of plate tectonics and is thought to be responsible for $>$ 95% of the force (Lithgow-Bertelloni and Richards, 1998). Mantle drag is caused by relative plate-mantle motion and may be a resisting force if plates move faster than the underlying upper mantle and a driving force if vice versa, mainly affecting plates with continental keels (Coltice *et al.*, 2019; van Hinsbergen *et al.*, 2021). Short-lived mantle drag may be caused by e.g. plume heads spreading below plates (Conrad and Lithgow-Bertelloni, 2006; van Hinsbergen *et al.*, 2011) and long-lived mantle drag may relate to whole mantle convection invoked by slab suction (Conrad and Lithgow-

Bertelloni, 2004; Becker and Faccenna, 2011; Höink *et al.*, 2011; Faccenna *et al.*, 2021). Such long-term whole mantle convection is likely not as fast as average plate motions as it is caused by sinking slabs in the lower mantle with magnitudes of $\sim 1 - 1.5$ cm/a (van der Meer *et al.*, 2018) although it may contribute to absolute plate motions (Schellart, 2010). Plates that are surrounded by ridges do not directly experience slab pull, and ridge push cannot drive its absolute plate motion as the push from opposite ridges would point toward the center of the plate and their difference would only be small. If only mantle drag would act on such plates, they would be expected to move very slowly, particularly when such plates are entirely oceanic. Surprisingly, however, plate tectonic reconstructions reveal that non-subducting plates may exhibit absolute plate velocities of up to 10 cm/a.

Non-subducting plates may form at triple junctions or at existing ridges (Neves *et al.*, 2003; Boschman and Hinsbergen, 2016; Choi *et al.*, 2021) and are surrounded by mid-oceanic ridges and transforms from two or more other plates. Current examples are small plates that exist between the major Pacific and Nazca plates, including the active Juan Fernández and Easter microplates and the fossil Bauer microplate (Searle *et al.*, 1993; Eakins and Lonsdale, 2003) that have an eastward absolute plate motion trailing the faster-moving Nazca Plate. However, the most prominent example is the Pacific plate that experienced fast absolute plate motions for periods of tens of Ma despite lacking an active subducting zone, as we will argue in the following.

The Pacific Plate is presently subducting at trenches from the Aleutians to New Zealand. These formed in the last $\sim 55 - 50$ Ma following the subduction of a mid-oceanic ridge (MOR) below Japan as well as a series of tectonic reorganizations (Seton *et al.*, 2015; Vaes *et al.*, 2019; Wu and Wu, 2019; van de Lagemaat and Hinsbergen, 2023). This initiation of Pacific Plate subduction and westward slab pull is logically considered to have caused a WNW-ward absolute plate motion of the Pacific Plate from ~ 50 Ma onward that is prominent in Eocene and younger hotspot tracks on the Pacific sea floor (Faccenna *et al.*, 2012; Torsvik *et al.*, 2019). Between ~ 85 Ma and 55-50 Ma, however, the Pacific Plate was bounded in the west by a transform fault system from plates of the Neotethyan region (van de Lagemaat and Hinsbergen, 2023), and to the north, east and south by spreading ridges (Figure 4.1a) (Engebretson *et al.*, 1985; Wright *et al.*, 2016; Vaes *et al.*, 2019; van de Lagemaat *et al.*, 2023). Nonetheless, in this time period the Pacific Plate reached NNW-ward absolute plate motions as high as 9 cm/a as constrained by plate tectonic reconstructions (Figure
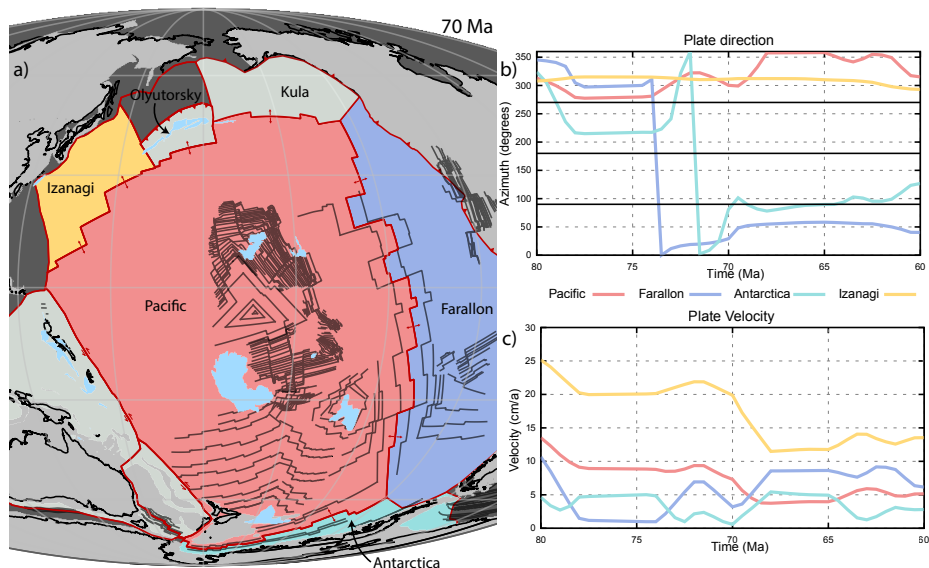
Figure 4.1 a) Plate reconstruction of the Pacific Ocean at 70 Ma after (van de Lagemaat and Hinsbergen, 2023). Plate motion azimuth (**b**) and velocity (**c**) of the Pacific, Izanagi, Antarctic and Farallon plates in the moving hotspot frame of (Doubrovine *et al.*, 2012).

4.1b,c) (Doubrovine *et al.*, 2012). Kinematic reconstructions suggest that the Pacific plate may have undergone westward subduction between ~ 110 and 85 Ma in the junction region with the Tethys region (van de Lagemaat and Hinsbergen, 2023), during which time the plate had a westward absolute plate motion direction of 5 cm/a (Torsvik *et al.*, 2019), but also before 110 Ma, when the plate was bordered by three ridges from the major Izanagi, Farallon, and Phoenix Plates (Engebretson *et al.*, 1985), the plate experienced southwest to northwestward absolute motions of 5 cm/a or more (Torsvik *et al.*, 2019).

If slab pull plays no role in driving the Pacific plate at times it was not subducting, its fast motion would require an unrealistically fast mantle drag (Clennett *et al.*, 2023). Furthermore, the Pacific Plate moved in the direction of the plates that were spreading away the fastest: predominantly the Izanagi plate (Figure 4.1a). During the peak absolute motion rates of 9 cm/a around 80 Ma ago, the Pacific Plate followed in the direction of the Izanagi Plate. This plate likely moved at very high absolute plate motions in this time interval. These are not known in detail because the plate itself, as well as the conjugate crust of the Pacific Plate younger than ~ 100 Ma, has been lost to subduction. However, assuming constant spreading rates

between 100 Ma and the arrival of the Izanagi-Pacific spreading ridge at the Japan trench around 50 Ma suggests that the Izanagi Plate moved at rates exceeding 12 cm/a, and perhaps up to cm/a to the north(northwest) (Figure 4.1b,c) (Wu *et al.*, 2016; Wu *et al.*, 2022). The Pacific Plate was at those times also spreading away from Farallon Plate to the west/northwest and the Phoenix Plate (or remnants thereof) moving to the south (Wright *et al.*, 2016; van de Lagemaat *et al.*, 2023), but these plates had slower absolute motion rates of roughly 5 cm/a (Figure 4.1c). Based on these inferences, we therefore hypothesize that the Pacific Plate was coupled across its bounding ridges to its neighboring plates such that it trailed the fastest moving one.

Typically, mid-oceanic ridges are conceptually considered to possess no strength and their only contribution to absolute plate motion stems from their relatively high topography (Forsyth and Uyeda, 1975). However, the upwelling mantle between plates consists of viscous rock and variably connected melt percolation channels, which consequently possesses finite mechanical strength. Here, we aim to assess whether some form of viscous coupling of plates 'seperated' by spreading ridges effectively allows the propagation of the intra-plate stress caused by slab pull across spreading ridges. To this end, we use a numerical modeling setup of plate and upper mantle rheology and evaluate whether a plate bounded by ridges may develop an absolute plate motion when the two neighbouring plates each have different absolute plate motions. We also performed numerical experiments to evaluate under which conditions the central plate may develop high absolute plate motion rates of up to 9 cm/a as reconstructed for the Pacific plate between 80 and 70 Ma ago (Figure 4.1c). We discuss our results in context of the global drivers of plate motions, intraplate stress, and enigmatic global plate reorganizations.

4.2   Methods

We performed numerical experiments in a 3D Cartesian box geometry with the geodynamic finite element code ASPECT version 2.5.0 (Kronbichler *et al.*, 2012; Gassmöller *et al.*, 2018; Heister *et al.*, 2017). Assuming the Boussinesq assumptions involving buoyancy-driven incompressible flow, we solves the conservation of mass (4.1), momentum (4.2) and energy (4.3) equations. Internal heating processes are neglected.

$$\nabla \cdot u = 0 \tag{4.1}$$

$$\nabla \cdot \sigma + \rho g = 0 \tag{4.2}$$

$$\rho C_p \left(\frac{\partial T}{\partial t} + u \cdot \nabla T \right) - \nabla \cdot (k \nabla T) = 0 \tag{4.3}$$

Our model consists of a 6000 km by 2000 km wide box that is 3000 km deep (Figure 4.2a). The compositional distribution and the initial temperature for both the oceanic lithosphere (plate model) and the mantle (Figure 4.2b) are implemented through the 'Geodynamic Worldbuilder' tool (Fraters *et al.*, 2019). Flow in the models follows a viscous-plastic rheology that encompasses dislocation and diffusion creep (Equation 4.4) and the Drucker-Prager yield criterion to limit viscous stresses (Glerum *et al.*, 2018). The effective viscosity is then a function of the effective deviatoric strain rate $\dot{\varepsilon}$, pressure p and temperature T as well as the material properties defined in tables 4.1 & 4.2:

$$\eta^{cr} = \frac{1}{2} A^{-\frac{1}{n}} \dot{\varepsilon}^{\frac{1-n}{n}} exp \left(\frac{E + pV}{nRT} \right) \tag{4.4}$$

where A is the pre-factor, n the stress exponent for dislocation creep, E the activation energy, V the activation volume and R the gas constant. The grain-size in diffusion creep is assumed constant and therefore incorporated in the pre-factor A.

The flow law parameters (Equation 4.4) are constant in the upper mantle and mantle transition zone through all experiments and based on those in Ulvrova *et al.* (2019) and Chapter 1 (Figure 4.2c). The oceanic lithosphere is modelled as a rigid plate with a constant viscosity equal to the maximum cut-off viscosity (Table 4.1). We found that the influence of the lower mantle is limited in this set-up and we therefore impose a constant viscosity for the lower mantle (Figure 4.2c), resembling a depth-averaged value of commonly used viscosity profiles (Table 4.1) (Steinberger and Calderwood, 2006).

Phase changes are present at 660, 410 and 100 km depths to account
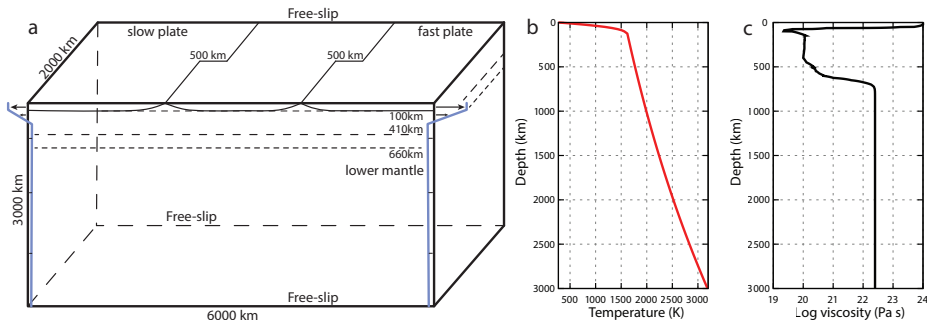

Figure 4.2 a) Cartoon of the model set up showing the extent of the domain and the initial location of the mid-oceanic ridges and transform faults. The blue lines represent the boundary velocity profile (not to scale) that is imposed on the entire left and right sides. **b**) Initial temperature profile and **c**) initial viscosity profile obtained away from a ridge.

Table 4.1 Model paramaters

Global parameters

Surface temperature K	273
Bottom temperature K	3200
Mantle thickness km	3000
Thermal expansivity K^{-1}	3×10^{-5}
Thermal diffusivity m^{2}s^{-1}	1×10^{-6}
Heat capacity Jkg^{-1}K^{-1}	1250
Radiogenic heating rate Wkg^{-1}	0×10^{-12}
Minimum viscosity cut-off Pa s	1×10^{18}
Maximum viscosity cut-off Pa s	1×10^{24}

	Oceanic lithosphere	*Upper Mantle*	*Mantle transition zone*	*Lower Mantle*
Reference density kgm^{-3}	3300	3300	3500	3900

Viscosity parameters

	MOR mantle	*Upper Mantle*	*Mantle transition zone*
Cohesions (C) MPa	20		
Angles of internal friction degrees	20		
Dislocation creep			
Prefactors (A) Pa^{-n}s^{-1}	*See table 4.2*	6.51×10^{-16}	8.51×10^{-17}
Stress exponents (n)	*See table 4.2*	3	3
Activation energies (E) Jmol^{-1}	500×10^3	500×10^3	500×10^3
Activation volumes (V) m^{3}mol^{-1}	1.2×10^{-5}	1.2×10^{-5}	2.5×10^{-5}
Diffusion creep			
Prefactors (A) Pa^{-1}s^{-1}	6.00×10^{-17}	6.00×10^{-17}	9.00×10^{-17}
Activation energies (E) Jmol^{-1}	150×10^3	150×10^3	155×10^3
Activation volumes (V) m^{3}mol^{-1}	6.34×10^{-7}	6.34×10^{-7}	14.34×10^{-7}
	Oceanic lithosphere		*Lower Mantle*
Constant viscosity Pa s	1×10^{24}		2.5×10^{22}

Phase transitions (*between*)

	100 km (crust-MOR)	*100 km (MOR-UM)*	*410 km (UP-MTZ)*	*660 km (MTZ-LM)*
Reference temperatures K	1200	1200	1600	1800
Clapeyron slopes MPaK^{-1}	-3	0	2	-2.5

for the layering in the Earth: from bottom to top the lower mantle, mantle transition zone, upper mantle, and oceanic lithosphere. The phase change temperatures, reference densities, Clapeyron slopes and the respective viscous parameters are stated in Table 4.1. Clapeyron slopes are used to heighten or lower the depth of each phase change according to the temperature at each depth (Table 4.1). In order to obtain a mantle wedge below a spreading ridge, which has its own viscous parameters in the models, we implement another phase change between the oceanic lithosphere and the upper mantle. This triangular shaped area (Figure 4.2a) is bounded at the top by the 1200 K isotherm of the oceanic lithosphere and reaches a maximum of 100 km depth. The 100 km boundary is similar to the maximum thickness of the oceanic lithosphere in our model, slightly shallower than its maximum depth (Condie, 2021).

4.2.1   Boundary conditions

Our model aims to evaluate whether and, if so, under what conditions viscous coupling at ridges may cause absolute plate motion of a non-subducting plate at velocities as high as 9 cm/a as reconstructed for the Pacific Plate at around 80 Ma, as discussed in the introduction. We simplified the setup to a three-plate system with only oceanic lithosphere, separated by two spreading ridges. We offset both ridges by 500km long transform faults to include a contribution of transform fault friction that may affect plate coupling. The top, bottom, front, and back faces of the domain are free-slip boundaries. Because we focus on a time in which absolute Pacific Plate motion was northward, we impose on the left- and right-hand sides boundary conditions that correspond to the reconstructed ranges of absolute plate motion of the Izanagi and Phoenix plates, respectively. We take a westwards view on the system, such that the right-hand plate has the highest absolute motions corresponding to the Izanagi Plate, post- and pre-70 Ma (Figure 4.1c). In model 1, which we use as a reference model, we used an imposed boundary velocity of 12 cm/a on the right-hand side, while a second set of models have a set velocity of 20 cm/a. The other bounding oceanic plate on the left-hand side moves in an opposite direction: -4 cm/a in both sets of experiments, corresponding to the absolute motions reconstructed for the daughters of the Phoenix Plate (van de Lagemaat *et al.*, 2023). The outgoing boundary velocities decrease linearly from 100km depth to a small inflow (about 7% of the imposed lithospheric outflow at each boundary) at 300km depth which is continuously imposed to the bottom of the domain (Figure 4.2a). This creates a net zero inflow over the entire boundary. After 10 Ma of modelled spreading, we compare the absolute velocity of the freely

moving central plate, corresponding to the Pacific Plate, with those from reconstructions using a moving hotspot reference frame (Doubrovine *et al.*, 2012) through a plate circuit through Antarctica summarized in (van de Lagemaat *et al.*, 2023).

4.2.2 Ridge rheology

To test the effect of viscous coupling across the mid-oceanic ridges we will vary the viscous parameters in the triangular shaped mantle below the ridges, below the oceanic crust and above 100 km of depth. This area uses the same formulation as the rest of the upper mantle, based on the diffusion and dislocation creep flow laws (Equation 4.4). In a first series of experiments, we check the result of the different boundary conditions, both ridges have a similar rheology. We explore the effect of viscous coupling at the ridges, by varying the effective viscosity in both ridges in an equal manner (Table 4.2). We then perform experiments in which we explore the effects of varying the stress-dependent rheologies on viscous coupling by changing the ridge's flow law parameters separately.

Lithospheric or shallow non-lithospheric upper mantle deformation is commonly modeled using flow laws for grain size insensitive dislocation creep, with characteristic stress exponents between $3.0 - 3.5$ (Hirth and Kohlstedt, 2003; Bürgmann and Dresen, 2008). This creep mechanism is broadly consistent with observations from deformed peridotites of ophiolites, interpreted to resemble the lithospheric mantle (ter Heege *et al.*, 2004). In our experiments, we do not include numerical representation of melt or grainsize evolution which may cause depth or strain rate-dependent changes in the viscosity field and gradient in the shallow upper mantle (Turner *et al.*, 2017; Sim *et al.*, 2020). To this end, we experiment with increasing the viscosity below a ridge first by lowering the stress exponent for dislocation creep n (Equation 4.4), see table 4.2 for an overview. For a given shear stress level this will increase the viscosity and decrease the strain rate leading to decreasing localization of deformation. A different way to conceptualize this change is that for a given flow (or: strain rate), a deforming mantle rock with a lower stress exponent will require higher stresses (or: lower strain rates) than a rock with a higher stress exponent, which translates to higher stress/strain rate ratios, and therefore effective viscosity. Lowering the stress exponent may also mimic a component of grain-size sensitive creep, which is known to occur in spreading ridges, through e.g., grain boundary sliding or diffusion creep (Warren and Hirth, 2006). We also show experiments in which the pre-factor A is changed (models 9, 10 – table 4.2), to increase the viscosity in the shallow mantle below the ridge
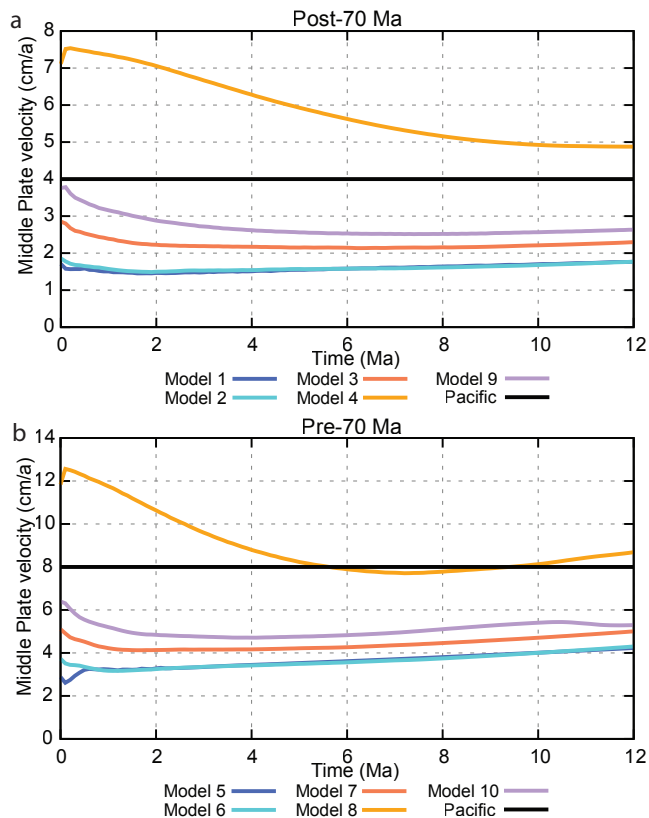
Figure 4.3 Modelled central plate velocities through time for boundary velocities of (**a**) 12 cm/a and (**b**) 20 cm/a. The colours represent the different modelling results (Table 4.2) while the black line represents the reconstructed velocity for the Pacific Plate (Figure 4.1c). The deceleration in models 4 and 8 is caused by the unrealistic widening of the spreading ridge over time.

without further lowering the influence of strain rate in the model (Table 4.2). This may resemble the stiffening caused by melting of mantle rock (Hirth and Kohlstedt, 1996). To resolve the high-strain rate and large viscosity gradients in the ridge we use an adaptive mesh refinement with a smallest cell resolution of 3.2 km in the top 50km of the domain, which stepwise increases to 100 km in the lower mantle.

4.3 Results

In our reference model (model 1), with an imposed boundary velocity of 12 cm/a and -4 cm/a on the right- and left-hand plates respectively, and with the same rheology for both ridge regions, we observe that the central

plate trails the fast-moving plate. In this set-up, the central plate develops
an absolute plate motion of 1.7 cm/a (Figure 4.3a). The ridges spread
symmetrically, or slightly asymmetrical with more accretion at the faster-
moving plate (Figure 4.4), and consequently obtain absolute motions up to
6 cm/a for the right-side ridge (R_r).

The non-lithosphere mantle below the ridge moves at a similar horizontal
velocity as the ridge and flows upward into the ridge at rates up to 3 cm/a to
accommodate the spreading (Figure 4.4). Flow in the lower mantle through
the 660km discontinuity replenishes the upper mantle over the entire width
of the model domain, to compensate for the lithospheric outflow, and is
smaller than 2 cm/a in the entire lower mantle. Near the fast-spreading
ridge (R_r) the upper mantle is actively being sucked towards the R_r to
accommodate the spreading at the ridge. This flow below the central plate
decreases with depth and magnitude towards the left-side ridge (L_r) and is
for half the extent of the plate slower than the absolute motion of the central
plate (Figure 4.4c). Below the central plate the underlying upper mantle
is dragged along with the right plate (Figure 4.4c). In other words, the
fast-moving plate is causing the central plate to move in the same direction.
This indicates that the central plate is coupled to the neighboring plates
through viscous coupling at and below the ridges, pulled along at the R_r
towards the fast-moving plate and resisted at the L_r by the slow-moving

Table 4.2 Overview of individual model parameters (stress exponent n and prefactor A)
and the resulting middle plate (MP) velocities as well as the velocity of the two ridges
R_l, R_r) in each model. Velocities are in $\mathrm{cm/a}$ where positive is in the direction of the
fast-moving plate. The last column indicates whether microplates form at the right-side
ridge.

Model	$n\ R_l$	$n\ R_r$	Prefactor $(\mathrm{Pa}^{-n}\mathrm{s}^{-1})$	Vel. MP (cm/a)	Vel. R_l (cm/a)	Vel. R_r	Microplate
Boundary velocity 12 cm/a							
1	3.5	3.5	6.51×10^{-16}	1.7	-1.2	6	no
2	3.0	3.0	6.51×10^{-16}	1.7	-1.1	6.5	yes
3	3.5	3.0	6.51×10^{-16}	2.2	0	7.4	yes
4	3.5	2.5	6.51×10^{-16}	4.9	0	-	no
9	3.5	3.0	0.651×10^{-16}	2.6	0	7	yes
Boundary velocity 20 cm/a							
5	3.5	3.5	6.51×10^{-16}	4	0	9.5	no
6	3.0	3.0	6.51×10^{-16}	4	0	10.8	yes
7	3.5	3.0	6.51×10^{-16}	4.7	0	11.3	yes
8	3.5	2.5	6.51×10^{-16}	8.1	0	-	no
10	3.5	3.0	0.651×10^{-16}	5.4	0	-	yes

Chapter 4

plate.

This is confirmed by experiments, again with equal rheology for both ridges, in which the absolute motion of the fast-moving right-hand plate is increased to 20 cm/a (model 5, table 4.2). In this case, the central plate has
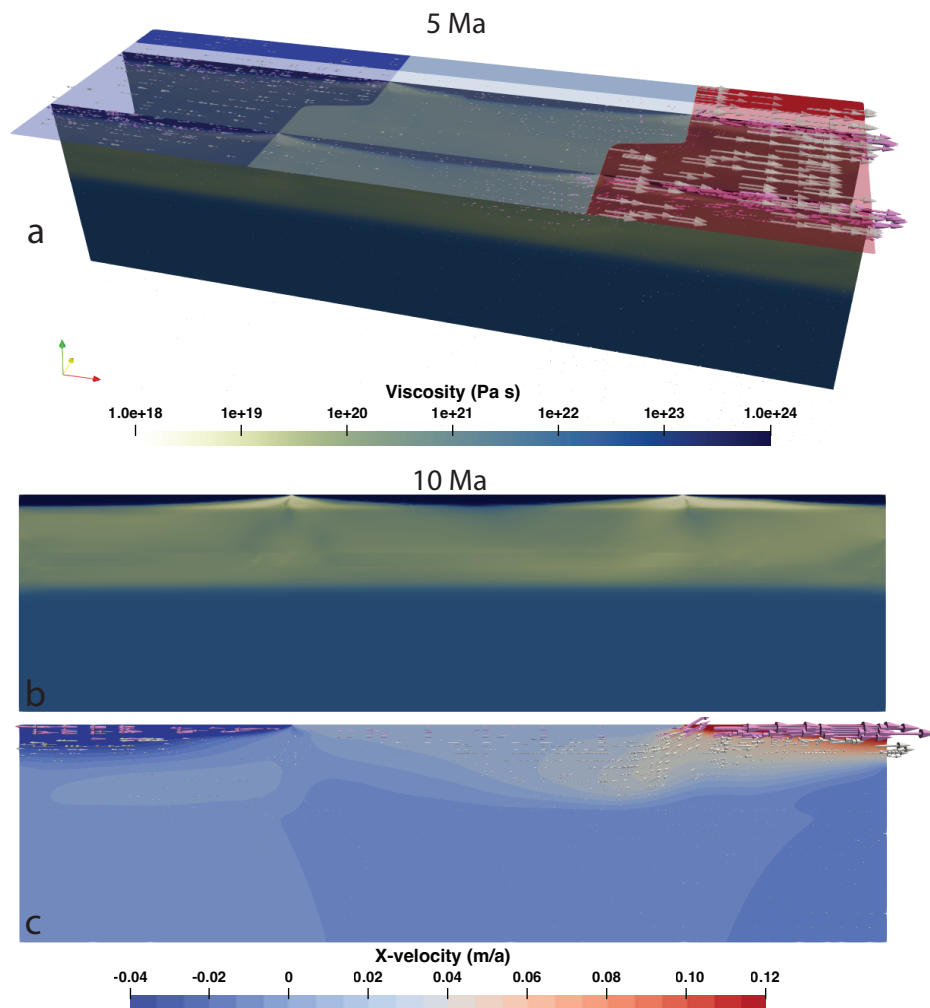
Figure 4.4 Snapshots of model 1. **a**) 3D representation of model 1 after 5 Ma, shown is the x-velocity distribution in a transparent top view. The snapshot also shows two depth-slices (up to 1500 km deep) to indicate the vertical distribution of the viscosity below the ridges. Pink arrows indicate the velocity on the surface and white arrows in the depth-slices. Bottom two panels: snapshot taken at $y = 500$ km of the viscosity (**b**) and x-component of the velocity (**c**) after 10 Ma. Here pink arrows show the velocity in the top 100km and the white arrows in the rest of the domain.

an absolute velocity of 4 cm/a trailing the right-hand plate (Figure 4.3b). Spreading is nearly symmetric, with Rr moving at rates of up to $\sim$ 9.5 cm/a to the right, and Lr remaining mantle-stationary (Table 4.2). This shows that the absolute motion of the middle plate depends on the absolute velocities of the neighboring plates. However, whereas our central plate moved 2-4 cm/a when the right-hand plate was moving at 12-20 cm/a, this is 2-2.5 times slower than the reconstructed Pacific Plate motions trailing the Izanagi Plate. We therefore performed additional numerical experiments to evaluate under which rheological conditions reconstructed rates for the central plate may be achieved.

We first tested whether the velocity of the middle plate depends on the absolute strength of the ridges. It is well known that the magnitude of viscosity has a first-order effect on plate boundary dynamics and the degree of coupling (Androvicova *et al.*, 2013; Behr *et al.*, 2022), so we investigated to what degree increasing the viscosity of the asthenosphere below the spreading ridge will increase the effectiveness of transferring plate motion forces between the two oceanic plates. We performed experiments in which we increased the strength of both ridges equally, by lowering the stress exponent n for dislocation creep from $n = 3.5$ to $n = 3.0$ (Table 4.2).

The results show that the central plate in this new setup (models 2 and 6) again follows the fastest moving, right-side plate, and with the same velocity as in the reference models (Figure 4.3). In other words, when the strength at both ridges increases equally, the enhanced coupling with the fast-moving plate is countered by the enhanced coupling with the opposite plate, and the net kinematic effect is the same.

An interesting difference in these experiments is that with the stronger sub-ridge shallow upper mantle, microplates form at the faster-spreading ridge R_r (Table 4.2). In both scenarios with 12 and 20 cm/a, the R_r first splits into two ridges creating another ridge-bounded plate. This new central plate is short-lived as after $\sim$ 1 Ma the ridge adjacent to the middle plate ceases spreading and the ridge closest to the fast-moving plate accommodates the full spreading rate. This 'ridge-jump' at R_r is roughly 50 km in the model pulled with 12 cm/a and 150 km when pulled with 20 cm/a. However, in both models a microplate remains where the two ridges meet the transform fault. This microplate grows over time, trails the faster-moving plate, and rotates slightly (Supplementary Movie 1). After 3-5 Ma of independent microplate motion and growth, one of the ridges bounding these microplates stops spreading and the microplate merges with the fast-moving plate. This development closely mimics the microplates from the East Pacific Rise, such as the Easter and Juan Fernández, and Bauer mi-

croplates, that also formed at high full spreading rates of ~ 14 cm/a (Naar and Hey, 1989; Eakins and Lonsdale, 2003; Neves *et al.*, 2003. These double ridge-segments or microplates do not form at the slower spreading L_r, which maintains its original orientation throughout the experiments. The enhanced sub-ridge shallow upper mantle strength thus produces spreading behavior that closely mimics reconstructed fast-spreading ridge behavior.

Interestingly, the development of these microplates does not influence the velocity of the original central plate. So, increasing the amount of viscous coupling at both ridges influences the spreading behavior on ridge R_r, but it does not change the velocity of the central plate. The pull of the fast-moving right plate thus appears to be partitioned over two ridges, but the kinematic effect on the original central plate remains the same. Generation of stronger rheology below both ridges is thus insufficient to develop faster central plate motion.

To test the influence of a spreading-rate dependent rheology, we prescribed different rheologies to both ridges in a next set of experiments by prescribing a lower stress exponent n for dislocation creep at the faster-spreading ridge R_r. When using $n_{L_r} = 3.5$ and $n_{R_r} = 3.0$ (models 3 and 7), the velocity of the central plate increased from 1.7 to 2.2 cm/a for the right plate pulling with 12 cm/a, and to 4.7 from 4.0 cm/a, for the right plate moving at 20 cm/a. This is an increase of ~ 30 and 20 % compared to the previously described models with the same boundary conditions (Figure 4.3). In both these models, the faster spreading ridge R_r also developed a microplate, adjacent to the transform fault in model 7 (Figure 4.5) and at the ridge through ridge propagation in model 3.

With a different value for n in both ridges we obtain faster central plate velocities, although still not equal to the reconstructed Pacific Plate motions. When we use $n = 2.5$, in the R_r and $n = 3.5$ in the L_r. (model 4 and 8), we obtain central plate velocities resembling the reconstructed motions (Figure 4.3a,b). However, spreading in these models is accommodated by an unrealistic large rift zone which does not resemble a MOR. Therefore, in the next experiments (models 9 and 10) we increase the ridges viscosity through the pre-factor A in the R_r while we keep the stress exponents for dislocation creep similar as in models 3 and 7 (Table 4.2) to keep a localized spreading center. The 10-fold decrease in pre-factor results in central plate velocities of 2.6 and 5.4 cm/a in models 9 and 10, respectively. Model 9 shows similar microplate development as previously described, forming two microplates simultaneously at both ends of the transform fault. The R_r in model 10 behaves differently, as multiple ridges form and continuously change shape, eventually forming an additional oceanic plate over the entire
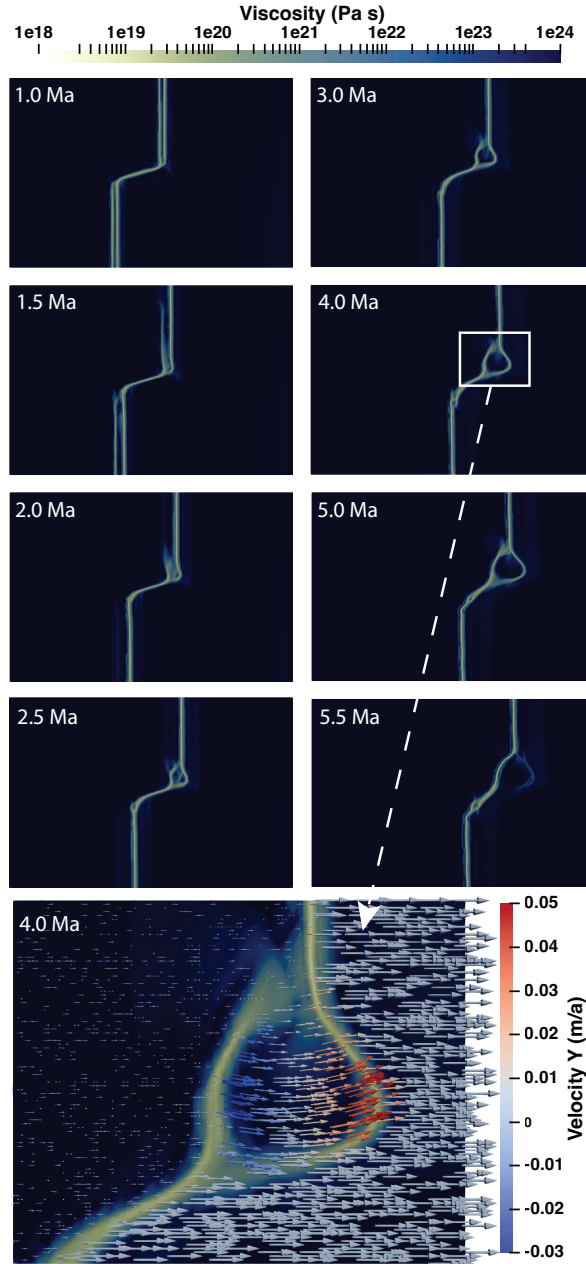
Figure 4.5 Top view of the evolution of the right ridge in model 7, where a microplate forms, grows, and merges with the fast-moving plate. Shown are snapshots of the viscosity in the right half of the domain in 0.5 or 1 Ma timesteps. The rotation of the microplate is shown in the bottom figure, which is a zoom in of the R_r at 4.0 Ma and includes arrows representing the full velocity vector (z-component = 0) coloured by the y-component of the velocity at the surface.

width of the domain that moves with 10 cm/a trailing the fast right plate (Figure 4.6). Although the central plate in these last two models only moves with $\sim 70\%$ of the reconstructed Pacific Plate motions, the newly created plate in model 10 does have a velocity as high as 10 cm/a (Figure 4.6). The new plate has a left plate (the original central plate) that moves in the same direction whereby their shared spreading ridge would not provide a resisting force like in all other models. This indicates that viscous coupling may indeed pull plates along across a spreading center while spreading is active at a ridge that is also moving in the mantle frame.

4.4 Discussion

Our experiments show that our hypothesis of viscous coupling across ridge-wedges successfully generates an absolute motion of an oceanic plate that is bounded by ridges, trailing the fastest moving plate. However, to obtain rates that resemble the reconstructed motion of the Pacific Plate requires, we must invoke a mechanism that increases sub-ridge viscosity and enhances coupling at faster-spreading ridges (e.g., strain hardening). Our experiments require that ridges strengthen further than can be explained by 'typical' diffusion or dislocation creep flow laws, for example a stress exponent that is atypical of end-member creep mechanisms ($n = 2.5$) in models 4 and 8 (Hirth and Kohlstedt, 2003; ter Heege *et al.*, 2004). However, three other mechanisms that were not taken into account in these widely used flow laws may allow for geologically realistic, enhanced 'strain-hardening'.

4.4.1 Grain-scale hypotheses for enhanced sub-ridge viscous coupling

First, during dislocation creep the creation and movement of dislocations creates internal stresses within and between grains (Wallis *et al.*, 2020) that lead to dislocation interactions, a process called "backstress" (cf. Thom and Kirkpatrick, 2023). Recent experimental work on single olivine crystals (Wallis *et al.*, 2022) and theoretical calculations of flow behavior due to dislocation interactions (Thom and Kirkpatrick, 2023) indicate that dislocation build-up may lead to major magnitudes of stored internal stress (on the order of 6-10 GPa), resulting in an effectively strain hardening mechanism. This internal build-up may then lead to pulses of plasticity, or creep transients (Wallis *et al.*, 2021). In fact, the contribution of transient creep to total deformation is greater for materials that deform by lower long-term stresses or higher temperatures (Hansen *et al.*, 2021), which applies well to the asthenospheric mantle below faster-spreading ridges, and may effectively act as a stress guide between the two adjacent oceanic plates.
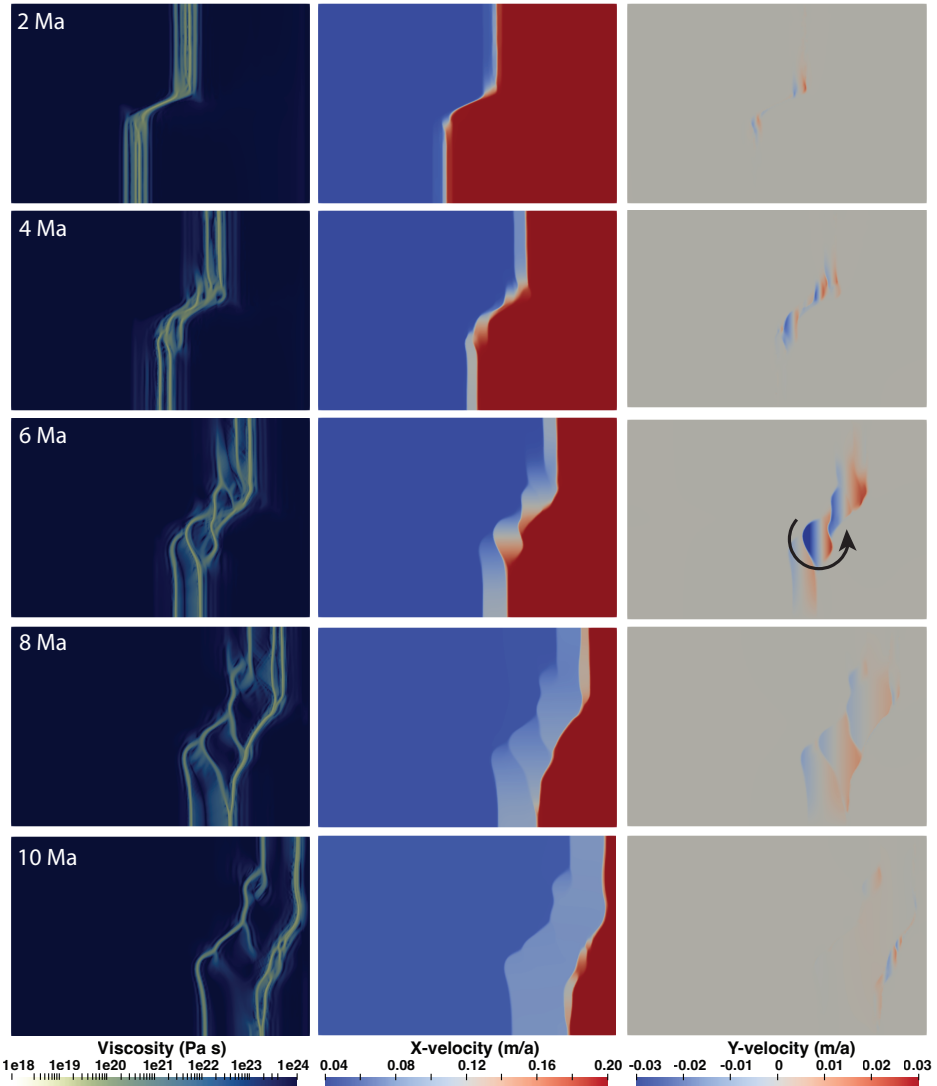
Figure 4.6 Top view (3000 × 2000 km) snapshots of the right ridge in model 10 showing the viscosity (left column), x-velocity (middle column) and y-velocity (right column) at five moments. These indicate the development of the right ridge splitting in two before forming multiple counterclockwise rotating microplates that eventually merge into one new oceanic plate moving at 10 cm/a after the right plate.

Therefore, even for mantle rocks deforming exclusively by "true" dislocation creep (i.e., no grain size sensitivity) the thermal and mechanical stratification across the broad lithosphere-asthenosphere-lithosphere zone beneath the MOR axis may experience stress build-up and effective strain hardening

that glues the plates together on short ($<$ 1 Ma) timescales.

In addition, changing the stress exponent can mimic the operation of grain-size sensitive creep mechanisms among which are diffusion or dislocation accommodated grain boundary sliding (Warren and Hirth, 2006) or grain-size sensitive dislocation creep (Bystricky and Mackwell, 2001). Dynamic recrystallization due to dislocation creep may result in grain size reduction in the lithosphere or asthenosphere, which in turn may trigger increasing proportions of grain boundary sliding (Chen *et al.*, 2006; Bürgmann and Dresen, 2008) causing a feedback wherein an increasing contribution from grain-size sensitive creep (and therefore decrease in the stress exponent) leads to sufficient 'strength' increase immediately below the ridge axis to retain viscous connectivity across the asthenospheric wedge. This may be even more effective at fast, hot spreading ridges, where thermal gradients are even higher (and therefore diffusion is even easier) as long as some dislocation activity is still present.

Finally, faster spreading ridges require higher melt extraction and melt-induced dehydration of the residual, depleted mantle rock (Bredow *et al.*, 2017). While the melt itself may weaken the ridge, the residual depleted mantle may stiffen by a factor >100 due to the extraction of water (Hirth and Kohlstedt, 1996; Ito *et al.*, 1999), potentially leading to viscous hardening based on the amount of melt extraction and thus spreading velocity.

Because ridge push has no effect on a plate surrounded by ridges, the only alternative mechanism to explain absolute motion of non-subducting plates is mantle drag (Clennett *et al.*, 2023). For the Pacific Plate, this would require long-lasting upper mantle motion rates that must have exceeded the reconstructed Pacific plate motion of 9 cm/a, i.e., an order of magnitude higher than lower mantle sinking rates (van der Meer *et al.*, 2018) and up to two order of magnitude higher than associated ambient lower mantle convection rates (Chapter 1). Moreover, this mantle motion would act in a direction that is opposite to the reconstructed motion of absolute drift of the Hawaiian hotspot (Hassan *et al.*, 2016; Torsvik *et al.*, 2017) and have to adjust to the increasing size of the Pacific Plate that by late Cretaceous times straddles two hemispheres. It would also need to suddenly cease when the Pacific Plate started subducting in the west and changed its absolute motion. Therefore, we consider that viscous coupling across the Pacific Plate's ridges, which occurs in all our experiments, offers a better explanation.

4.4.2 Possible implications for plate driving forces and global plate reorganizations

Realizing that intraplate stress induced by slab pull may propagate across spreading ridges offers novel and exciting opportunities to explain several enigmatic observations. For instance, the reorientation of Pacific Plate motion around 85 Ma followed the initiation of two new subduction zones in the northern Panthalassa ocean: one north-dipping, forming the Kronotsky intra-oceanic arc, and one south-dipping and retreating, forming the Olyutorsky arc (Konstantinovskaya, 2002; Shapiro and Solov'ev, 2009; Domeier *et al.*, 2017; Vaes *et al.*, 2019). The Pacific Plate, however, was separated from these subducting plate boundaries by two plates that spread away: the Kula Plate that subducted below the Kronotsky Arc (Wright *et al.*, 2016; Domeier *et al.*, 2017) and along the Olyutorsky plate in the upper plate of the northward retreating Olyutorksy subduction zone (Vaes *et al.*, 2019). Coupling at these northwards moving ridges may aid to the explanation why the Pacific Plate changed absolute motion from westwards to northward around 85 Ma. In addition, the $\sim 55-50$ Ma arrest of the northward pull of the Olyutorsky subduction zone, and the $\sim 45-40$ Ma arrest of the Kronotsky subduction zone thus removed northward pull on the Pacific Plate through the Kula-Pacific and Olyutorskt-Pacific ridges around these times. These changes may thus have contributed to the westward reorientation of Pacific plate motion, in tandem with the onset of subduction of the Pacific Plate in the west.

We showed that two oceanic plates, separated by a ridge, with different magnitudes of plate motion may exert a pull on each other which would be opposite to the ridge push force and depending on the magnitude of the plate motions. This seemingly paradoxical combination of forces may explain why plates mainly surrounded by MORs may still be in extension, such as the African Plate (Gaina *et al.*, 2013) or the Antarctic Plate (Faccenna *et al.*, 2008). It may also explain why microcontinents, potentially aided by plumes, may break off supercontinents into their internal oceans like de Cimmerides (Şengör *et al.*, 2023), Argoland (Advokaat and Hinsbergen, 2023) or the hypothetical Tibetan Himalayan microcontinent (van Hinsbergen *et al.*, 2012). Likewise, viscous coupling across spreading ridges also implies that motion of a subducting plate is not only subject to its own basal drag, but also to that of its neighbors. Those effects may be important in the assessment of intra-plate stress evolution (Warners-Ruckstuhl *et al.*, 2012; Wouters *et al.*, 2021) but, most importantly, require a mantle frame of plate motion for the analysis of the viscous coupling across the

Chapter 4

ridge wedge.

Finally, viscous coupling at MORs provides novel ways to explain perplexing series of global plate reorganizations. Changing plate motions and reorientation of plate boundaries within such reorganizations seem to affect multiple plates, within short time spans of only a few Ma, most famously around 50 Ma (Rona and Richardson, 1978), but a unifying underlying physical mechanism has so far been lacking. As slab pull is the main driver of plate tectonics, subduction initiation, for instance as a result of plume activity or collisions and subduction zone transferal (Domeier *et al.*, 2017; Stern and Gerya, 2018; van Hinsbergen *et al.*, 2021) may be a logical initiator for plate reorganizations. Although subduction initiation may cause plate motion changes, that may itself cause subduction initiation, such plate tectonic chain reactions (Gürer *et al.*, 2022) are much slower than suggested for global plate reorganizations (Rona and Richardson, 1978; Matthews *et al.*, 2012; Seton *et al.*, 2015). With coupled ridges, a change in slab pull force of one plate may immediately impact the force balance of its neighbors, offering a mechanism to rapidlly propagate changes in plate motion. The global plate reorganization around 50 Ma likely resulted from paleogeographic coincidences, such as the arrival of ridges or continents in trenches in the northern and western Pacific region, or between India and Asia, but coupling at ridges may explain how these changes have rapidly propagated globally. This did not only affect plate motion, but also orogenesis, volcanism, and through that, global climate and environment. To study the unifying underlying physics, we identify the study of the strength and rheological evolution of mantle below spreading ridges of key importance to improve our understanding of the global earth system.

A

Appendix

We here recall the equations of the chapter 2 and show the equations for normalization. Where $n_{c,j}$ is the number of particles per composition c in a cell j and N_c is the total number of c-particles divided by the number of cells.

$$\rho_{c,j} = \frac{n_{c,j}}{N_c} \tag{A.1}$$

$$P_{j,c} = \frac{\rho_{c,j}}{\sum\limits_{c=1}^{C} \rho_{c,j}} \tag{A.2}$$

$$P_j = \frac{\sum\limits_{c=1}^{C} \rho_{c,j}}{\sum\limits_{j=1}^{M} \sum\limits_{c=1}^{C} \rho_{c,j}} \tag{A.3}$$

$$S_{pd} = -\sum_{j=1}^{M} P_j \ln P_j \tag{A.4}$$

$$S_j = -\sum_{c=1}^{C} P_{j,c} \ln P_{j,c} \tag{A.5}$$

$$S = \sum_{j=1}^{M} P_j S_j \tag{A.6}$$

$$S_{pd\,normalized} = \frac{S_{pd}}{\ln M} \tag{A.7}$$

$$S_{j\,normalized} = \frac{S_j}{\ln C} \tag{A.8}$$

$$S_{normalized} = \frac{S}{\ln C} \tag{A.9}$$

Four examples are given below, each with different distributions of particles and compositions in a small rectangular grid of 4 cells. We use these four examples to illustrate how the configurational entropy is affected by certain distributions. The background of the cells is colored according to S_j in grayscale, from 0 (black) to 1 (white) and the tracers shown are randomly given a position in the cell appointed to them.
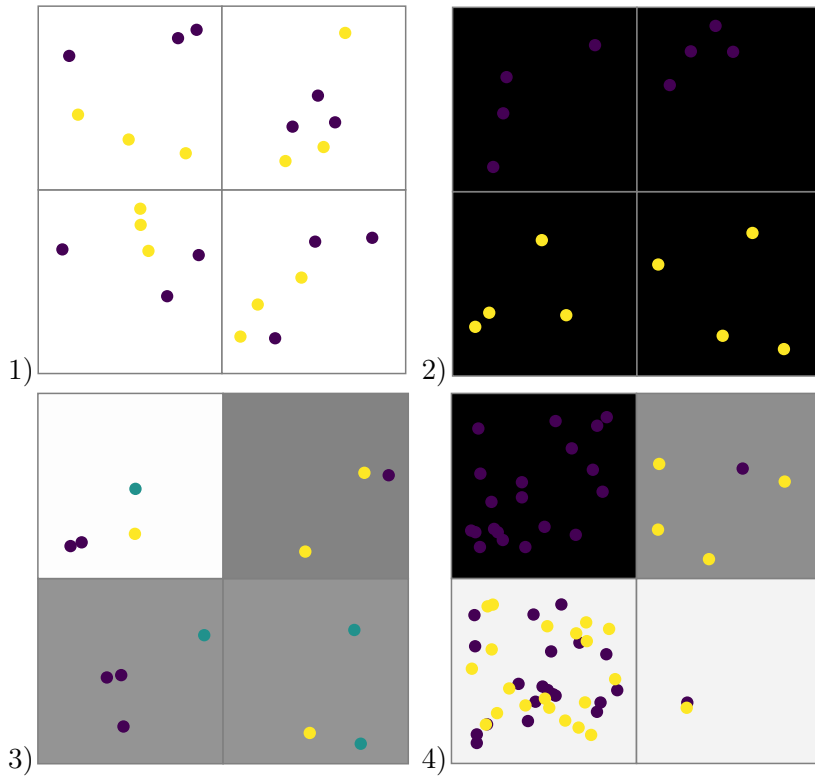
Examples 1-4 of configurational entropy calculations.

Example 1 – equal distribution, fully mixed

We start with a uniform distribution of particles with completely mixed compositions in each cell. The number of expected particles per composition per cell (N_c) is equal to the sum of the number of particles in that cell, this also reflected in vector P_j which is equal for all cells – and therefore $S_{pd\,normalized}$ is equal to 1 (after normalization) indicating a uniform distribution. The local entropy S_j per cell is defined through $P_{j,c}$ which is equally distributed and equal to the normalization. Therefore, it indicates perfect mixing for all four cells. The global entropy combines P_j and $S_{j\,normalized}$ and is therefore equal to the endmember, which is 1.

$$n_{c,j} = \begin{pmatrix} 3 & 3 & 3 & 3 \\ 3 & 3 & 3 & 3 \end{pmatrix} \tag{A.10}$$

$$N_C = \begin{pmatrix} 3 \\ 3 \end{pmatrix} \tag{A.11}$$

$$\rho_{c,j} = \begin{pmatrix} 1 & 1 & 1 & 1 \\ 1 & 1 & 1 & 1 \end{pmatrix} \tag{A.12}$$

$$P_{c,j} = \begin{pmatrix} 1/2 & 1/2 & 1/2 & 1/2 \\ 1/2 & 1/2 & 1/2 & 1/2 \end{pmatrix} \tag{A.13}$$

$$P_j = \begin{pmatrix} 1/4 & 1/4 & 1/4 & 1/4 \end{pmatrix} \tag{A.14}$$

$$S_{pd} = 1.38629 \tag{A.15}$$

$$S_j = \begin{pmatrix} 0.693 & 0.693 & 0.693 & 0.693 \end{pmatrix} \tag{A.16}$$

$$S = 0.69314 \tag{A.17}$$

$$S_{pd\,normalized} = \frac{1.38629}{\ln 4} = 1 \tag{A.18}$$

$$S_{j\,normalized} = \begin{pmatrix} 1 & 1 & 1 & 1 \end{pmatrix} \tag{A.19}$$

$$S_{normalized} = \frac{0.69314}{\ln 2} = 1 \tag{A.20}$$

Example 2 – equal distribution, no mixing

The spatial distribution of particles is the same as in example 1 but compositions are not mixed, so $S_{pd\,normalized}$ is still 1. $P_{j,c}$ is either one or zero per composition which both will lead to a zero for the local entropy which is therefore 0 for all four cells. As this local entropy feeds into the global entropy S, that is also 0.

$$n_{c,j} = \begin{pmatrix} 0 & 0 & 4 & 4 \\ 4 & 4 & 0 & 0 \end{pmatrix} \tag{A.21}$$

$$N_C = \binom{2}{2} \tag{A.22}$$

$$\rho_{c,j} = \begin{pmatrix} 0 & 0 & 2 & 2 \\ 2 & 2 & 0 & 0 \end{pmatrix} \tag{A.23}$$

$$P_{c,j} = \begin{pmatrix} 0 & 0 & 1 & 1 \\ 1 & 1 & 0 & 0 \end{pmatrix} \tag{A.24}$$

$$P_j = \begin{pmatrix} 1/4 & 1/4 & 1/4 & 1/4 \end{pmatrix} \tag{A.25}$$

$$S_{pd} = 1.38629 \tag{A.26}$$

$$S_j = \begin{pmatrix} 0 & 0 & 0 & 0 \end{pmatrix} \tag{A.27}$$

$$S = 0 \tag{A.28}$$

$$S_{pd\,normalized} = \frac{1.38629}{\ln 4} = 1 \tag{A.29}$$

$$S_{j\,normalized} = \begin{pmatrix} 0 & 0 & 0 & 0 \end{pmatrix} \tag{A.30}$$

$$S_{normalized} = \frac{0}{\ln 2} = 0 \tag{A.31}$$

Example 3 – random example with 3 compositions

The distribution is ideally mixed as the expected number of particles in each cell is 3.5. P_j is therefore not the same in each cell, but close to that. $S_{pd\,normalized}$ is therefore close to 1 in this example. The compositions are not equally distributed, the top left cell is close to the expected distribution (N_c) and therefore has a local entropy close to 1 (after normalization by $ln(3)$). The bottom cells are equally far off expected values (1.5 off for purple, and 1 for the other colors) and have therefore the same S_j. As three cells have local entropy of about 0.5, but distributions are somewhat equal, the global entropy is 0.678 – which reflects the weighted average of S_j.

$$n_{c,j} = \begin{pmatrix} 3 & 0 & 2 & 1 \\ 1 & 2 & 1 & 0 \\ 0 & 1 & 1 & 2 \end{pmatrix} \tag{A.32}$$

$$N_C = \begin{pmatrix} 1.5 \\ 1 \\ 1 \end{pmatrix} \tag{A.33}$$

$$\rho_{c,j} = \begin{pmatrix} 2 & 0 & 4/3 & 2/3 \\ 1 & 2 & 1 & 0 \\ 0 & 1 & 1 & 2 \end{pmatrix} \tag{A.34}$$

$$P_{c,j} = \begin{pmatrix} 2/3 & 0 & 4/10 & 1/4 \\ 1/3 & 2/3 & 3/10 & 0 \\ 0 & 1/3 & 3/10 & 3/4 \end{pmatrix} \tag{A.35}$$

$$P_j = \begin{pmatrix} 1/4 & 1/4 & 5/18 & 2/9 \end{pmatrix} \tag{A.36}$$

$$S_{pd} = 1.3832 \tag{A.37}$$

$$S_j = \begin{pmatrix} 0.6365 & 0.6365 & 1.0888 & 0.5623 \end{pmatrix} \tag{A.38}$$

$$S = 0.74569 \tag{A.39}$$

$$S_{pd\,normalized} = \frac{1.38629}{\ln 4} = 0.99777 \tag{A.40}$$

$$S_{j\,normalized} = \begin{pmatrix} 0.5794 & 0.5794 & 0.9912 & 0.5119 \end{pmatrix} \tag{A.41}$$

$$S_{normalized} = \frac{0.74569}{\ln 3} = 0.67876 \tag{A.42}$$

Example 4 – no equal distribution

This last case showcases an uneven particle distribution, with an expected number of particles of 16.75 ($\sum N_c$) that is not recovered in any cell. The vector P_j is therefore not balanced and $S_{pd\,normalized}$ is 0.689, indicating an imperfect particle distribution. The top left is obviously unmixed with S_j = 0. The bottom cells have the same ratio of compositions and therefore a similar high S_j. as the 50/50 compositional ratio is not too far off the ideal ratio. The bottom cells contribute significantly to the global entropy S and the top left cell has a sizable weighing factor ($P_3 = 0.238$) but as its $S_j = 0$ it does therefore not contribute to the total entropy.

$$n_{c,j} = \begin{pmatrix} 20 & 1 & 20 & 1 \\ 20 & 1 & 0 & 4 \end{pmatrix} \tag{A.43}$$

$$N_C = \begin{pmatrix} 10.5 \\ 6.25 \end{pmatrix} \tag{A.44}$$

$$\rho_{c,j} = \begin{pmatrix} 1.9 & 0.095 & 1.905 & 0.095 \\ 3.2 & 0.16 & 0 & 0.64 \end{pmatrix} \tag{A.45}$$

$$P_{c,j} = \begin{pmatrix} 0.373 & 0.373 & 1 & 0.129 \\ 0.627 & 0.627 & 0 & 0.871 \end{pmatrix} \tag{A.46}$$

$$P_j = \begin{pmatrix} 0.638 & 0.0319 & 0.2381 & 0.0919 \end{pmatrix} \tag{A.47}$$

$$S_{pd} = 0.9576 \tag{A.48}$$

$$S_j = \begin{pmatrix} 0.66 & 0.66 & 0 & 0.385 \end{pmatrix} \tag{A.49}$$

$$S = 0.478 \tag{A.50}$$

$$S_{pd\,normalized} = \frac{0.9576}{\ln 4} = 0.6907 \tag{A.51}$$

$$S_{j\,normalized} = \begin{pmatrix} 0.953 & 0.953 & 0 & 0.556 \end{pmatrix} \tag{A.52}$$

$$S_{normalized} = \frac{0.478}{\ln 2} = 0.689 \tag{A.53}$$

Supplementary information

All figures, supplementary figures and supplementary movies can be accessed in digital form through a Google Drive folder, which is organized per chapter and can be accessed through the following link:

https://drive.google.com/drive/folders/192YrKvaVGtF9kgAJMo7IIU9KNr7eQLhb

Or by scanning the QR-code below.

References

Advokaat, E. L. and D. J. van Hinsbergen (2023). "Finding Argoland: Reconstructing a microcontinental archipelago from the SE Asian accretionary orogen". *Gondwana Research*. DOI: 10.1016/j.gr.2023.10.005.

Androvicova, A., H. Čížková, and A. van den Berg (2013). "The effects of rheological decoupling on slab deformation in the Earth's upper mantle". *Stud. Geophys. Geod.* 57, pp. 460–481. DOI: 10.1007/s11200-012-0259-7.

Argus, D. F., W. R. Peltier, G. Blewitt, and C. Kreemer (2021). "The viscosity of the top third of the lower mantle estimated using GPS, GRACE, and relative sea level measurements of glacial isostatic adjustment". *Journal of Geophysical Research: Solid Earth* 126.5, e2020JB021537. DOI: 10.1029/2020JB021537.

Arnould, M., N. Coltice, N. Flament, and C. Mallard (2020). "Plate tectonics and mantle controls on plume dynamics". *Earth and Planetary Science Letters* 547, p. 116439. DOI: 10.1016/j.epsl.2020.116439.

Ballmer, M. D., C. Houser, J. W. Hernlund, R. M. Wentzcovitch, and K. Hirose (2017). "Persistence of strong silica-enriched domains in the Earth's lower mantle". *Nature Geoscience* 10.3, pp. 236–240. DOI: 10.1038/NGEO2898.

Ballmer, M. D., L. Schumacher, V. Lekic, C. Thomas, and G. Ito (2016). "Compositional layering within the large low shear-wave velocity provinces in the lower mantle". *Geochemistry, Geophysics, Geosystems* 17.12, pp. 5056–5077. DOI: 10.1126/sciadv.1500815.

Bangerth, W., J. Dannberg, M. Fraters, R. Gassmoeller, A. Glerum, T. Heister, and J. Naliboff (July 2021). *ASPECT v2.3.0*. Version v2.3.0. DOI: 10.5281/zenodo.5131909. URL: https://doi.org/10.5281/zenodo.5131909.

Barry, T., J. H. Davies, M. Wolstencroft, I. Millar, Z Zhao, P Jian, I Safonova, and M. Price (2017). "Whole-mantle convection with tectonic plates preserves long-term global patterns of upper mantle geochemistry". *Scientific reports* 7.1, pp. 1–9. DOI: 10.1038/s41598-017-01816-y.

Becker, T. and C. Faccenna (2011). "Mantle conveyor beneath the Tethyan collisional belt". *Earth Planet. Sci. Lett.* 310, pp. 453–461. DOI: 10.1016/j.epsl.2011.08.021.

Běhounková, M. and H. Čížková (2008). "Long-wavelength character of sub-ducted slabs in the lower mantle". *Earth and Planetary Science Letters* 275.1-2, pp. 43–53. DOI: 10.1016/j.epsl.2008.07.059.

Behr, W. M. and T. W. Becker (2018). "Sediment control on subduction plate speeds". *Earth and Planetary Science Letters* 502, pp. 166–173. DOI: 10.1016/j.epsl.2018.08.057.

Behr, W. M., A. F. Holt, T. W. Becker, and C. Faccenna (2022). "The effects of plate interface rheology on subduction kinematics and dynamics". *Geophysical Journal International* 230.2, pp. 796–812. DOI: 10.1093/gji/ggac075.

Bercovici, D., G. Schubert, and Y. Ricard (2015). "Abrupt tectonics and rapid slab detachment with grain damage". *Proceedings of the National Academy of Sciences* 112.5, pp. 1287–1291. DOI: 10.1073/pnas.1415473112.

Billen, M. and K. Arredondo (2018). "Decoupling of plate-asthenosphere motion caused by non-linear viscosity during slab folding in the transition zone". *Phys. Earth. Planet. Inter.* 281, pp. 17–30. DOI: 10.1016/j.pepi.2018.04.011.

Bina, C. R. and G. Helffrich (1994). "Phase transition Clapeyron slopes and transition zone seismic discontinuity topography". *Journal of Geophysical Research: Solid Earth* 99.B8, pp. 15853–15860. DOI: 10.1029/94JB00462.

Boschman, L. M. and D. J. van Hinsbergen (2016). "On the enigmatic birth of the Pacific Plate within the Panthalassa Ocean". *Science Advances* 2.7, e1600022. DOI: 10.1126/sciadv.1600022.

Boutoux, A., A. Briaud, C. Faccenna, P. Ballato, F. Rossetti, and E. Blanc (2021). "Slab folding and surface deformation of the Iran mobile belt". *Tectonics* 40.6, e2020TC006300. DOI: 10.1029/2020TC006300.

Bower, D., M. Gurnis, and N. Flament (2015). "Assimilating lithosphere and slab history in 4-D Earth models". *Phys. Earth. Planet. Inter.* 238, pp. 8–22. DOI: 10.1016/j.pepi.2014.10.013.

Bredow, E., B. Steinberger, R. Gassmöller, and J. Dannberg (2017). "How plume-ridge interaction shapes the crustal thickness pattern of the Réunion hotspot track". *Geochemistry, Geophysics, Geosystems*. DOI: 10.1002/2017GC006875.

Briaud, A., R. Agrusta, C. Faccenna, F. Funiciello, and J. van Hunen (2020). "Topographic fingerprint of deep mantle subduction". *Journal of*

Geophysical Research: Solid Earth 125, e2019JB017962. DOI: 10.1029/2019JB017962.

Bull, A., M. Domeier, and T. Torsvik (2014). "The effect of plate motion history on the longevity of deep mantle heterogeneities". *Earth Planet. Sci. Lett.* 401, pp. 172–182. DOI: 10.1016/j.epsl.2014.06.008.

Bull, A., A. McNamara, T. Becker, and J. Ritsema (2010). "Global scale models of the mantle flow field predicted by synthetic tomography models". *Phys. Earth. Planet. Inter.* 182, pp. 129–138. DOI: 10.1016/j.pepi.2010.03.004.

Bürgmann, R. and G. Dresen (2008). "Rheology of the lower crust and upper mantle: Evidence from rock mechanics, geodesy, and field observations". *Annu. Rev. Earth Planet. Sci.* 36, pp. 531–567. DOI: 10.1146/annurev.earth.36.031207.124326.

Burke, K. and T. H. Torsvik (2004). "Derivation of large igneous provinces of the past 200 million years from long-term heterogeneities in the deep mantle". *Earth and Planetary Science Letters* 227.3-4, pp. 531–538. DOI: 10.1016/j.epsl.2004.09.015.

Burstedde, C., L. C. Wilcox, and O. Ghattas (2011). "`p4est`: Scalable Algorithms for Parallel Adaptive Mesh Refinement on Forests of Octrees". *SIAM Journal on Scientific Computing* 33.3, pp. 1103–1133. DOI: 10.1137/100791634.

Butterworth, N., A. Talsma, R. Müller, M. Seton, H.-P. Bunge, B. Schuberth, G. Shephard, and C. Heine (2014). "Geological, tomographic, kinematic and geodynamic constraints on the dynamics of sinking slabs". *Journal of Geodynamics* 73, pp. 1–13. DOI: 10.1016/j.jog.2013.10.006.

Bystricky, M. and S. Mackwell (2001). "Creep of dry clinopyroxene aggregates". *Journal of Geophysical Research: Solid Earth* 106.B7, pp. 13443–13454. DOI: 10.1029/2001JB000333.

Camesasca, M., M. Kaufman, and I. Manas-Zloczower (2006). "Quantifying fluid mixing with the Shannon entropy". *Macromolecular theory and simulations* 15.8, pp. 595–607. DOI: 10.1002/mats.200600037.

Cao, X., N. Flament, and R. D. Müller (2021). "Coupled evolution of plate tectonics and basal mantle structure". *Geochemistry, Geophysics, Geosystems* 22, e2020GC009244. DOI: 10.1029/2020GC009244.

Capitanio, F., C. Faccenna, S. Zlotnik, and D. Stegman (2011). "Subduction dynamics and the origin of Andean orogeny and the Bolivian orocline". *Nature* 480. DOI: 10.1038/nature10596.

Capitanio, F., D. Stegman, L. Moresi, and W. Sharples (2010). "Upper plate controls on deep subduction, trench migrations and deformations at convergent margins". *Tectonophysics* 483, pp. 80–92.

Cerpa, N., B. Guillaume, and J.Martinod (2018). "The interplay between overriding plate kinematics, slab dip and tectonics". *Geophy. J. Int.* 215, pp. 1789–1802. DOI: 10.1093/gji/ggy365.

Chapman, J. B., J. E. Shields, M. N. Ducea, S. R. Paterson, S. Attia, and K. E. Ardill (2021). "The causes of continental arc flare ups and drivers of episodic magmatic activity in Cordilleran orogenic systems". *Lithos* 398, p. 106307. DOI: 10.1016/j.lithos.2021.106307.

Chelle-Michou, C., M. Chiaradia, D. Selby, M. Ovtcharova, and R. A. Spikings (2015). "High-resolution geochronology of the Coroccohuayco porphyry-skarn deposit, Peru: A rapid product of the Incaic orogeny". *Economic Geology* 110.2, pp. 423–443. DOI: 10.2113/econgeo.110.2.423.

Chen, S, T Hiraga, and D. L. Kohlstedt (2006). "Water weakening of clinopyroxene in the dislocation creep regime". *Journal of Geophysical Research: Solid Earth* 111.B8. DOI: 10.1029/2005JB003885.

Chen, Y.-W., J. Wu, and J. Suppe (2019). "Southward propagation of Nazca subduction along the Andes". *Nature* 565.7740, pp. 441–447. DOI: 10.1038/s41586-018-0860-1.

Choi, H., S.-S. Kim, and S.-H. Park (2021). "Tectonic constraints on formation and evolution of microplates in the Indian and Pacific Oceans: reviews and statistical inferences". *Geosciences Journal* 25, pp. 799–811. DOI: 10.1007/s12303-021-0005-7.

Christensen, U. R. and D. A. Yuen (1985). "Layered convection induced by phase transitions". *Journal of Geophysical Research: Solid Earth* 90.B12, pp. 10291–10300. DOI: 10.1029/JB090iB12p10291.

Ciskova, H., J. van Hunen, A. van den Berg, and N. Vlaar (2002). "The influence of rheological weakening and yield stress on the interaction of slabs with the 670 km discontinuity". *Earth Planet. Sci. Lett.* 199, pp. 447–457. DOI: 10.1016/S0012-821X(02)00586-1.

Čížková, H., A. van den Berg, W. Spakman, and C. Matyska (2012). "The viscosity of the earth's lower mantle inferred from sinking speed of subducted lithosphere". *Phys. Earth. Planet. Inter.* 200–201, pp. 56–62. DOI: 10.1016/j.pepi.2012.02.010.

Čížková, H. and C. Bina (2013). "Effects of mantle and subduction-interface rheologies on slab stagnation and trench rollback". *Earth Planet. Sci. Lett.* 379, pp. 95–103. DOI: 10.1016/j.epsl.2013.08.011.

Čížková, H. and C. R. Bina (2019). "Linked influences on slab stagnation: Interplay between lower mantle viscosity structure, phase transitions, and plate coupling". *Earth and Planetary Science Letters* 509, pp. 88–99.

Čížková, H., J. van Hunen, and A. van den Berg (2007). "Stress distribution within subducting slabs and their deformation in the transition zone". *Physics of the Earth and Planetary Interiors* 161.3-4, pp. 202–214. DOI: 10.1016/j.pepi.2007.02.002.

Clennett, E. J., A. F. Holt, M. G. Tetley, T. W. Becker, and C. Faccenna (2023). "Assessing plate reconstruction models using plate driving force consistency tests". *Scientific reports* 13.1, p. 10191. DOI: 10.1038/s41598-023-37117-w.

Coltice, N., L. Husson, C. Faccenna, and M. Arnould (2019). "What drives tectonic plates?" *Science Advances* 5.10. DOI: 10.1126/sciadv.aax4295.

Coltice, N. and J Schmalzl (2006). "Mixing times in the mantle of the early Earth derived from 2-D and 3-D numerical simulations of convection". *Geophysical Research Letters* 33.23. DOI: 10.1029/2006GL027707.

Coltice, N., M. Seton, T. Rolf, R. Müller, and P. J. Tackley (2013). "Convergence of tectonic reconstructions and mantle convection models for significant fluctuations in seafloor spreading". *Earth and Planetary Science Letters* 383, pp. 92–100.

Coltice, N. and G. E. Shephard (2018). "Tectonic predictions with mantle convection models". *Geophysical Journal International* 213.1, pp. 16–29. DOI: 10.1093/gji/ggx531.

Condie, K. C. (2021). *Earth as an evolving planetary system*. Academic Press.

Conrad, C. P. and C. Lithgow-Bertelloni (2004). "The temporal evolution of plate driving forces: Importance of "slab suction" versus "slab pull" during the Cenozoic". *Journal of Geophysical Research: Solid Earth* 109.B10. DOI: 10.1029/2004JB002991.

Conrad, C. and C. Lithgow-Bertelloni (2006). "Influence of continental roots and asthenosphere on plate-mantle coupling". *Geophys. Res. Lett.* 33.L05312. DOI: https://doi.org/10.1029/2005GL025621.

Cordier, P., K. Gouriet, T. Weidner, J. van Orman, O. Castelnau, J. M. Jackson, and P. Carrez (2023). "Periclase deforms more slowly than bridgmanite under mantle conditions". *Nature* 613.7943, pp. 303–307. DOI: 10.1038/s41586-022-05410-9.

Dannberg, J. and R. Gassmöller (2018). "Chemical trends in ocean islands explained by plume-slab interaction". *PNAS* 115.17, pp. 4351–4356.

Dasgupta, R., N. Mandal, and C. Lee (2021). "Controls of subducting slab dip and age on the extensional versus compressional deformation in the overriding plate". *Tectonophysics* 801, p. 228716. DOI: 10.1016/j.tecto.2020.228716.

DeMets, C and S Merkouriev (2021). "Detailed reconstructions of India–Somalia Plate motion, 60 Ma to present: implications for Somalia Plate absolute motion and India–Eurasia Plate motion". *Geophysical Journal International* 227.3, pp. 1730–1767. DOI: 10.1093/gji/ggx531.

Deschamps, F., L. Cobden, and P. J. Tackley (2012). "The primitive nature of large low shear-wave velocity provinces". *Earth and Planetary Science Letters* 349, pp. 198–208.

Dobson, D. P. and J. P. Brodholt (2005). "Subducted banded iron formations as a source of ultralow-velocity zones at the core–mantle boundary". *Nature* 434.7031, pp. 371–374. DOI: 10.1038/nature03430.

Domeier, M., P. V. Doubrovine, T. H. Torsvik, W. Spakman, and A. L. Bull (2016). "Global correlation of lower mantle structure and past subduction". *Geophysical Research Letters* 43.10, pp. 4945–4953. DOI: 10.1002/2016GL068827.

Domeier, M., G. E. Shephard, J. Jakob, C. Gaina, P. V. Doubrovine, and T. H. Torsvik (2017). "Intraoceanic subduction spanned the Pacific in the Late Cretaceous–Paleocene". *Science Advances* 3.11, eaao2303. DOI: 10.1126/sciadv.aao2303.

Domeier, M. and T. H. Torsvik (2014). "Plate tectonics in the late Paleozoic". *Geoscience Frontiers* 5.3, pp. 303–350. DOI: 10.1016/j.gsf.2014.01.002.

Doubrovine, P. V., B. Steinberger, and T. H. Torsvik (2012). "Absolute plate motions in a reference frame defined by moving hot spots in the Pacific, Atlantic, and Indian oceans". *Journal of Geophysical Research: Solid Earth* 117.B9.

Doucet, L. S., Z.-X. Li, H. Gamal El Dien, A. Pourteau, J. B. Murphy, W. J. Collins, N. Mattielli, H. K. Olierook, C. J. Spencer, and R. N. Mitchell

(2020). "Distinct formation history for deep-mantle domains reflected in geochemical differences". *Nature Geoscience* 13.7, pp. 511–515. DOI: 10.1038/s41561-020-0599-9.

Dupré, B. and C. J. Allègre (1983). "Pb–Sr isotope variation in Indian Ocean basalts and mixing phenomena". *Nature* 303.5913, pp. 142–146. DOI: 10.1038/303142a0.

Eakins, B. W. and P. F. Lonsdale (2003). "Structural patterns and tectonic history of the Bauer microplate, Eastern Tropical Pacific". *Marine Geophysical Researches* 24, pp. 171–205. DOI: 10.1007/s11001-004-5882-4.

Engebretson, D. C., A. Cox, and R. G. Gordon (1985). "Relative motions between oceanic and continental plates in the Pacific basin". DOI: 10.1130/SPE206-p1.

Espinoza, V. and G. Iaffaldano (2023). "Rapid absolute plate motion changes inferred from high-resolution relative spreading reconstructions: A case study focusing on the South America plate and its Atlantic/Pacific neighbors". *Earth and Planetary Science Letters* 604, p. 118009. DOI: 10.1016/j.epsl.2023.118009.

Faccenna, C., T. W. Becker, C. P. Conrad, and L. Husson (2013). "Mountain building and mantle dynamics". *Tectonics* 32.1, pp. 80–93. DOI: 10.1029/2012TC003176.

Faccenna, C., T. W. Becker, A. F. Holt, and J. P. Brun (2021). "Mountain building, mantle convection, and supercontinents: Holmes (1931) revisited". *Earth and Planetary Science Letters* 564, p. 116905. DOI: 10.1016/j.epsl.2021.116905.

Faccenna, C., T. W. Becker, S. Lallemand, and B. Steinberger (2012). "On the role of slab pull in the Cenozoic motion of the Pacific plate". *Geophysical Research Letters* 39.3. DOI: 10.1029/2011GL050155.

Faccenna, C., L. Jolivet, C. Piromallo, and A. Morelli (2003). "Subduction and the depth of convection in the Mediterranean mantle". *Journal of Geophysical Research: Solid Earth* 108.B2. DOI: 10.1029/2001JB001690.

Faccenna, C., F. Rossetti, T. W. Becker, S. Danesi, and A. Morelli (2008). "Recent extension driven by mantle upwelling beneath the Admiralty Mountains (East Antarctica)". *Tectonics* 27.4. DOI: 10.1029/2007TC002197.

Flament, N., O. Bodur, S. Williams, and A. Merdith (2022). "Assembly of the basal mantle structure beneath Africa". *Nature* 603, pp. 846–851. DOI: 10.1038/s41586-022-04538-y.

Fleitout, L. and C. Froidevaux (1982). "Tectonics and topography for a lithosphere containing density heterogeneities". *Tectonics* 1.1, pp. 21–56. DOI: 10.1029/TC001i001p00021.

Forsyth, D. and S. Uyeda (1975). "On the relative importance of the driving forces of plate motion". *Geophysical Journal International* 43.1, pp. 163–200. DOI: 10.1111/j.1365-246X.1975.tb00631.x.

Fraters, M., C. Thieulot, A. van den Berg, and W. Spakman (2019). "The Geodynamic World Builder: a solution for complex initial conditions in numerical modelling". *Solid Earth* 10, pp. 1785–1807. DOI: 10.5194/se-10-1785-2019.

Fuston, S. and J. Wu (2021). "Raising the Resurrection plate from an unfolded-slab plate tectonic reconstruction of northwestern North America since early Cenozoic time". *GSA Bulletin* 133.5-6, pp. 1128–1140. DOI: 10.1130/B35677.1.

Gaina, C., T. H. Torsvik, D. J. van Hinsbergen, S. Medvedev, S. C. Werner, and C. Labails (2013). "The African Plate: A history of oceanic crust accretion and subduction since the Jurassic". *Tectonophysics* 604, pp. 4–25. DOI: 10.1016/j.tecto.2013.05.037.

Garel, F., S. Goes, D. Davies, J. Davies, S. Kramer, and C. Wilson (2014). "Interaction of subducted slabs with the mantle transition-zone: A regime diagram from 2-D thermo-mechanical models with a mobile trench and an overriding plate". *Geochem. Geophys. Geosyst.* 15.1739–1765. DOI: 10.1002/2014GC005257.

Garnero, E. J., A. K. McNamara, and S.-H. Shim (2016). "Continent-sized anomalous zones with low seismic velocity at the base of Earth's mantle". *Nature Geoscience* 9.7, pp. 481–489. DOI: 10.1038/NGEO2733.

Gassmöller, R., H. Lokavarapu, E. M. Heien, E. G. Puckett, and W. Bangerth (2018). "Flexible and scalable particle-in-cell methods with adaptive mesh refinement for geodynamic computations". *Geochem. Geophys. Geosyst.* 19.9, pp. 3596–3604. DOI: 10.1029/2018GC007508.

Gassmöller, R., J. Dannberg, W. Bangerth, T. Heister, and R. Myhill (2020). "On formulations of compressible mantle convection". *Geophysical Journal International* 221.2, pp. 1264–1280. DOI: 10.1093/gji/ggaa078.

Gazel, E., J. Trela, M. Bizimis, A. Sobolev, V. Batanova, C. Class, and B. Jicha (2018). "Long-lived source heterogeneities in the Galapagos mantle plume". *Geochemistry, Geophysics, Geosystems* 19.8, pp. 2764–2779. DOI: 10.1029/2017GC007338.

Gerya, T. (2014). "Precambrian geodynamics: concepts and models". *Gondwana Research* 25.2, pp. 442–463.

Girard, J., G. Amulele, R. Farla, A. Mohiuddin, and S.-i. Karato (2016). "Shear deformation of bridgmanite and magnesiowüstite aggregates at lower mantle conditions". *Science* 351.6269, pp. 144–147. DOI: 10.1126/science.aad3113.

Glerum, A., C. Thieulot, M. Fraters, C. Blom, and W. Spakman (2018). "Nonlinear viscoplasticity in ASPECT: benchmarking and applications to subduction". *Solid Earth* 9.2, pp. 267–294. DOI: 10.5194/se-9-267-2018.

Glerum, A., S. Brune, D. S. Stamps, and M. R. Strecker (2020). "Victoria continental microplate dynamics controlled by the lithospheric strength distribution of the East African Rift". *Nature Communications* 11.1, pp. 1–15. DOI: 10.1038/s41467-020-16176-x.

Goes, S., F. Cammarano, and U. Hansen (2004). "Synthetic seismic signature of thermal mantle plumes". *Earth and Planetary Science Letters* 218.3-4, pp. 403–419. DOI: 10.1016/S0012-821X(03)00680-0.

Goes, S., R. Agrusta, J. Van Hunen, and F. Garel (2017). "Subduction-transition zone interaction: A review". *Geosphere* 13.3, pp. 644–664. DOI: 10.1130/GES01476.1.

Goes, S., F. Capitanio, G. Morra, M Seton, and D Giardini (2011). "Signatures of downgoing plate-buoyancy driven subduction in Cenozoic plate motions". *Physics of the Earth and Planetary Interiors* 184.1-2, pp. 1–13. DOI: 10.1016/j.pepi.2010.10.007.

Goltz, G. and M. Böse (2002). "Configurational entropy of critical earthquake populations". *Geophys. Res. Lett.* 29.20. DOI: 10.1029/2002GL015540.

Guerrero, J. M., F. Deschamps, Y. Li, W.-P. Hsieh, and P. J. Tackley (2023). "Influence of heterogeneous thermal conductivity on the long-term evolution of the lower-mantle thermochemical structure: implications for primordial reservoirs". *Solid Earth* 14.2, pp. 119–135. DOI: 10.5194/se-14-119-2023.

Gülcher, A. J. P., M. D. Ballmer, and P. J. Tackley (2021). "Coupled dynamics and evolution of primordial and recycled heterogeneity in Earth's lower mantle". *Solid Earth* 12.9, pp. 2087–2107. DOI: 10.5194/se-12-2087-2021.

Gülcher, A. J., D. J. Gebhardt, M. D. Ballmer, and P. J. Tackley (2020). "Variable dynamic styles of primordial heterogeneity preservation in the Earth's lower mantle". *Earth and Planetary Science Letters* 536, p. 116160. DOI: 10.1016/j.epsl.2020.116160.

Gürer, D., R. Granot, and D. J. van Hinsbergen (2022). "Plate tectonic chain reaction revealed by noise in the Cretaceous quiet zone". *Nature Geoscience* 15.3, pp. 233–239. DOI: 10.1038/s41561-022-00893-7.

Hafkenscheid, E, M. Wortel, and W Spakman (2006). "Subduction history of the Tethyan region derived from seismic tomography and tectonic reconstructions". *Journal of Geophysical Research: Solid Earth* 111.B8. DOI: 10.1029/2005JB003791.

Hansen, L. N., D. Wallis, T. Breithaupt, C. A. Thom, and I. Kempton (2021). "Dislocation creep of olivine: Backstress evolution controls transient creep at high temperatures". *Journal of Geophysical Research: Solid Earth* 126.5, e2020JB021325. DOI: 10.1029/2020JB021325.

Hansen, U., D. A. Yuen, S. Kroening, and T. Larsen (1993). "Dynamical consequences of depth-dependent thermal expansivity and viscosity on mantle circulations and thermal structure". *Physics of the earth and planetary interiors* 77.3-4, pp. 205–223. DOI: 10.1016/0031-9201(93)90099-U.

Hart, S. R. (1984). "A large-scale isotope anomaly in the Southern Hemisphere mantle". *Nature* 309.5971, pp. 753–757. DOI: 10.1038/309753a0.

Hassan, R., R. D. Müller, M. Gurnis, S. E. Williams, and N. Flament (2016). "A rapid burst in hotspot motion through the interaction of tectonics and deep mantle flow". *Nature* 533.7602, pp. 239–242. DOI: 10.1038/nature17422.

Heister, T., J. Dannberg, R. Gassmöller, and W. Bangerth (2017). "High Accuracy Mantle Convection Simulation through Modern Numerical Methods. II: Realistic Models and Problems". *Geophy. J. Int.* 210.2, pp. 833–851. DOI: 10.1093/gji/ggx195.

Hirth, G. and D. L. Kohlstedt (1996). "Water in the oceanic upper mantle: Implications for rheology, melt extraction and the evolution of the lithosphere". *Earth Planet. Sci. Lett.* 144, pp. 93–108. DOI: 10.1016/0012-821X(96)00154-9.

Hirth, G. and D. Kohlstedt (2003). "Rheology of the upper mantle and the mantle wedge: A view from the experimentalists". *in Inside the Subduc-*

tion Factory, ed. J. Eiler, Geophysical Monograph American Geophysical Union, Washington, D.C. 138, pp. 83–105.

Hoernle, K., R. Werner, J. P. Morgan, D. Garbe-Schonberg, J. Bryce, and J. Mrazek (2000). "Existence of complex spatial zonation in the Galápagos plume". *Geology* 28.5, pp. 435–438. DOI: 10.1130/0091-7613(2000) 28<435:EOCSZI>2.0.CO;2.

Höink, T., A. M. Jellinek, and A. Lenardic (2011). "Viscous coupling at the lithosphere-asthenosphere boundary". *Geochemistry, Geophysics, Geosystems* 12.10. DOI: 10.1029/2011GC003698.

Holmes, A. (1928). "Radioactivity and continental drift".

Holt, A., T. Becker, and B. Buffett (2015). "Trench migration and overriding plate stress in dynamic subduction models". *Geophy. J. Int.* 201, pp. 172–192. DOI: 10.1093/gji/ggv011.

Homrighausen, S., K. Hoernle, F. Hauff, P. A. Hoyer, K. M. Haase, W. H. Geissler, and J. Geldmacher (2023). "Evidence for compositionally distinct upper mantle plumelets since the early history of the Tristan-Gough hotspot". *Nature Communications* 14.1, p. 3908.

Hu, J., M. Gurnis, J. Rudi, G. Stadler, and R. D. Müller (2022). "Dynamics of the abrupt change in Pacific Plate motion around 50 million years ago". *Nature Geoscience* 15.1, pp. 74–78. DOI: 10.1038/s41561-021-00862-6.

Isacks, B., J. Oliver, and L. R. Sykes (1968). "Seismology and the new global tectonics". *Journal of Geophysical Research* 73.18, pp. 5855–5899. DOI: 10.1029/JB073i018p05855.

Ishii, K. and S. R. Wallis (2022). "A possible mechanism for spontaneous cyclic back-arc spreading". *Progress in Earth and Planetary Science* 9.1, p. 27. DOI: 10.1186/s40645-022-00486-3.

Ita, J. and S. King (1994). "Sensitivity of convection with an endothermic phase change to the form of governing equations, initial conditions, boundary conditions, and equation of state". *J. Geophys. Res.* 99.B8, pp. 15,919–15,938. DOI: 10.1029/94JB00852.

Ito, G., Y. Shen, G. Hirth, and C. J. Wolfe (1999). "Mantle flow, melting, and dehydration of the Iceland mantle plume". *Earth and Planetary Science Letters* 165.1, pp. 81–96. DOI: 10.1016/S0012-821X(98)00216-7.

Jackson, M. G. and F. Macdonald (2022). "Hemispheric geochemical dichotomy of the mantle is a legacy of austral supercontinent assembly

and onset of deep continental crust subduction". *AGU Advances* 3.6, e2022AV000664. DOI: 10.1029/2022AV000664.

Jackson, M., T. Becker, and J. Konter (2018). "Evidence for a deep mantle source for EM and HIMU domains from integrated geochemical and geophysical constraints". *Earth and Planetary Science Letters* 484, pp. 154–167. DOI: 10.1016/j.epsl.2017.11.052.

Jackson, M., T. Becker, and B. Steinberger (2021). "Spatial characteristics of recycled and primordial reservoirs in the deep mantle". *Geochemistry, Geophysics, Geosystems* 22.3, e2020GC009525. DOI: 10.1029/2020GC009525.

Jackson, M., J. Konter, and T. Becker (2017). "Primordial helium entrained by the hottest mantle plumes". *Nature* 542.7641, pp. 340–343. DOI: 10.1038/nature21023.

Jones, T. D., N. Sime, and P. van Keken (2021). "Burying Earth's primitive mantle in the slab graveyard". *Geochemistry, Geophysics, Geosystems* 22.3, e2020GC009396. DOI: 10.1029/2020GC009396.

Karato, S.-I. and P. Wu (1993). "Rheology of the Upper Mantle: A synthesis". *Science* 260, pp. 771–778. DOI: 10.1126/science.260.5109.771.

Karato, S.-I. (2008). *Deformation of Earth Materials*. Cambridge University Press. ISBN: 978-0-521-84404-8.

Karato, S.-i., S. Zhang, and H.-R. Wenk (1995). "Superplasticity in Earth's lower mantle: evidence from seismic anisotropy and rock physics". *Science* 270.5235, pp. 458–461. DOI: 10.1126/science.270.5235.458.

Katsura, T., A. Shatskiy, M. G. M. Manthilake, S. Zhai, H. Fukui, D. Yamazaki, T. Matsuzaki, A. Yoneda, E. Ito, A. Kuwata, *et al.* (2009). "Thermal expansion of forsterite at high pressures determined by in situ X-ray diffraction: The adiabatic geotherm in the upper mantle". *Physics of the Earth and Planetary Interiors* 174.1-4, pp. 86–92. DOI: 10.1016/j.pepi.2008.08.002.

Katsura, T., H. Yamada, O. Nishikawa, M. Song, A. Kubo, T. Shinmei, S. Yokoshi, Y. Aizawa, T. Yoshino, M. J. Walter, *et al.* (2004). "Olivine-wadsleyite transition in the system (Mg, Fe) 2SiO4". *Journal of Geophysical Research: Solid Earth* 109.B2. DOI: 10.1029/2003JB002438.

Keken, P. van, E. Hauri, and C. Ballentine (2002). "Mantle mixing: the generation, preservation and destruction of chemical heterogeneity". *Annu. Rev. Earth Sci* 30, pp. 493–525. DOI: 10.1146/annurev.earth.30.091201.141236.

Kellogg, L. and D. Turcotte (1990). "Mixing and the distribution of heterogeneities in a chaotically convecting mantle". *Journal of Geophysical Research: Solid Earth* 95.B1, pp. 421–432. DOI: 10.1029/JB095iB01p00421.

King, S. D. (2016). "Reconciling laboratory and observational models of mantle rheology in geodynamic modelling". *Journal of Geodynamics* 100, pp. 33–50. DOI: 10.1016/j.jog.2016.03.005.

Knesel, K. M., B. E. Cohen, P. M. Vasconcelos, and D. S. Thiede (2008). "Rapid change in drift of the Australian plate records collision with Ontong Java plateau". *Nature* 454.7205, pp. 754–757. DOI: 10.1038/nature07138.

Koelemeijer, P., A. Deuss, and J. Ritsema (2017). "Density structure of Earth's lowermost mantle from Stoneley mode splitting observations". *Nature Communications* 8.1, p. 15241. DOI: 10.1038/ncomms15241.

Konstantinovskaya, E. (2002). "The mechanism of continental crust accretion: an example of Western Kamchatka". *Geotectonics* 36.5, pp. 393–411.

Kronbichler, M., T. Heister, and W. Bangerth (2012). "High accuracy mantle convection simulation through modern numerical methods". *Geophy. J. Int.* 191, pp. 12–29. DOI: 10.1111/j.1365-246X.2012.05609.x.

Kumar, P., X. Yuan, M. R. Kumar, R. Kind, X. Li, and R. Chadha (2007). "The rapid drift of the Indian tectonic plate". *Nature* 449.7164, pp. 894–897. DOI: 10.1038/nature06214.

Lamb, S., J. D. Moore, M. Perez-Gussinye, and T. Stern (2020). "Global whole lithosphere isostasy: implications for surface elevations, structure, strength, and densities of the continental lithosphere". *Geochemistry, Geophysics, Geosystems* 21.10, e2020GC009150. DOI: 10.1029/2020GC009150.

Lambart, S., J. M. Koornneef, M.-A. Millet, G. R. Davies, M. Cook, and C. J. Lissenberg (2019). "Highly heterogeneous depleted mantle recorded in the lower oceanic crust". *Nature Geoscience* 12.6, pp. 482–486. DOI: 10.1038/s41561-019-0368-9.

Le Pichon, X. (1968). "Sea-floor spreading and continental drift". *Journal of geophysical research* 73.12, pp. 3661–3697. DOI: 10.1029/JB073i012p03661.

Lee, C. and S. D. King (2011). "Dynamic buckling of subducting slabs reconciles geological and geophysical observations". *Earth and Planetary Science Letters* 312.3-4, pp. 360–370. DOI: 10.1016/j.epsl.2011.10.033.

Li, S., D. J. van Hinsbergen, Y. Najman, J. Liu-Zeng, C. Deng, and R. Zhu (2020a). "Does pulsed Tibetan deformation correlate with Indian plate motion changes?" *Earth and Planetary Science Letters* 536, p. 116144. DOI: 10.1016/j.epsl.2020.116144.

Li, S., D. J. van Hinsbergen, Z. Shen, Y. Najman, C. Deng, and R. Zhu (2020b). "Anisotropy of magnetic susceptibility (AMS) analysis of the Gonjo Basin as an independent constraint to date Tibetan shortening pulses". *Geophysical Research Letters* 47.8, e2020GL087531. DOI: 10.1029/2020GL087531.

Li, Y., L. Liu, D. Peng, H. Dong, and S. Li (2023). "Evaluating tomotectonic plate reconstructions using geodynamic models with data assimilation, the case for North America". *Earth-Science Reviews*, p. 104518. DOI: 10.1016/j.earscirev.2023.104518.

Lin, Y.-A., L. Colli, and J. Wu (2022). "NW Pacific-Panthalassa intra-oceanic subduction during Mesozoic times from mantle convection and geoid models". *Geochem. Geophys. Geosyst.* 23, e2022GC010514. DOI: 10.1029/2022GC010514.

Lithgow-Bertelloni, C. and M. A. Richards (1998). "The dynamics of Cenozoic and Mesozoic plate motions". *Reviews of Geophysics* 36.1, pp. 27–78. DOI: 10.1029/97RG02282.

Manga, M. (1996). "Mixing of heterogeneities in the mantle: Effect of viscosity differences". *Geophys. Res. Lett.* 23.4, pp. 403–406. DOI: 10.1029/96GL00242.

Matthews, K. J., M. Seton, and R. D. Müller (2012). "A global-scale plate reorganization event at 105- 100 Ma". *Earth and Planetary Science Letters* 355, pp. 283–298. DOI: 10.1016/j.epsl.2012.08.023.

McKenzie, D. P. and R. L. Parker (1967). "The North Pacific: an example of tectonics on a sphere". *Nature* 216.5122, pp. 1276–1280. DOI: 10.1038/2161276a0.

McNamara, A. K. (2019). "A review of large low shear velocity provinces and ultra low velocity zones". *Tectonophysics* 760, pp. 199–220. DOI: 10.1016/j.tecto.2018.04.015.

Merdith, A. S., S. E. Williams, A. S. Collins, M. G. Tetley, J. A. Mulder, M. L. Blades, A. Young, S. E. Armistead, J. Cannon, S. Zahirovic, *et al.* (2021). "Extending full-plate tectonic models into deep time: Linking the Neoproterozoic and the Phanerozoic". *Earth-Science Reviews* 214, p. 103477. DOI: 10.1016/j.earscirev.2020.103477.

Mitrovica, J. and A. Forte (2004). "A new inference of mantle viscosity based upon joint inversion of convection and glacial isostatic adjustment data". *Earth and Planetary Science Letters* 225.1-2, pp. 177–189. DOI: 10.1016/j.epsl.2004.06.005.

Morgan, W. J. (1968). "Rises, trenches, great faults, and crustal blocks". *Journal of Geophysical Research* 73.6, pp. 1959–1982. DOI: 10.1029/JB073i006p01959.

Morishima, H, T Kato, M Suto, E Ohtani, S. Urakawa, W Utsumi, O Shimomura, and T Kikegawa (1994). "The phase boundary between α-and β-Mg2SiO4 determined by in situ X-ray observation". *Science* 265.5176, pp. 1202–1203. DOI: 10.1126/science.265.5176.1202.

Müller, R. D., N. Flament, J. Cannon, M. G. Tetley, S. E. Williams, X. Cao, Ö. F. Bodur, S. Zahirovic, and A. Merdith (2022). "A tectonic-rules-based mantle reference frame since 1 billion years ago–implications for supercontinent cycles and plate–mantle system evolution". *Solid Earth* 13.7, pp. 1127–1159. DOI: 10.5194/se-13-1127-2022.

Müller, R. D., S. Zahirovic, S. E. Williams, J. Cannon, M. Seton, D. J. Bower, M. G. Tetley, C. Heine, E. Le Breton, S. Liu, *et al.* (2019). "A global plate model including lithospheric deformation along major rifts and orogens since the Triassic". *Tectonics* 38.6, pp. 1884–1907. DOI: 10.1029/2018TC005462.

Mulyukova, E., B. Steinberger, M. Dabrowski, and S. Sobolev (2015). "Survival of LLSVPs for billions of years in a vigorously convecting mantle: Replenishment and destruction of chemical anomaly". *J. Geophys. Res.* 120, pp. 3824–3847. DOI: 10.1002/2014JB011688.

Naar, D. F. and R. Hey (1989). "Speed limit for oceanic transform faults". *Geology* 17.5, pp. 420–422. DOI: 10.1130/0091-7613(1989)017<0420:SLFOTF>2.3.CO;2.

Naliboff, J. B. and L. H. Kellogg (2007). "Can large increases in viscosity and thermal conductivity preserve large-scale heterogeneity in the mantle?" *Physics of the Earth and Planetary Interiors* 161.1-2, pp. 86–102. DOI: 10.1016/j.pepi.2007.01.009.

Neves, M., R. Searle, and M. Bott (2003). "Easter microplate dynamics". *Journal of Geophysical Research: Solid Earth* 108.B4. DOI: 10.1029/2001JB000908.

Parsons, A. J., K. Sigloch, and K. Hosseini (2021). "Australian Plate Subduction is Responsible for Northward Motion of the India-Asia Collision

Zone and 1,000 km Lateral Migration of the Indian Slab". *Geophysical Research Letters* 48.18, e2021GL094904. DOI: 10.1029/2021GL094904.

Patriat, P. and J. Achache (1984). "India–Eurasia collision chronology has implications for crustal shortening and driving mechanism of plates". *Nature* 311.5987, pp. 615–621. DOI: 10.1038/311615a0.

Peng, D. and L. Liu (2022). "Quantifying slab sinking rates using global geodynamic models with data-assimilation". *Earth-Science Reviews* 230, p. 104039. DOI: 10.1016/j.earscirev.2022.104039.

Perugini, D., C. De Campos, M. Petrelli, D. Morgavi, F. P. Vetere, and D. Dingwell (2015). "Quantifying magma mixing with the Shannon entropy: Application to simulations and experiments". *Lithos* 236, pp. 299–310. DOI: 10.1016/j.lithos.2015.09.008.

Pokornỳ, J., H. Čížková, and A. van den Berg (2021). "Feedbacks between subduction dynamics and slab deformation: Combined effects of nonlinear rheology of a weak decoupling layer and phase transitions". *Physics of the Earth and Planetary Interiors* 313, p. 106679. DOI: 10.1016/j.pepi.2021.106679.

Pons, M., S. V. Sobolev, S. Liu, and D. Neuharth (2022). "Hindered trench migration due to slab steepening controls the formation of the Central Andes". *Journal of Geophysical Research: Solid Earth* 127.12, e2022JB025229. DOI: 10.1029/2022JB025229.

Qayyum, A., N. Lom, E. L. Advokaat, W. Spakman, D. G. van Der Meer, and D. J. van Hinsbergen (2022). "Subduction and Slab Detachment Under Moving Trenches During Ongoing India-Asia Convergence". *Geochemistry, Geophysics, Geosystems* 23.11, e2022GC010336. DOI: 10.1029/2022GC010336.

Ranalli, G. (1995). *Rheology of the Earth*. Springer Science & Business Media.

Replumaz, A., H. Kárason, R. D. van der Hilst, J. Besse, and P. Tapponnier (2004). "4-D evolution of SE Asia's mantle from geological reconstructions and seismic tomography". *Earth and Planetary Science Letters* 221.1-4, pp. 103–115. DOI: 10.1016/S0012-821X(04)00070-6.

Ribe, N., E. Stutzmann, Y. Ren, and R. van der Hilst (2007). "Buckling instabilities of subducted lithosphere beneath the transition zone". *Earth Planet. Sci. Lett.* 254, pp. 173–179.

Ritsema, J., A. Deuss, H. van Heijst, and J. Woodhouse (2011). "S40rts: a degree-40 shear- velocity model for the mantle from new rayleigh wave

dispersion, teleseismic traveltime and normal-mode splitting function measurements". *Geophy. J. Int.* 184, pp. 1223–1236.

Ritsema, J. and V. Lekić (2020). "Heterogeneity of seismic wave velocity in Earth's mantle". *Annual Review of Earth and Planetary Sciences* 48, pp. 377–401. DOI: 10.1146/annurev-earth-082119-065909.

Rolf, T., F. A. Capitanio, and P. J. Tackley (2018). "Constraints on mantle viscosity structure from continental drift histories in spherical mantle convection models". *Tectonophysics* 746, pp. 339–351. DOI: 10.1016/j.tecto.2017.04.031.

Rona, P. A. and E. S. Richardson (1978). "Early Cenozoic global plate reorganization". *Earth and Planetary Science Letters* 40.1, pp. 1–11. DOI: 10.1016/0012-821X(78)90069-9.

Royden, L. H. and L. Husson (2006). "Trench motion, slab geometry and viscous stresses in subduction systems". *Geophysical Journal International* 167.2, pp. 881–905. DOI: 10.1111/j.1365-246X.2006.03079.x.

Saxena, A., J. Dannberg, R. Gassmöller, M. Fraters, T. Heister, and R. Styron (2023). "High-Resolution Mantle Flow Models Reveal Importance of Plate Boundary Geometry and Slab Pull Forces on Generating Tectonic Plate Motions". *Journal of Geophysical Research: Solid Earth* 128.8, e2022JB025877. DOI: 10.1029/2022JB025877.

Schellart, W. P. (2010). "Andean mountain building and magmatic arc migration driven by subduction-induced whole mantle flow". *Nature Communications* 8.

Schellart, W. (2005). "Influence of the subducting plate velocity on the geometry of the slab and migration of the subduction hinge". *Earth Planet. Sci. Lett.* 231, pp. 197–219. DOI: 10.1016/j.epsl.2004.12.019.

Schubert, G., D. Turcotte, and P. Olson (2001). *Mantle Convection in the Earth and Planets.* Cambridge University Press. ISBN: 0-521-70000-0. DOI: 10.1017/CBO9780511612879.

Sdrolias, M. and R. D. Müller (2006). "Controls on back-arc basin formation". *Geochemistry, Geophysics, Geosystems* 7.4. DOI: 10.1029/2005GC001090.

Searle, R., R. Bird, R. Rusby, and D. Naar (1993). "The development of two oceanic microplates: Easter and Juan Fernandez microplates, East Pacific Rise". *Journal of the Geological Society* 150.5, pp. 965–976. DOI: 10.1144/gsjgs.150.5.0965.

Segal, A. and N. Praagman (2005). *The Sepran FEM package*. Tech. rep. Technical Report, Ingenieursbureau Sepra, The Netherlands.

Şengör, A. C., D. Altıner, C. Zabcı, G. Sunal, N. Lom, E. Aylan, and T. Öner (2023). "On the nature of the Cimmerian Continent". *Earth-Science Reviews*, p. 104520. DOI: 10.1016/j.earscirev.2023.104520.

Seton, M., N. Flament, J. Whittaker, R. D. Müller, M. Gurnis, and D. J. Bower (2015). "Ridge subduction sparked reorganization of the Pacific plate-mantle system 60–50 million years ago". *Geophysical Research Letters* 42.6, pp. 1732–1740. DOI: 10.1002/2015GL063057.

Shannon, C. E. (1948). "A mathematical theory of communication". *The Bell system technical journal* 27.3, pp. 379–423. DOI: 10.1002/j.1538-7305.1948.tb01338.x.

Shapiro, M. and A. Solov'ev (2009). "Formation of the Olyutorsky–Kamchatka foldbelt: A kinematic model". *Russian Geology and Geophysics* 50.8, pp. 668–681. DOI: 10.1016/j.rgg.2008.10.006.

Sigloch, K. and M. G. Mihalynuk (2013). "Intra-oceanic subduction shaped the assembly of Cordilleran North America". *Nature* 496.7443, p. 50.

Sim, S. J., M. Spiegelman, D. R. Stegman, and C. Wilson (2020). "The influence of spreading rate and permeability on melt focusing beneath mid-ocean ridges". *Physics of the Earth and Planetary Interiors* 304, p. 106486. DOI: 10.1016/j.pepi.2020.106486.

Spakman, W., M. Chertova, A. van den Berg, and D. van Hinsbergen (2018). "Puzzling features of western Mediterranean tectonics explained by slab dragging". *Nature Geoscience* 11, pp. 211–216. DOI: 10.1038/s41561-018-0066-z.

Stegman, D., R. Farrington, F. Capitanio, and W. Schellart (2010). "A regime diagram for subduction styles from 3-D numerical models of free subduction". *Tectonophysics* 483, pp. 29–45.

Steinbach, V. and D. A. Yuen (1995). "The non-adiabatic nature of mantle convection as revealed by passive tracers". *Earth and Planetary Science Letters* 136.3-4, pp. 241–250. DOI: 10.1016/0012-821X(95)00166-A.

Steinberger, B. and A. Calderwood (2006). "Models of large-scale viscous flow in the Earth's mantle with constraints from mineral physics and surface observations". *Geophy. J. Int.* 167, pp. 1461–1481. DOI: 10.1111/j.1365-246X.2006.03131.x.

Stern, R. J. and T. Gerya (2018). "Subduction initiation in nature and models: A review". *Tectonophysics* 746, pp. 173–198. DOI: 10.1016/j.tecto.2017.10.014.

Stracke, A., F. Genske, J. Berndt, and J. M. Koornneef (2019). "Ubiquitous ultra-depleted domains in Earth's mantle". *Nature Geoscience* 12.10, pp. 851–855. DOI: 10.1038/s41561-019-0446-z.

Su, C., Y. Liu, D. Fan, W. Song, J. Jiang, Z. Sun, and G. Yang (2022). "Thermodynamic Properties of Fe-Bearing Wadsleyite and Determination of the Olivine-Wadsleyite Phase Transition Boundary in (Mg, Fe) 2SiO4 System". *Frontiers in Earth Science* 10, p. 879678. DOI: 10.3389/feart.2022.879678.

Tackley, P. (2000). "Self-consistent generation of tectonic plates in time-dependent, three-dimensional mantle convection simulations 1. Pseudo-plastic yielding". *Geochem. Geophys. Geosyst.* 1.1.

ter Heege, J., J. De Bresser, and C. Spiers (2004). "Composite flow laws for crystalline materials with log-normally distributed grain size: theory and application to olivine". *Journal of structural Geology* 26.9, pp. 1693–1705. DOI: 10.1016/j.jsg.2004.01.008.

Thieulot, C. (2018). "GHOST: Geoscientific Hollow Sphere Tesselation". *Solid Earth* 9.1–9. DOI: 10.5194/se-9-1169-2018.

Thom, C. A. and J. D. Kirkpatrick (2023). "A mechanism for transient creep in crustal shear zones". *Geology* 51.7, pp. 642–646. DOI: 10.1130/g50867.1.

Torsvik, T. H., K. Burke, B. Steinberger, S. J. Webb, and L. D. Ashwal (2010). "Diamonds sampled by plumes from the core–mantle boundary". *Nature* 466.7304, pp. 352–355. DOI: 10.1038/nature09216.

Torsvik, T. H., P. V. Doubrovine, B. Steinberger, C. Gaina, W. Spakman, and M. Domeier (2017). "Pacific plate motion change caused the Hawaiian-Emperor Bend". *Nature Communications* 8.1, p. 15660. DOI: 10.1038/ncomms15660.

Torsvik, T. H., R. D. Müller, R. van der Voo, B. Steinberger, and C. Gaina (2008). "Global plate motion frames: toward a unified model". *Reviews of geophysics* 46.3. DOI: 10.1029/2007RG000227.

Torsvik, T. H., B. Steinberger, G. E. Shephard, P. V. Doubrovine, C. Gaina, M. Domeier, C. P. Conrad, and W. W. Sager (2019). "Pacific-Panthalassic reconstructions: Overview, errata and the way forward".

Geochemistry, Geophysics, Geosystems 20.7, pp. 3659–3689. DOI: 10. 1029/2019GC008402.

Torsvik, T. H., R. van der Voo, P. V. Doubrovine, K. Burke, B. Steinberger, L. D. Ashwal, R. G. Trønnes, S. J. Webb, and A. L. Bull (2014). "Deep mantle structure as a reference frame for movements in and on the Earth". *Proceedings of the National Academy of Sciences* 111.24, pp. 8735–8740.

Tosi, N., D. A. Yuen, N. de Koker, and R. M. Wentzcovitch (2013). "Mantle dynamics with pressure-and temperature-dependent thermal expansivity and conductivity". *Physics of the Earth and Planetary Interiors* 217, pp. 48–58. DOI: 10.1016/j.pepi.2013.02.004.

Trampert, J., P. Vacher, and N. Vlaar (2001). "Sensitivities of seismic velocities to temperature, pressure and composition in the lower mantle". *Physics of the Earth and Planetary Interiors* 124.3-4, pp. 255–267. DOI: 10.1016/S0031-9201(01)00201-1.

Turner, A. J., R. F. Katz, M. D. Behn, and T. Keller (2017). "Magmatic focusing to mid-ocean ridges: The role of grain-size variability and non-Newtonian viscosity". *Geochemistry, Geophysics, Geosystems* 18.12, pp. 4342–4355. DOI: 10.1002/2017GC007048.

Ulvrova, M. M., N. Coltice, S. Williams, and P. J. Tackley (2019). "Where does subduction initiate and cease? A global scale perspective". *Earth and Planetary Science Letters* 528, p. 115836. DOI: 10.1016/j.epsl.2019. 115836.

Vaes, B., D. J. van Hinsbergen, and L. M. Boschman (2019). "Reconstruction of subduction and back-arc spreading in the NW Pacific and Aleutian Basin: Clues to causes of Cretaceous and Eocene plate reorganizations". *Tectonics* 38.4, pp. 1367–1413. DOI: 10.1029/2018TC005164.

van de Lagemaat, S. H. and D. J. van Hinsbergen (2023). "Plate tectonic cross-roads: Reconstructing the Panthalassa-Neotethys Junction Region from Philippine Sea Plate and Australasian oceans and orogens". *Gondwana Research*. DOI: 10.1016/j.gr.2023.09.013.

van de Lagemaat, S. H., D. J. van Hinsbergen, L. M. Boschman, P. J. Kamp, and W. Spakman (2018). "Southwest Pacific absolute plate kinematic reconstruction reveals major Cenozoic Tonga-Kermadec slab dragging". *Tectonics* 37.8, pp. 2647–2674. DOI: 10.1029/2017TC004901.

van de Lagemaat, S. H., P. J. Kamp, L. M. Boschman, and D. J. van Hinsbergen (2023). "Reconciling the Cretaceous breakup and demise

of the Phoenix Plate with East Gondwana orogenesis in New Zealand". *Earth-Science Reviews* 236, p. 104276. DOI: 10.1016/j.earscirev.2022. 104276.

van den Berg, A., G. Segal, and D. Yuen (2015). "SEPRAN: A Versatile Finite-Element Package for a Wide Variety of Problems in Geosciences". *Journal of Earth Science* 26.1, pp. 089–095. DOI: 10.1007/s12583-015-0508-0.

van den Berg, A., D. Yuen, K. Umemoto, M. Jacobs, and R. Wentzcovitch (2019). "Mass-dependent dynamics of terrestrial exoplanets using ab initio mineral properties". *Icarus* 317, pp. 412–426. DOI: 10.1016/j. icarus.2018.08.016.

van den Berg, A. P., P. E. van Keken, and D. A. Yuen (1993). "The effects of a composite non-Newtonian and Newtonian rheology on mantle convection". *Geophysical Journal International* 115.1, pp. 62–78. DOI: 10.1111/j.1365-246X.1993.tb05588.x.

van der Meer, D., T. Torsvik, W Spakman, D. van Hinsbergen, and M. Amaru (2012). "Intra-Panthalassa Ocean subduction zones revealed by fossil arcs and mantle structure". *Nature Geoscience* 5.3, pp. 215–219. DOI: 10.1038/ngeo708.

van der Meer, D. G., D. J. van Hinsbergen, and W. Spakman (2018). "Atlas of the underworld: Slab remnants in the mantle, their sinking history, and a new outlook on lower mantle viscosity". *Tectonophysics* 723, pp. 309–448. DOI: 10.1016/j.tecto.2017.10.004.

van der Meer, D. G., W. Spakman, D. J. van Hinsbergen, M. L. Amaru, and T. H. Torsvik (2010). "Towards absolute plate motions constrained by lower-mantle slab remnants". *Nature Geoscience* 3.1, pp. 36–40. DOI: 10.1038/ngeo708.

van der Meer, D. G., R. E. Zeebe, D. J. van Hinsbergen, A. Sluijs, W. Spakman, and T. H. Torsvik (2014). "Plate tectonic controls on atmospheric CO2 levels since the Triassic". *Proceedings of the National Academy of Sciences* 111.12, pp. 4380–4385. DOI: 10.1073/pnas.1315657111.

van der Voo, R., W. Spakman, and H. Bijwaard (1999). "Tethyan subducted slabs under India". *Earth and Planetary Science Letters* 171.1, pp. 7–20.

van Hinsbergen, D. J. J., B. Steinberger, P. V. Doubrovine, and R. Gassmöller (2011). "Acceleration and deceleration of India-Asia convergence since the Cretaceous: Roles of mantle plumes and continen-

tal collision". *Journal of Geophysical Research* 116.B6. DOI: 10.1029/2010JB008051.

van Hinsbergen, D., P. Lippert, G. Dupont-Nivet, N. McQuarrie, P. Doubrovine, W. Spakman, and T. Torsvik (2012). "Greater India Basin hypothesis and a two-stage Cenozoic collision between India and Asia". *Proceedings of the National Academy of Sciences of the United States of America* 109.20, pp. 7659–7664. DOI: 10.1073/pnas.1117262109.

van Hinsbergen, D. J. J., E Hafkenscheid, W. Spakman, J. Meulenkamp, and R. Wortel (2005). "Nappe stacking resulting from subduction of oceanic and continental lithosphere below Greece". *Geology* 33.4, pp. 325–328. DOI: 10.1130/G20878.1.

van Hinsbergen, D. J., P. C. Lippert, S. Li, W. Huang, E. L. Advokaat, and W. Spakman (2019). "Reconstructing Greater India: Paleogeographic, kinematic, and geodynamic perspectives". *Tectonophysics* 760, pp. 69–94. DOI: 10.1016/j.tecto.2018.04.006.

van Hinsbergen, D. J. and T. L. Schouten (2021). "Deciphering paleogeography from orogenic architecture: constructing orogens in a future supercontinent as thought experiment". *American journal of science* 321.6, pp. 955–1031. DOI: 10.2475/06.2021.09.

van Hinsbergen, D. J., B. Steinberger, C. Guilmette, M. Maffione, D. Gürer, K. Peters, A. Plunder, P. McPhee, C. Gaina, E. L. Advokaat, *et al.* (2021). "A record of plume-induced plate rotation triggering seafloor spreading and subduction initiation". DOI: 10.1038/s41561-021-00780-7.

Vilella, K., T. Bodin, C.-E. Boukaré, F. Deschamps, J. Badro, M. D. Ballmer, and Y. Li (2021). "Constraints on the composition and temperature of LLSVPs from seismic properties of lower mantle minerals". *Earth and Planetary Science Letters* 554, p. 116685. DOI: 10.1016/j.epsl.2020.116685.

Wallis, D., L. N. Hansen, K. M. Kumamoto, C. A. Thom, O. Plümper, M. Ohl, W. B. Durham, D. L. Goldsby, D. E. Armstrong, C. D. Meyers, *et al.* (2020). "Dislocation interactions during low-temperature plasticity of olivine and their impact on the evolution of lithospheric strength". *Earth and Planetary Science Letters* 543, p. 116349. DOI: 10.1016/j.epsl.2020.116349.

Wallis, D., L. N. Hansen, A. J. Wilkinson, and R. A. Lebensohn (2021). "Dislocation interactions in olivine control postseismic creep of the upper mantle". *Nature Communications* 12.1, p. 3496. DOI: 10.1038/s41467-021-23633-8.

Wallis, D., M. Sep, and L. N. Hansen (2022). "Transient Creep in Subduction Zones by Long-Range Dislocation Interactions in Olivine". *Journal of Geophysical Research: Solid Earth* 127.1, e2021JB022618. DOI: 10.1029/2021JB022618.

Warners-Ruckstuhl, K. N., R. Govers, and R. Wortel (2012). "Lithosphere–mantle coupling and the dynamics of the Eurasian Plate". *Geophysical Journal International* 189.3, pp. 1253–1276.

Warren, J. M. and G. Hirth (2006). "Grain size sensitive deformation mechanisms in naturally deformed peridotites". *Earth and Planetary Science Letters* 248.1-2, pp. 438–450. DOI: 10.1016/j.epsl.2006.06.006.

Waszek, L., B. Tauzin, N. C. Schmerr, M. D. Ballmer, and J. C. Afonso (2021). "A poorly mixed mantle transition zone and its thermal state inferred from seismic waves". *Nature geoscience* 14.12, pp. 949–955. DOI: 10.1038/s41561-021-00850-w.

Wegener, A. (1912). "Die entstehung der kontinente". *Geologische Rundschau* 3.4, pp. 276–292. DOI: 10.1007/BF02202896.

Weis, D., M. O. Garcia, J. M. Rhodes, M. Jellinek, and J. S. Scoates (2011). "Role of the deep mantle in generating the compositional asymmetry of the Hawaiian mantle plume". *Nature Geoscience* 4.12, pp. 831–838. DOI: 10.1038/ngeo1328.

Wellmann, J. F. and K. Regenauer-Lieb (2012). "Uncertainties have a meaning: Information entropy as a quality measure for 3-D geological models". *Tectonophysics* 526, pp. 207–216. DOI: 10.1016/j.tecto.2011.05.001.

White, L. T. and G. S. Lister (2012). "The collision of India with Asia". *Journal of Geodynamics* 56, pp. 7–17. DOI: h10.1016/j.jog.2011.06.006.

Wichmann, D., P. Delandmeter, H. A. Dijkstra, and E. van Sebille (2019). "Mixing of passive tracers at the ocean surface and its implications for plastic transport modelling". *Environmental Research Communications* 1.11, p. 115001. DOI: 10.1088/2515-7620/ab4e77.

Wilson, C. J., D. H. Moore, S. A. Vollgger, and H. E. Madeley (2020). "Structural evolution of the orogenic gold deposits in central Victoria, Australia: The role of regional stress change and the tectonic regime". *Ore Geology Reviews* 120, p. 103390. DOI: 10.1016/j.oregeorev.2020.103390.

Wortel, R. and S. Cloetingh (1981). "On the origin of the Cocos-Nazca spreading center". *Geology* 9.9, pp. 425–430. DOI: 0.1130/0091-7613(1981)9<425:OTOOTC>2.0.CO;2.

Wouters, M. C., L. Pérez-Díaz, A. Tuck-Martin, G. Eagles, J. Adam, and R. Govers (2021). "Dynamics of the African Plate 75 Ma: From Plate Kinematic Reconstructions to Intraplate Paleo-Stresses". *Tectonics* 40.7, e2020TC006355. DOI: 10.1029/2020TC006355.

Wright, N. M., M. Seton, S. E. Williams, and R. D. Mueller (2016). "The Late Cretaceous to recent tectonic history of the Pacific Ocean basin". *Earth-Science Reviews* 154, pp. 138–173. DOI: 10.1016/j.earscirev.2015.11.015.

Wu, J. T.-J. and J. Wu (2019). "Izanagi-Pacific ridge subduction revealed by a 56 to 46 Ma magmatic gap along the northeast Asian margin". *Geology* 47.10, pp. 953–957. DOI: 10.1130/G46778.1.

Wu, J., Y.-A. Lin, N. Flament, J. T.-J. Wu, and Y. Liu (2022). "Northwest Pacific-Izanagi plate tectonics since Cretaceous times from western Pacific mantle structure". *Earth and Planetary Science Letters* 583, p. 117445. DOI: 10.1016/j.epsl.2022.117445.

Wu, J., J. Suppe, R. Lu, and R. Kanda (2016). "Philippine Sea and East Asian plate tectonics since 52 Ma constrained by new subducted slab reconstruction methods". *Journal of Geophysical Research: Solid Earth* 121.6, pp. 4670–4741. DOI: 10.1002/2016JB012923.

Xue, K., W. P. Schellart, and V. Strak (2022). "Overriding plate deformation and topography during slab rollback and slab rollover: insights from subduction experiments". *Tectonics* 41.2, e2021TC007089. DOI: 10.1029/2021TC007089.

Yamazaki, D. and S.-I. Karato (2001). "Some mineral physics constraints on the rheology and geothermal structure of Earth's lower mantle". *American Mineralogist* 86.4, pp. 385–391. DOI: 10.2138/am-2001-0401.

Yan, J., M. D. Ballmer, and P. J. Tackley (2020). "The evolution and distribution of recycled oceanic crust in the Earth's mantle: Insight from geodynamic models". *Earth and Planetary Science Letters* 537, p. 116171. DOI: 10.1016/j.epsl.2020.116171.

Zahirovic, S., R. D. Müller, M. Seton, and N. Flament (2015). "Tectonic speed limits from plate kinematic reconstructions". *Earth and Planetary Science Letters* 418, pp. 40–52. DOI: 10.1016/j.epsl.2015.02.037.

Zelst, I. van, F. Crameri, A. E. Pusok, A. Glerum, J. Dannberg, and C. Thieulot (2022). "101 Geodynamic modelling: How to design, interpret, and communicate numerical studies of the solid Earth". 13, pp. 583–637. DOI: 10.5194/se-13-583-2022.

Samenvatting

Deformatie in de aardkorst en de daarbij voorkomende aardbevingen, vulkanisme en ertsen worden veroorzaakt door processen die plaatsvinden in het binnenste van de aarde. Geodynamische modellen zijn de enige manier om de wisselwerking tussen het (diepe) binnenste van de aarde en het oppervlak te bestuderen. Dit komt doordat deze processen plaatsvinden op tijdschalen van miljoenen tot miljarden jaren maar ook omdat directe observaties alleen kunnen worden gedaan op het oppervlak, waar het geologische archief het een venster terug in de tijd biedt. De modellen maken vaak gebruik van invoer uit één vakgebied en proberen de structuur en evolutie van de vaste aarde te voorspellen en de vormende processen te verklaren. De daaruit komende hypothesen kunnen dan weer worden getest door observaties vanuit een ander vakgebied. Nieuwe geologische of geofysische observaties zijn een manier om deze modellen te verbeteren en daarmee ons begrip van de dynamische vaste aarde. Dit proefschrift richt zich op de interactie tussen de mantel en de beweging van de tektonische platen erboven door gebruik te maken van nieuwe kinematische observaties die zijn verkregen vanuit tektonische reconstructies op basis van geologische gegevens.

Een van de observaties is de gemiddelde snelheid van plaatzinken, die is verkregen door het geologische archief met tomografisch afgebeelde platen in de mantel te correleren. Deze observatie illustreert de vertraging van platen van enkele centimeters per jaar in de bovenste mantel tot een gemiddelde zinksnelheid in de onderste mantel van een tiental millimeters per jaar. We onderzoeken het effect van variërende zinksnelheden op mantelstroming en -menging. Modellen met zinksnelheden van 10-15 mm/jaar vertonen een zeer beperkte beweging van de mantel. Deze modellen behouden grote ongemengde zones in de midden-mantel, zelfs na 1 miljard jaar van gesimuleerde subductie en mantelconvectie. Het vergelijken van zulke modellen met de daadwerkelijke mantel is moeilijk omdat observaties uit de mantel afkomstig zijn van de interpretatie van seismische tomografie of de chemische signatuur van vulkanisch gesteente uit pluimen. We gebruiken configurationele entropie om de menging van verschillende composities in onze modellen in kaart te brengen en te kwantificeren. Deze entropie kan worden gebruikt om, met een globaal getal, de gemengde toestand van de mantel te analyseren en verschillende geodynamische modellen met elkaar te vergelijken. Bovendien kan de lokale entropie nuttig zijn om geodynamische modellen te valideren tegen anomalieën in de mantel uit seismologische of geochemische observaties.

De vertraging van platen van subducerende platen naar de gemiddelde zinksnelheden van platen in de onderste mantel vindt plaats door verdikking of buiging in de bovenste mantel en de mantelovergangszone. Recente kinematische reconstructies van de Indische plaat hebben snelle oscillaties in plaatbeweging, ter grootte van 50% in 2 tot 3 miljoen jaar. Onze regionale geodynamische modellen tonen aan dat het buigen van platen de oscillaties in plaatbewegingssnelheid kan veroorzaken, voordat de platen de onderste mantel in zinken. We laten zien dat amplitude en periode van de oscillaties afhangen van de gemiddelde subductiesnelheid, aangezien deze onderhevig is aan de tijd waarin een plaat door de bovenste mantel beweegt. We bespreken hoe episodische deformatie in de bovenliggende plaat kan worden veroorzaakt door het buigen van subducerende platen en hoe tektonische reconstructies zulke snelle oscillaties in plaatbeweging zouden kunnen missen.

Dit laat zien dat tektonische platen worden aangedreven door subductie, met een 'slab pull'-kracht, in de bovenste paar honderd kilometer van de mantel. Platen die niet subduceren, en dus niet zo'n kracht hebben, zijn echter niet mantel-stationair. Voor continentale platen kan dit worden verklaard door mantelsleur op hun kiel, veroorzaakt door mantelstroming of pluimpulsen. Daarentegen is de Pacifische plaat een voorbeeld van een oceanische plaat die in het Laat-Krijt tot 9 cm/jaar bewoog, zonder actieve subductie en volledig omringd door mid-oceanische ruggen en transformbreuken. We gebruiken 3D-geodynamische modellen van een oceanische plaat, omgeven door mid-oceanische ruggen, die wordt beïnvloed door de plaatbeweging van de platen aan weerszijden van de ruggen. Deze modellen tonen aan dat de oceanische plaat in het midden langzaam achter de snelst bewegende buurplaat aan beweegt en dat die beweging kan worden verhoogd door viskeuze koppeling onder de mid-oceanische ruggen. We bespreken welke mechanismen verantwoordelijk kunnen zijn voor deze koppeling en hoe dit een rol kan spelen bij de overdracht van veranderingen in plaatbeweging, bijvoorbeeld tijdens wereldwijde plaat reorganisaties.

Dit proefschrift toont aan dat geodynamische modellen, als ze afgestemd zijn op specifieke kinematische observaties van plaatbeweging, nuttig zijn om processen te bestuderen die tektonische platen en beweging in de aardmantel aandrijven. Dit soort modellen bieden een krachtig middel om inzicht te krijgen in individuele processen maar ook in de dynamische evolutie die de aarde heeft gevormd, waarbij gebruik wordt gemaakt van inzichten uit de verschillende disciplines die de vaste aarde bestuderen.

Acknowledgements

This dissertation represents the end of an era for me as it is the culmination of a 13-year long journey of studying, teaching, and doing research at Utrecht University. In this period, I have met an enormous amount of people that impressed, supported, and guided me, for which I am very grateful. I would like to take this opportunity to express my gratitude to all of you for your part in this journey and eventually the completion of my PhD.

First and foremost, I would like to thank my promotor **Douwe**, I thoroughly enjoyed working together on my projects and the fieldwork-teaching campaigns we did. Thank you for supervising me during my BSc thesis, MSc thesis and taking me along as 'baby'-staff to Aliaga, where I learned that doing a PhD was the right path for me to take. Your guidance over these past years was invaluable as was your patience when we needed to talk about model problems. Thank you for always having time for a talk, whether about academia, cycling, other 'geosports' or just to rant about life, your guidance-style really suited me and helped me get to the end. That made these past years, besides a great learning experience, also a fun endeavor.

I also want to express my gratitude to my other two promoters, **Cedric** and **Wim**, for helping me with the technical and mathematical aspect of my work. For finding better ways to illustrate and present my results, for solving problems with the models itself, but also for the regular lunch alarm at 12 o'clock. Thank you for teaching me to be a geophysicist.

My peers, fellow PhD students, office mates, paranymphs and friends: **Suzanna** and **Bram** have been of great support during my PhD, I couldn't have done it without you. You both have been part of my journey since my first year in Utrecht and I couldn't have wished for better partners in crime. Sharing achievements as well as disappointments, having fun on fieldwork, gossiping about our boss, it all was needed to lessen the burden.

There are more colleagues from the TRIGGER team I would like to thank. **Abdul**, **Goran**, **Nalan**, **Thomas** thanks for the fun and experiences we could share. **Lydian**, thanks for all the small talk and especially for taking me to Costa Rica, which might be the sole initiator of me doing this PhD. **Eldert**, thanks for all we have done together, from sharing our year as junior teacher to teaching in the field. **Kalijn**, thanks for our talks on teaching

and for your widespread enthusiasm and optimism. A special thanks to **Jakub**, with whom I set-up, worked out and wrote the third chapter of this dissertation, I think we can be proud of the product.

Thank you to all other colleagues that made the coffee-breaks, fieldwork supervision and the PhD journey more enjoyable: **Annemijn, Rûna, Hen, Janneke, Romy, Liz, Frenk, Rosa, Martha, Marjolein, Renato, Carl, Jorien, Joris, Bas, Wout, Mariette, Leo, Emilia, Alissa**. Thanks to **Lukas**, **Menno** and **Arie** for helping with very specific coding questions, and to **Inge Loes** for helping me obtaining my teachers degree. I would also like to thank **Dennis, Maurits, Erwin** and **Rob** for my time with them as first occupants of the VMA, which led to starting this PhD. Thanks to **Lennart, Barbara, Boy, Hester, Sanne, Iris** and all other PhD-participants of the Hoe?Zo!-show for those amazing two years of theatrical adventure.

Outside of the work-environment I want to thank all my friends that helped me stay sane these last years. First of all, to all my friends from the '**HK 11**', and its entire agglomeration: your presence through my studies and the subsequent years has been priceless. Thanks for distracting me with staycations, holidays, and all the vrijmibo's, and for showing interest in my work. **Heren 2, Heren 3**, thanks for the joy during and after volleyball, it provided a much needed relaxation to split the week. Thanks to the **four musketeers**, I know contact has been limited but our friendship means a lot to me.

I am very grateful for my family and want to acknowledge everything you have done for me. **Pap, Map**, thank you for creating a stimulating environment for me to grow up in, in which I always was able to do whatever I wanted and thank you for all the support throughout the years. To my two sisters, **Karin** and **Marleen**, thank you for being excellent role models and for always raising the bar ever so slightly.

And finally, most importantly, my dear **Mayke**, you have been part of my life through this entire journey and I want to thank you from the deepest of my heart. I am grateful to have met you and to share my life with you. Thank you for giving all the emotional, mental, and culinary support through all the ups and all the downs I had on this venture. I count myself lucky that we share so many interests and have a similar approach in life. As I am now, quite literally, closing this chapter, I am very much looking forward to start the next with you, you are amazing!

Curriculum Vitae

7 January 1993   **Born in Dordrecht, the Netherlands**

2005 - 2011   **Secondary School**
Stedelijk Dalton Lyceum, Dordrecht

2011 - 2014   **BSc Earth Sciences**
Utrecht University

2015 - 2018   **MSc Earth Structure and Dynamics**
Utrecht University

2018 - 2019   **Junior teacher, Department of Earth Sciences**
Utrecht University

2019 - 2024   **PhD Candidate, Mantle Dynamics group**
Utrecht University

2024   **Lecturer, Department of Earth Sciences**
Utrecht University

Bibliography

Included in this thesis (Chapters 1-3):

1. **van der Wiel, E.**, van Hinsbergen, D.J.J., Thieulot, C. & Spakman, W., 2024. Linking rates of slab sinking to long-term lower mantle flow and mixing. *Earth and Planetary Science Letters*, 625, p.118471.

2. **van der Wiel, E.**, Thieulot, C., & van Hinsbergen, D.J.J (in review). Quantifying mantle mixing through configurational entropy, *Solid Earth*.

3. **van der Wiel, E.**, Pokorný, J., Čížková, H., Spakman, W., van den Berg, A.P. & van Hinsbergen, D.J.J., 2023. Slab buckling as a driver for rapid oscillations in plate motion and subduction rate. (in review). *Communications Earth and Environment*.

Not included in this thesis:

4. Boschman, L.M., **van der Wiel, E.**, Flores, K.E., Langereis, C.G., & van Hinsbergen, D.J.J. (2019). The Caribbean and Farallon plates connected: Constraints from stratigraphy and paleomagnetism of the Nicoya Peninsula, Costa Rica. *Journal of Geophysical Research: Solid Earth*, 124(7), 6243-6266.

5. Boschman, L.M., Van Hinsbergen, D.J.J., Langereis, C.G., Flores, K.E., Kamp, P.J., Kimbrough, D.L., Hayato, U., van de Lagemaat, S.H.A., **van der Wiel, E.** & Spakman, W. (2021). Reconstructing lost plates of the Panthalassa Ocean through paleomagnetic data from circum-Pacific accretionary orogens. *American Journal of Science*, 321(6), 907-954.

6. Vaes, B., van Hinsbergen, D.J.J., van de Lagemaat, S.H.A., **van der Wiel, E.**, Lom, N., Advokaat, E.L., Boschman, L.M., Gallo, L.C., Greve, A., Guilmette, C. and Li, S., 2023. A global apparent polar wander path for the last 320 Ma calculated from site-level paleomagnetic data. *Earth-Science Reviews*, p.104547.